LIFETIME MEASUREMENTS OF MAGNESIUM-32 IN THE $N = 20$ ISLAND OF INVERSION

By

Robert Martin Elder

A DISSERTATION

Submitted to
Michigan State University
in partial fulfillment of the requirements
for the degree of

Physics - Doctor of Philosophy

2020

ABSTRACT

LIFETIME MEASUREMENTS OF MAGNESIUM-32 IN THE $N = 20$ ISLAND OF INVERSION

By

Robert Martin Elder

Understanding how nuclear shell structure and magic numbers emerge near stability but change as nuclides move away from stability is one of the main goals of modern nuclear structure studies. The $N = 20$ island of inversion is one of the oldest and best-studied examples of a magic number disappearing in exotic isotopes, but new observations are still emerging. Nuclides in this region exhibit collective behavior driven by the neutron particle-hole intruder configurations across the reduced gap between the sd and pf shells. The assignment of the ^{32}Mg nuclide to the $N = 20$ island of inversion is supported from studies of the mass, excited states, and transition rate to the 2^+_1 state of ^{32}Mg. However, a complete understanding of this classic island of inversion nuclide is still a challenge. The 0^+_2 state of ^{32}Mg was observed at a lower energy than many models predicted, leading to a reinterpretation of the collectivity in ^{32}Mg. Reduced transition rates are valuable observables to characterize collectivity However, precise measurements of the reduced $E2$ transition rates in ^{32}Mg are still needed to test the validity of recent theoretical calculations.

This dissertation reports the results from an experimental study of the collectivity in ^{32}Mg. The present work includes lifetime measurements for the lowest 0^+, 2^+, and 4^+ excited states in ^{32}Mg which are used to determine the reduced $E2$ transition rates. Lifetime measurements were performed using two different and complementary experimental approaches. First, the TRIPLEX device was used along with the Recoil-distance Method and Doppler-shift Attenuation Method to measure the lifetimes of the short-lived 2^+_1 and

4_1^+ states in ^{32}Mg. The results reinforce the evidence from the energy systematics and earlier $B(E2)$ measurements which suggest that the ground-state band in ^{32}Mg is collective. Second, a novel in-flight technique referred to here as the Cascade Doppler-shift Method was used to observe decays from the 0_2^+ isomer in ^{32}Mg. The 0_2^+ state was confirmed and the measured lifetime suggests a large collectivity in this state as well. The small partial cross section populating the 0_2^+ state in the ^{9}Be(^{34}Si,^{32}Mg)X reaction provides experimental evidence for the dominance of intruder configurations in the 0_2^+ state.

In summary, the lifetime measurements presented in this thesis indicate the collectivity in ^{32}Mg driven by intruder configurations that dominate the ground state as well as low-lying excited states. Experimental methods based on in-flight Doppler-shift techniques are demonstrated in this work and highlight how a broad range of lifetimes from 1 ps to tens of ns can be measured in rare-isotope beam experiments.

ACKNOWLEDGMENTS

There are many people whom I must thank for their support during my thesis research. Foremost, I am thankful for the guidance of my research advisor Dr. Hironori Iwasaki. His advice has consistently encouraged me to reach greater rigor in my research and writing. I have learned a great deal about physics and about how to succeed as a scientist from Dr. Iwasaki. I am also deeply grateful for his sincere support when I would occasionally struggle with my work.

I also wish to thank the members of my guidance committee, Dr. Alexandra Gade, Dr. Heiko Hergert, Dr. Sean Liddick, and Dr. Stuart Tessmer for their encouragement and advice. They have challenged me to produce better work and also ensured that I had all that I needed throughout my research.

The experiment described in this work would not have been possible without the expertise of a great many people. The past and present members of the lifetime group have always provided me with valuable feedback. I am thankful for their hard work. I would also like to thank the gamma group for their expertise and skill. I am grateful to the entire experimental collaboration and the support staff at the National Superconducting Cyclotron Laboratory who made the experiment a success with their professionalism and attention.

My family and friends have been a constant source of affirmation and love for a long time before this research began. I could not have reached where I am now without my parents Joan and Andy. Thank you both for everything. Before I could take my first steps, you were there to raise and guide me. I also thank my friends from Michigan State University, from Ohio Wesleyan University, and from everywhere else who have kept me in good cheer even when I was faced with self-doubt. Finally, I am thankful for my son Kolten who has been

incredibly patient as I write this dissertation. The joy and pride he gives me has made me a better person.

TABLE OF CONTENTS

LIST OF TABLES

LIST OF FIGURES

Chapter 1

Introduction

1.1 The Atomic Nucleus

A nucleus sits at the core of every atom. The atom has a radius of 10^{-10} m, while the nucleus is merely 10^{-14} to 10^{-15} m in radius. However, the atomic nucleus is very dense and contains 99% of the atom's mass. The atomic nucleus is composed of protons and neutrons, together called *nucleons*, which are bound together by the strong nuclear force. The number of nucleons in a nucleus can vary from zero to a couple of hundred, although not all combinations of proton and neutron number will form a bound system. The number of protons Z determines the element of the nucleus and different isotopes of a given element are determined by the number of neutrons N. The total number of nucleons, also known as the mass number, is $A = Z + N$. Commonly, a particular nuclide, the nuclear species determined by a specific proton and neutron number, is designated with the notation $^A Z$ where Z is written as the elemental abbreviation. For example, the nuclide with six protons $Z = 6$ and seven neutrons $N = 7$ is the element carbon and would be written as ^{13}C.

Thousands of different nuclides are known to exist and can be depicted in a Segré chart such as the chart shown in Fig. 1.1 [1]. Each nuclide is represented by a square and arranged with increasing N along the x-axis and increasing Z along the y-axis. Figure 1.1 labels the isotopes by their mode of radioactive decay. The variety of radioactive decay modes is but
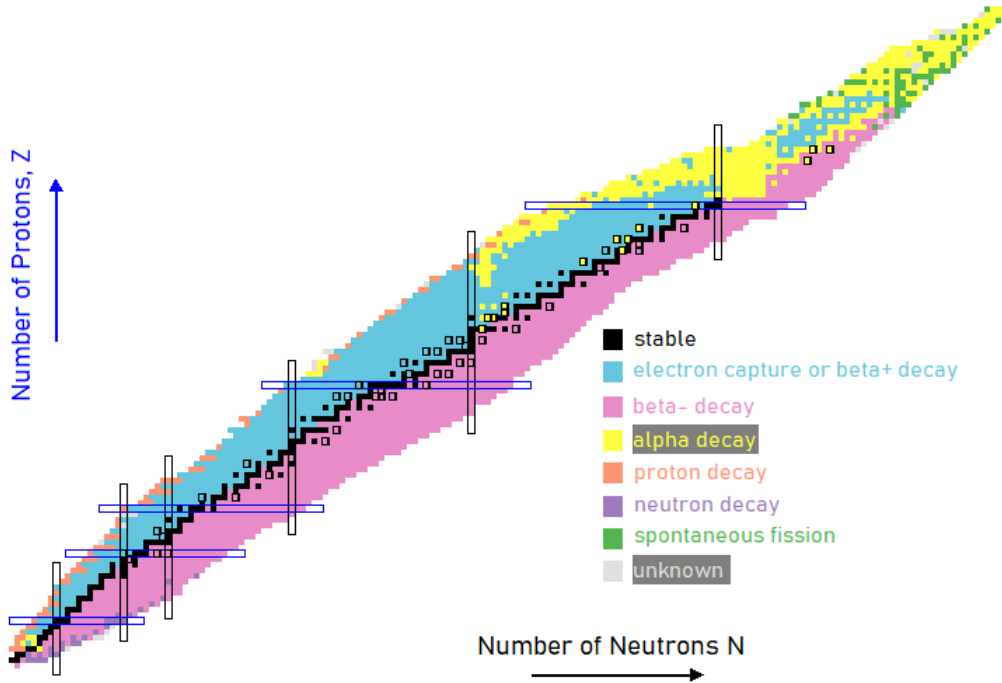
Figure 1.1: A Segré chart depicting the known nuclides. The nuclides are arranged by increasing N along the x-axis and increasing Z along the y-axis. The decay mode of each nuclide is represented by the color. The blue and black narrow rectangles represent the proton and neutron magic numbers. Magic number 2 is not labeled in this figure. The figure is adapted from Ref. [1]

one example of the breadth of phenomena that exists in nuclear structure.

Nucleons are not point particles, but have internal structure made up of quarks. The proton is composed of two up quarks and one down quark while the neutron has one up quark and two down quarks. The sum of the charges of these quarks, $+2/3e$ for each up quark and $-1/3e$ for each down quark, results in the net charges of the nucleons: $+e$ for protons, 0 for neutrons. The strong interaction confines the quarks together within the nucleon while the weak interaction is responsible for the beta decay process which is the most common decay mode for unstable nuclides. At the scale of the nucleus the details of the strong and weak interactions are contained in an effective interaction called the nuclear force.

The exact form of the nuclear force is not known. At very short distances, less than the

radius of a nucleon which is roughly $r = 10^{-15}$ m, the nuclear force is repulsive. The nuclear force between nucleons is strongly attractive for distances between about $r = 10^{-15}$ m and $r = 2 \times 10^{-15}$ m. At large distances the strength of the attractive nuclear force dies rapidly away and approaches zero.

Due to the positive charge of the protons, the Coulomb interaction plays an important role in the nuclear system. The Coulomb repulsion felt by protons in a typical nucleus is smaller than the net nuclear attraction, so the protons remain bound. Figure 1.1 shows that the smallest stable nuclides have roughly equal numbers of protons and neutrons. However for larger stable nuclides, the nucleus contains more neutrons than protons. This is a result of the Coulomb interaction causing the protons to be relatively less bound than the neutrons.

Each nucleon is a spin-1/2 particle and has orbital angular momentum l. The intrinsic spin and orbital angular momentum of a nucleon couple to the total angular momentum j. The momenta of all nucleons add vectorially to the total angular momentum of the nucleus, J or I, often called the spin of the nucleus. The total energy of the nucleus is also the sum of the energy contributions of the nucleons. Many states of a given nucleus are possible, corresponding to different combinations of the nucleons' single-particle states. The lowest-energy state of a nucleus is referred to as the ground state. The higher-energy states are usually referred to by their excitation energy E_x relative to the ground state. The spins and excitation energies of nuclear states are crucial observables that can assist our understanding of nuclear phenomena and the underlying nuclear interaction.

1.2 The Shell Model

Abundant experimental evidence suggests that at particular numbers of protons or neutrons certain properties emerge. Figure 1.2 shows the excitation energy of the the first excited states in even-even nuclides [2]. The figure shows that at particular numbers of protons or
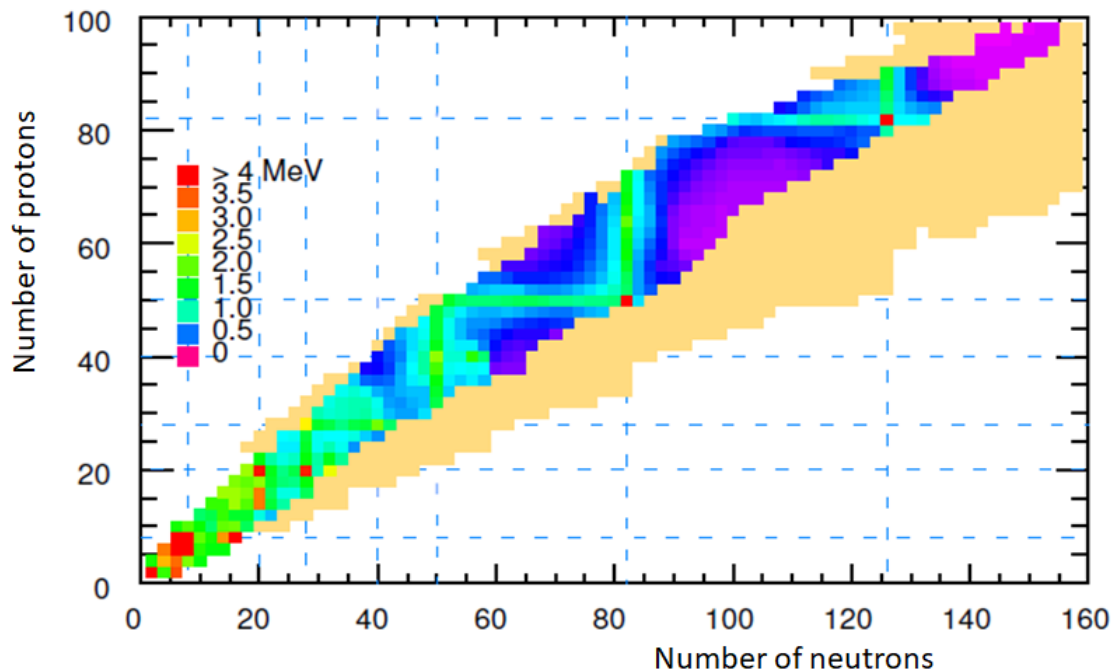
Figure 1.2: The energy of the first excited states in even-even nuclides. The large excitation energies at proton or neutron number of 8, 20, 28, 40, 50, 82, and 126 are evidence for closed shells at these magic numbers. The figure is adapted from Ref. [2].

neutrons the energy of the first excited state is dramatically larger than for surrounding nuclides. These numbers are called magic numbers and they are 2, 8, 20, 28, 50, 82, and 126 (2 is less evident from Fig. 1.2 but other evidence supports its magicity). This property is exactly what would be expected in the presence of a large shell gap between one set of single-particle states and another. What is fascinating is the regularity with which the shell gaps emerge for many nuclides with a magic number of protons or neutrons.

The phenomenon of magic numbers can be explained with the nuclear shell model. The

nuclear shell model is similar to the atomic shell model which describes the behavior of atomic electrons surrounding a nucleus. These shell models assume independent particle motion for the particles involved, and they assume that each particle is affected by a central potential, $V(r)$. Nucleons are densely bound together so it is not obvious that they could be independent of one another. However, nucleons obey the Pauli exclusion rule, meaning that no two nucleons can share the same quantum numbers. This implies that very little space in the nucleus is shared by the nucleons so they do not often collide [3]. Each nucleon is affected by the strong force caused by each other nucleon. While each strong force interaction between two nucleons is not necessarily central, the net force felt by a nucleon is sufficiently centralized. Protons and neutrons are distinguishable particles so they do not Pauli-block each other from filling single-particle levels. Thus, there will be separate shells for both protons and neutrons. The nuclear force is nearly the same for both protons and neutrons [2] and one result of this is that protons and neutrons have the same set of magic numbers.

The three-dimensional harmonic oscillator potential is a good starting point for the central potential of the nuclear shell model. The harmonic oscillator potential has the form

$$V_{HO}(r) = \frac{1}{2}m\omega^2 r^2 \tag{1.1}$$

and the nucleons occupy single-particle levels with energy

$$\epsilon = (N + 3/2)\hbar\omega \tag{1.2}$$

where the N is the harmonic oscillator quantum number and $N \geq 0$. Each energy level has

an occupancy of

$$D_N = (N+1)(N+2). \tag{1.3}$$

The levels of the harmonic oscillator potential are shown in the left column of Fig. 1.3. When the number of nucleons in a level meets the occupancy, that level is filled and the next nucleon must occupy a level that is higher in energy by $\hbar\omega$. This causes a natural gap between the energies of a closed-shell system and the system with one more nucleon. However, for the harmonic oscillator these gaps are at nucleon numbers 2, 8, 20, 40, 70, 112, and 168 as shown in the left column of Fig. 1.3. The harmonic oscillator alone is not sufficient to reproduce all the magic numbers greater than 20.

A more appropriate central potential choice is the Woods-Saxon potential [4] depicted in Fig. 1.4. The Woods-Saxon central potential has the form

$$V_{WS}(r) = \frac{V_0}{1 + e^{(r-R_0)/a_0}} \tag{1.4}$$

where V_0 is the depth of the central potential, R_0 is the radius, and a_0 is the diffuseness which controls how suddenly the potential well returns to zero [2]. One advantage of the Woods-Saxon potential is that the center of the potential is flatter than the harmonic oscillator. This properly accounts for the saturation of the nuclear density [3]. The Woods-Saxon potential also goes to zero at large r, while the harmonic oscillator increases to infinity. The trend toward zero more accurately reflects the fact that the nuclear force is a short range effect which dies out at large distances. The shape of the Woods-Saxon potential causes a splitting of the energy levels compared to the harmonic oscillator. The nucleons with larger orbital angular momentum l are lower in energy than states with lower l in the same harmonic oscillator N shell. In Fig. 1.3, the orbital angular momentum of a state is labeled according
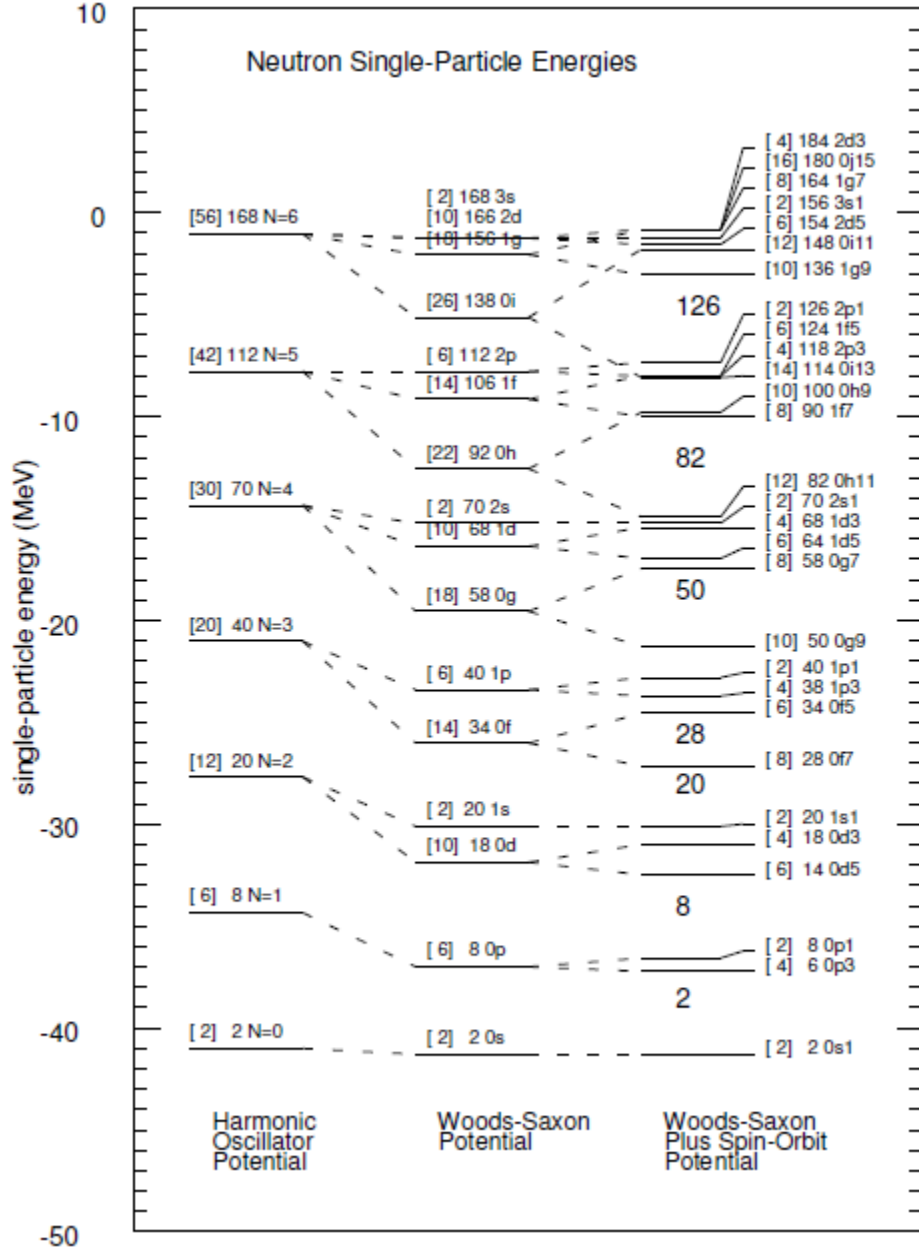
Figure 1.3: The single-particle orbits for neutrons in the ^{208}Pb nucleus, calculated for the harmonic oscillator potential, Woods-Saxon potential, and Woods-Saxon potential with spin-orbit term. The figure is adapted from Ref. [2]. The number in brackets is the occupancy of that orbit and is followed by the cumulative occupancy in that orbit and all lower-energy orbits. The orbits are labeled by the harmonic oscillator quantum number N, the orbital angular momentum quantum number $l = s, p, d, f, g, h, i$ meaning $l = 0, 1, 2, 3, 4, 5, 6$, and twice the total angular momentum quantum number $2j$.
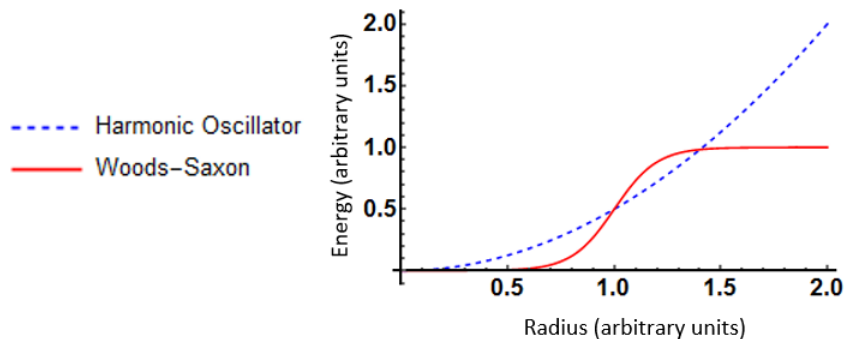
Figure 1.4: The forms of the central potentials discussed in the text. The harmonic oscillator potential is shown as a blue dashed line and the Woods-Saxon potential is shown as a solid red line. The Woods-Saxon potential is shifted vertically by one unit to align with the minimum of the harmonic oscillator potential.

to the convention used in spectroscopic notation, $s = 0$, $p = 1$, $d = 2$, $f = 3$, $g = 4$, $h = 5$, $i = 6$, etc.

The final adjustment to the central potential that results in the proper magic numbers is the inclusion of a spin-orbit term [5, 6]. This term depends on the coupling of intrinsic spin s and orbital angular momentum l and causes the state with s oriented parallel to l to be more bound than the antiparallel arrangement. For example, in Fig. 1.3 the $0p_{3/2}$ orbit is lower than the $0p_{1/2}$. This effect is large enough that an orbital from the next higher harmonic oscillator quantum number $N + 1$ can be lowered to intrude on a lower harmonic oscillator level N. This results in the negative-parity states seen in many medium and heavy nuclei. With the spin-orbit term, the observed magic numbers are now reproduced.

The shell model is a valuable theoretical tool that can explain many properties of nuclides at and near closed shells. As already discussed, the shell model explains the large excitation energy of the first excited state for magic nuclides. For a nucleus with one more or one fewer nucleon than than a doubly closed-shell nucleus, the shell model can suggest a straightforward interpretation. For example, ^{49}Sc has $Z = 21$ and $N = 28$, one more proton than ^{48}Ca.

The ^{49}Sc ground state can be imagined as an inert ^{48}Ca core with a single valence proton in the next available proton orbital, which is $0f_{7/2}$. This model predicts that the ground-state spin and parity is $7/2^-$ ($-$ parity corresponding to the odd value for $l = f = 3$), which turns out to reproduce observations. For full calculations, the shell model must account for the energies of the inert core, the valence nucleons, and the interactions between each of the nucleons and the core. This is no small task, but leads to accurate results and is computationally much simpler compared to treating the interactions among all A nucleons in a nucleus.

1.3 Nuclear Collectivity

Far from closed shells the number of nucleons outside of a closed shell becomes large. In these regions it becomes impractical to describe the behavior of a nucleus with one or a few nucleons outside of an inert core which causes shell model approaches to struggle. Instead, there are collective models that describe the nucleons with the collective motion of many nucleons.

One collective mode in nuclear systems is vibrational motion, in which the nucleons vibrate relative to a spherical shape. The vibrational modes are phonons which each has the same energy and spin 2. A standard vibrational band of states is built on the 0^+ ground state. The first vibrational state has one phonon, so by coupling to the ground state it can produce only a 2^+ state. The two-phonon vibrational mode couples a second phonon to the first and the possible states from the angular momentum coupling are 0^+, 2^+, and 4^+. The three-phonon mode again couples the angular momentum of the third phonon to any of the two-phonon states which results in states 0^+, 2^+, 3^+, 4^+, and 6^+. Since each additional

phonon adds the same energy, the two-phonon states are at about twice the excitation energy of the one-phonon state, and the three-phonon states have about thrice the excitation energy of the one-phonon state. This pattern continues, with the n-phonon states at an excitation energy of about

$$E_n = nE(2_1^+). \tag{1.5}$$

The regular spacing of these excited state energies is a clear signature of vibrational behavior.

A rigidly deformed nucleus will rotate about an axis perpendicular to the axis of symmetry. This rotational behavior is another collective phenomenon that exists in many nuclides. The energy of a rotational band built on a 0^+ ground state increases with spin,

$$E_{rot}(J) = J(J+1)\frac{\hbar^2}{2I} \tag{1.6}$$

where I is the moment of inertia of the nucleus and the spin J is even. The states of a typical rotational band are spaced with increasing energy separation at increasing spin. The shape of a nucleus can be characterized by the quadrupole deformation β and the asymmetry of the deformation γ. β is positive and represents the size of the deformation along the axis of symmetry, with $\beta = 0$ representing a spherical nucleus. For $\beta > 0$ and $\gamma = 0°$, the nucleus has a prolate shape, that is, the nucleus is deformed but maintains an axis of symmetry and it is longer along the axis of symmetry than it is for a perpendicular axis (for instance, like an American football). For $\beta > 0$ and $\gamma = 60°$, the shape is oblate, where the nucleus is shorter along the symmetry axis than a perpendicular axis (similar to the shape of a curling stone). For values of γ between $0°$ and $60°$, the nucleus has no axis of symmetry and is therefore triaxially deformed.

The simple pictures of vibrational and rotational nuclei are often insufficient to describe

the more complicated cases that arise in real nuclei. The collective modes can be coupled to an excited single-particle state, for instance. The vibrational and rotational modes can be coupled together as well, and the deformation of a rotating nucleus may not be rigid, but changing throughout the rotational band. Nevertheless, the systematic changes in energy of vibrational and rotational states provide a paradigm to which we can compare observed states. The ratio of the excited energies of the 4^+ and the 2^+ state $E(4^+)/E(2^+)$ is often used. This ratio is $E(4^+)/E(2^+) = 2.0$ for vibrational bands from Eq. 1.5. For rotational bands, the ratio is $E(4^+)/E(2^+) = 3.33$ from Eq. 1.6.

1.4 Electromagnetic Transitions

Not only are the states of a nucleus interesting, but the transitions between two nuclear states hold enlightening physical information as well. The atomic nucleus can undergo spontaneous radioactive decay from one state to another. The random decay of a nuclear state can be characterized by its lifetime. The lifetime τ of a state is proportional to the state's half-life,

$$\tau = \frac{t_{1/2}}{Ln(2)} \tag{1.7}$$

where the half-life $t_{1/2}$ is the time for half of a sample of N nuclei in the state of interest to decay. Radioactive decay reduces the energy of the nucleus while emitting radiation. The inverse process causes the nucleus to transition from a lower-energy state to a higher-energy state in the presence of either real or virtual radiation. An example of this is a Coulomb-excitation reaction where the nucleus is excited to a higher-energy state due to the electric field of another nucleus.

Most of the transitions between states of the same nucleus are electromagnetic transitions mediated by the exchange of a photon called a gamma ray [2]. Gamma rays are spin-1 bosons that carry energy E_γ proportional to their frequency ν. A nucleus in initial state i which decays to a final state f will emit a gamma ray with angular momentum λ such that the angular momentum of the system is conserved. This requires

$$|J_f - J_i| \leq \lambda \leq J_f + J_i \tag{1.8}$$

where J_i and J_f are the spins of the nuclear states i and f. Since gamma rays are spin-1, they cannot have the value $\lambda = 0$. Therefore, transitions between two nuclear states of spin $J_i = J_f = 0$ cannot occur via gamma-ray decay. Instead the transition experiences a different decay process such as electron capture or pair production.

The strong interaction conserves parity so most nuclear states have a well-defined parity $\pi = \pm 1$ [2]. For gamma-ray decay between states with good parity, the gamma ray also has a well-defined character which is either electric (E) when $\pi_f \pi_i (-1)^l = 1$ or magnetic (M) when $\pi_f \pi_i (-1)^l = -1$. Transitions between states are often referred to by their electromagnetic multipolarity $\pi\lambda$, for instance $E0$, $E1$, $M1$, $E2$, etc.

When more than one multipolarity is allowed to take place between two states, the multipolarity with the lower λ usually dominates. Formally, the decay rate between an initial state $|\psi_i >$ and a final state $|\psi_f >$ is

$$W = \sum_{\pi,\lambda} \left(\frac{8\pi(\lambda + 1)}{\lambda[(2\lambda + 1)!!]^2} \right) \left(\frac{k^{2\lambda+1}}{\hbar} \right) \frac{| < \psi_f ||\hat{O}(\pi\lambda)|| \psi_i > |^2}{(2J_i + 1)} \tag{1.9}$$

where $| < \psi_f ||\hat{O}(\pi\lambda)|| \psi_i > |$ is a reduced matrix element of the one-body operator $\hat{O}$, π is

E or M, and λ is the angular momentum of the transition [2]. The quantity k is the wave number of the gamma ray, $k = E_\gamma/\hbar c$. From Eq. 1.9 the reduced transition rate is defined as

$$B(\pi\lambda) = \frac{|<\psi_f||O(\pi\lambda)||\psi_i>|^2}{(2J_i + 1)}.$$ (1.10)

The reduced transition rate contains interesting physical properties of the nuclear system: the wavefunctions $|\psi_i>$ and $|\psi_f>$, and the transition operator $O(\pi\lambda)$. Reduced transition rates are often used to compare the observed properties of a nuclear transition with either theoretical calculations or with other nuclides. Since the reduced transition rate depends on J_i, the reduced transition rate for the decay of state i to state f can be different from the transition from f to i and requires the following conversion,

$$B(f \to i) = \frac{2J_i + 1}{2J_f + 1}B(i \to f)$$ (1.11)

To determine the reduced transition rate, the experimenter must determine the gamma-ray energy E_γ, the multipolarity $\pi\lambda$, and the half-life $t_{1/2}$ which is inversely proportional to the decay rate. For the most common electromagnetic transitions the following equations are often used as a shorthand:

$$B(E1) = \frac{0.435}{E_\gamma^3 t_{1/2,p}}e^2\text{fm}^2\text{MeV}^3\text{fs},$$ (1.12)

$$B(M1) = \frac{39.4}{E_\gamma^3 t_{1/2,p}}\mu_N^2\text{fm}^2\text{MeV}^3\text{fs},$$ (1.13)

and

$$B(E2) = \frac{564}{E_\gamma^5 t_{1/2,p}}e^2\text{fm}^4\text{MeV}^5\text{ps}.$$ (1.14)

The subscript p signifies that $t_{1/2,p}$ is the partial half-life of the state. The quantity $t_{1/2,p} = t_{1/2}/b$ for cases in which a state may decay via multiple branches where b is the branching ratio. Reduced transition rates are often compared with the Weisskopf estimate [7]. The Weisskopf estimate for a reduced transition rate uses the limit of single-particle behavior of one nucleon. For measured reduced transition rates that are much larger than the Weisskopf estimate, the transition is considered to involve the collective motion of many nucleons. The Weisskopf estimate is defined as

$$B_W(E\lambda) = \left(\frac{1}{4\pi}\right)\left[\frac{3}{(3+\lambda)}\right]^2 (1.2A^{1/3})^{2\lambda} e^2 \text{fm}^{2\lambda} \tag{1.15}$$

for electric transitions, and

$$B_W(M\lambda) = \left(\frac{10}{\pi}\right)\left[\frac{3}{(3+\lambda)}\right]^2 (1.2A^{1/3})^{2\lambda-2} \mu_N^2 \text{fm}^{2\lambda-2} \tag{1.16}$$

for magnetic transitions.

Reduced transition rates can probe the nuclear structure effects that have been discussed so far such as shell closures and collective modes. The $B(E2)$ value for the 0_1^+ to 2_1^+ transition in even-even nuclei shows the existence of closed shells. Figure 1.5 shows the $B(E2; 0_1^+ \rightarrow 2_1^+)$ value for argon isotopes from ^{32}Ar to ^{48}Ar [8]. The $B(E2)$ value is minimized for the closed shells of neutrons at $N = 20$ and $N = 28$. For these magic nuclides, transitioning from the 0_1^+ state to the 2_1^+ state requires the breaking of a closed shell, which hinders the transition rate. Between the closed shells, the $B(E2)$ value is maximized (see Fig. 1.5). Thus, a large $B(E2)$ value is a signature of collective behavior away from closed-shell structures. The ratio of $B(E2)$ values for the $4^+ \rightarrow 2^+$ transition and the $2^+ \rightarrow 0^+$ transition also probes the
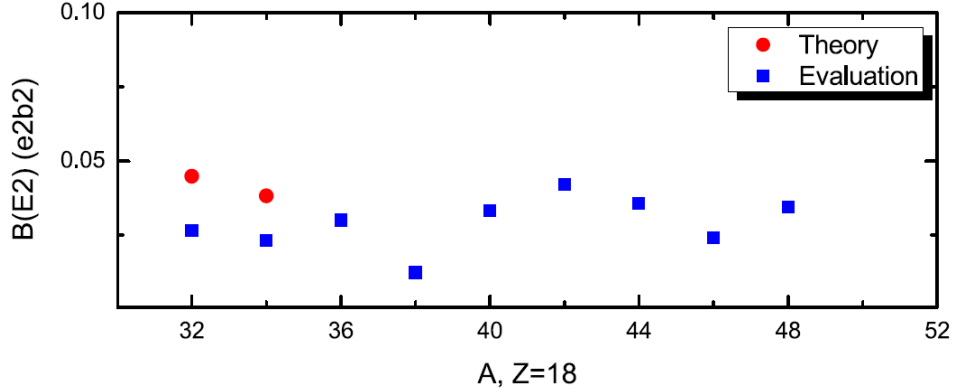
Figure 1.5: $B(E2; 0^+_1 \to 2^+_1)$ values for argon isotopes, adapted from Ref. [8] . The $B(E2)$ value is minimized for isotopes with a conventional magic number of neutrons, $N = 20$ or $N = 28$.

collective nature of the band of those states. $B(E2; 4^+ \to 2^+)/B(E2; 2^+ \to 0^+) = 2.0$ is expected for a vibrational band and $B(E2; 4^+ \to 2^+)/B(E2; 2^+ \to 0^+) = 1.43$ is expected for a symmetrically-deformed rotational band [3].

1.5   Islands of Inversion

The magic numbers were first introduced to explain observations about nuclei near stability [9]. As experiments have expanded the library of nuclear physics data to more unstable nuclides, it has been seen that the magic numbers do not remain static for all nuclides [10]. Near stability, the magic numbers indicate closed shell which support spherical shapes, enhanced stability, and first excited states with large energies and low transition rates in even-even nuclides. Regions with a conventional magic number where the nuclides do not exhibit the effects of a shell closure but instead behave more like mid-shell collective nuclides are called islands of inversion. Islands of inversion have been proposed in neutron-rich regions for many magic numbers such as $N = 8, 20, 28, 40$, [11–18] and more recently at 50 [19]. Generally, the islands of inversion occur when the large shell gap that exists for magic nuclides

near stability is suddenly reduced or is overcome by proton-neutron correlations in nuclides with extreme excesses of protons or neutrons. The physical mechanisms underlying these changes have been suggested to be the tensor component of the proton-neutron interaction and the three-body effective forces [10, 20–22].

The existence of an island of inversion was first postulated to explain the unexpected excess binding energy for neutron-rich isotopes near the $N = 20$ magic number [23–25]. The evidence for the $N = 20$ island of inversion can also be seen in the energy trend of 2^+_1 excited states in even-even nuclides as shown in Fig. 1.6. For $N = 20$ nuclides close to stability, the
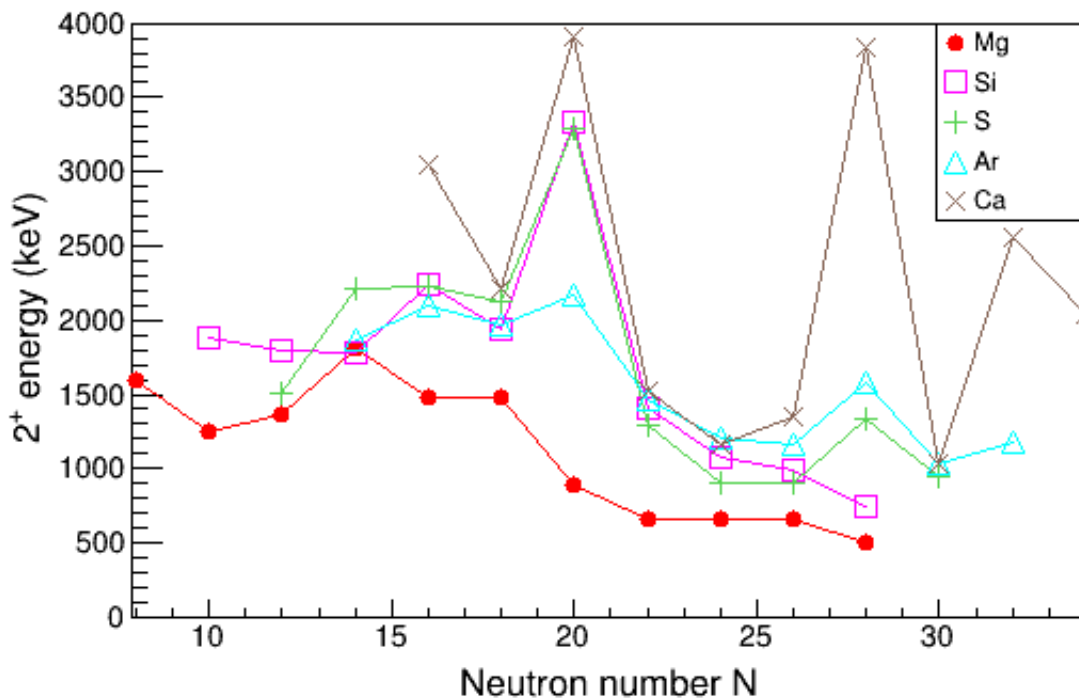
Figure 1.6: The energy of the first 2^+ states in even-even nuclides. For many nuclides with the magic number $N = 20$ or $N = 28$ the first 2^+ energy is larger than the neighboring even-even isotopes. This is not the case for ^{32}Mg at $N = 20$ and for ^{40}Mg and ^{42}Si at $N = 28$.

2^+_1 energy is larger compared to the neighboring even-even isotopes. This trend is broken for ^{32}Mg, the most neutron-rich $N = 20$ isotone shown in Fig. 1.6. The breakdown of the

$N = 28$ magic number can also be seen in this plot at ^{40}Mg and ^{42}Si.

The conventional $N = 20$ magic number is a result of the large shell gap between the neutron sd shell and the neutron pf shell. This supports the normal neutron configuration in which zero neutrons are promoted to the pf shell, leaving zero holes in the sd shell. This is also called the zero-particle-zero-hole or 0p0h configuration. The intruder configurations are those in which pairs of neutrons are excited from the sd shell to the pf shell. These are the two-particle-two-hole (2p2h) configurations, four-particle-four-hole (4p4h) configurations, etc. These intruder configurations are not favored near stability due to the large energy needed to cross the sd-pf shell gap. Moving from ^{34}Si to ^{32}Mg, two protons are removed from the proton $d_{5/2}$ orbital. This causes a sudden reduction in the contribution from the proton-neutron $\pi d_{5/2} - \nu d_{3/2}$ interaction, reducing in the sd-pf shell gap [10]. This allows intruder configurations to become preferred in ^{32}Mg.

1.6   Collectivity in ^{32}Mg

The ^{32}Mg nuclide has $Z = 12$ and $N = 20$. According to the magic numbers near stability, ^{32}Mg should be magic as well. However, ^{32}Mg is neutron rich and within the $N = 20$ island of inversion which was first identified from the mass measurements of neutron-rich Na isotopes [23]. Evidence for the inclusion of ^{32}Mg in the island of inversion also came from a mass measurement [26] which noted the same signature of excess binding energy as observed in the neutron-rich Na isotopes. Additionally, the low energy of the 2_1^+ state of ^{32}Mg at 885 keV suggested a deformed shape [14].

The unexpected binding in the $N = 20$ island of inversion was reproduced in Hartree-Fock calculations which suggested the deformation in this region was due to the filling of

negative parity orbitals from the neutron $0f_{7/2}$ level [27]. Shell model calculations performed in only the sd shell could not reproduce the experimental results for the neutron-rich Na and Mg isotopes [25]. By including orbitals from both the sd shell and the pf shell, the shell model calculations were more successful [24, 28–30]. Shell model calculations using the sd and pf shells have been extended to make predictions across the the entire $N = 20$ island of inversion [20, 21, 31, 32]. Beyond mean field calculations have successfully described this region as well [33, 34].

Several experiments have probed the possible deformation of ^{32}Mg by measuring the reduced $E2$ transition rate between the 0_1^+ and 2_1^+ states. An intermediate-energy Coulomb excitation reaction was used to make the first measurement which found the result of $B(E2; 0_1^+ \rightarrow 2_1^+) = 454(78)\ e^2\text{fm}^4$ [12]. This result was consistent with the available shell model calculations that include both sd and pf shells. The measurement was apparently confirmed by Ref. [35] which found $B(E2; 0_1^+ \rightarrow 2_1^+) = 440(55)\ e^2\text{fm}^4$ and interpreted ^{32}Mg as being dominated by $2\hbar\omega$ configurations, i.e., configurations with two neutrons across the $sd\text{-}pf$ shell gap. Shortly after, two additional measurements were made of the reduced $E2$ transition rate, one reporting a larger value of $B(E2; 0_1^+ \rightarrow 2_1^+) = 622(90)\ e^2\text{fm}^4$ [36], and one reporting $B(E2; 0_1^+ \rightarrow 2_1^+) = 449(53)\ e^2\text{fm}^4$ [37] in very good agreement with the first two measurements [12, 35]. More measurements of the reduced transition rate have been made with Coulomb excitation reactions [38, 39], and a fast-timing lifetime measurement has also been reported [40] which was used to deduce the $B(E2)$ value. None of these later results agree with the large $B(E2)$ value from Ref. [36]. The Coulomb excitation results of Refs. [35, 38] have discussed the role of feeding contributions from higher-lying states and report a feeding-corrected $B(E2; 0_1^+ \rightarrow 2_1^+)$ value near $350\ e^2\text{fm}^4$. Despite the variation in the measurement of the $B(E2)$ value they all agree that the $B(E2)$ is larger in ^{32}Mg than

in the neighboring even-even ^{30}Mg nuclide, indicating the onset of deformation in ^{32}Mg. Nevertheless, the large range of the $B(E2; 0_1^+ \rightarrow 2_1^+)$ results leaves uncertainty in the degree of the deformation in ^{32}Mg. To understand the deformation in the ground-state band of ^{32}Mg, it is necessary to find a conclusive $B(E2; 0_1^+ \rightarrow 2_1^+)$ value that sufficiently accounts for feeding effects. It would be useful to have a model-independent measurement of the 2_1^+ lifetime that is precise enough to resolve the different $B(E2; 0_1^+ \rightarrow 2_1^+)$ results.

The 4_1^+ state of ^{32}Mg is also important to consider. The decay of this state was first observed in a beta-decay experiment [41] but it was not until the later work of Ref. [42] that assigned it to ^{32}Mg in coincidence with the 885-keV $2_1^+ \rightarrow 0_1^+$ transition. Later, a proton inelastic scattering experiment established the 4_1^+ assignment [43]. Along with the reported measurement of the 6_1^+ state, the ground-state band has been suggested to be a deformed rotational band [44]. So far no $B(E2)$ value has been reported for the $4_1^+ \rightarrow 2_1^+$ transition, but this measurement could provide crucial evidence for the deformed rotor interpretation of ^{32}Mg. Using the expected ratio of reduced $E2$ transition rates in a deformed band ($B(E2; 4_1^+ \rightarrow 2_1^+)/B(E2; 2_1^+ \rightarrow 0_1^+) = 1.43$) and a $B(E2; 2_1^+ \rightarrow 0_1^+)$ estimated to be 90 e^2fm^4 from the measurements discussed in the previous paragraph, the symmetric deformed rotor interpretation suggests $B(E2; 4_1^+ \rightarrow 2_1^+) = 129$ e^2fm^4. This corresponds to a 4_1^+ lifetime estimate of $\tau = 1.0$ ps. Alternatively, for a vibrational band the expected ratio is $B(E2; 4_1^+ \rightarrow 2_1^+)/B(E2; 2_1^+ \rightarrow 0_1^+) = 2.0$, leading to a $B(E2; 4_1^+ \rightarrow 2_1^+) = 180$ e^2fm^4 and a lifetime of $\tau = 0.7$ ps. Therefore, the lifetime of the 4_1^+ state can be used to distinguish between collective modes in the ground-state band of ^{32}Mg.

The properties of ^{32}Mg discussed so far are consistent with an inversion between the intruder 2p2h configurations and the normal 0p0h configuration. In this picture, the ground-state band is dominated by 2p2h configurations and a band built on a higher-lying 0^+

state should be dominated by the 0p0h configuration. The 0_2^+ state was first observed ten years ago at 1058 keV in a (t, p) two neutron transfer reaction [13]. This experiment reconstructed the ^{32}Mg reaction product energy to distinguish the excited state at 1058 keV. The angular distribution of recoiling protons was used to deduce the spin-parity assignment of 0^+. Gamma rays in coincidence with the population of the 0_2^+ state indicated that the 0_2^+ state decays to the 2_1^+ state with a transition energy of 172 keV. However, the low intensity of these gamma rays indicated that the 0_2^+ state has a long lifetime ($\tau > 10$ ns). Initially, the properties of the 0_2^+ state were considered to be additional evidence for the mixing of the 0p0h and 2p2h configurations. However, later analyses indicated that the intruder 4p4h configurations were necessary to explain the energy, the long lifetime, and the (t, p) reaction cross section of the 0_2^+ state [13, 45, 46]. This is in agreement with the importance of the 4p4h configurations suggested in recent shell-model studies [20, 21]. Since the first observation, the 0_2^+ state has not been confirmed and its lifetime remains largely unconstrained. The importance of the 0_2^+ state in understanding the contribution of intruder configurations such as the 4p4h configurations merits additional measurements of the state energy and lifetime.

The work presented in this dissertation has tried to characterize the collective properties driven by intruder configurations in ^{32}Mg with new experimental observations. First, with a model-independent lifetime measurement of the 2_1^+ state, the $B(E2)$ discrepancy from past measurements can be resolved. This is also an important quantity for distinguishing between theoretical calculations. Second, the lifetime measurement of the 4_1^+ is another goal since this can provide additional insight about the collective nature of the ground-state band. Finally, the 0_2^+ state should be explored again to confirm the existence of this state and provide unique insights on the contribution from intruder configurations on the collectivity in ^{32}Mg. Ultimately, with these new measurements, a clearer picture of the collectivity in

^{32}Mg should be apparent.

Chapter 2

Experimental Techniques

The observations presented in this dissertation are from an experiment studying the in-flight decays of excited states in ^{32}Mg. The experiment has the following brief outline. A rare-isotope beam of ^{34}Si is produced from a stable beam of ^{48}Ca ion with fragmentation reactions on a ^{9}Be target. The ^{34}Si rare-isotope beam is delivered to the secondary ^{9}Be target where it undergoes two-proton removal reactions resulting in ^{32}Mg. The ^{32}Mg reaction products are produced in excited states and continue to move at relativistic velocities along the beamline. Gamma rays are emitted from the ^{32}Mg ions as they decay in-flight to lower-energy states. Ultimately, each positively identified ^{32}Mg reaction product is associated with the gamma rays observed in coincidence.

This chapter describes the details of several of the techniques used in this experiment. First, this chapter provides a discussion of gamma-ray spectroscopy since the observation of gamma rays emitted from in-flight decays is the basis for the lifetime measurement techniques which are used in this dissertation. Then, the lifetime measurement techniques used in this work are described, including the Doppler-shift Attenuation Method, the Recoil-distance Method, and the novel Cascade Doppler-shift Method. The last section of this chapter discusses the properties of the direct reaction mechanism that is used in this experiment to produce ^{32}Mg.

2.1 Gamma-ray Spectroscopy

The gamma-ray decay of a nucleus causes a change of energy in the nucleus which is equal to the energy of the emitted gamma ray[1]. By measuring the energy of the emitted gamma ray, the excitation energy of the nuclear states can be reconstructed.

2.1.1 Gamma-ray Interactions in Matter

The three most relevant interactions between gamma rays and matter for this experiment are photoelectric absorption, Compton scattering and pair production. Each of these interactions results in the transfer of energy from the gamma ray to the absorbing material. If all energy is transferred from the gamma ray it vanishes. If the gamma ray survives with a portion of its original energy, it is deflected in a new direction and can interact again at another location in the material. The greater the mass attenuation coefficient μ/ρ for a given interaction, material, and gamma-ray energy, the more likely it is for the interaction to take place. The mass attenuation coefficients for gamma rays in sodium iodide are shown in Fig. 2.1 for various interactions [47]. For gamma rays with less than about 250 keV of energy, photoelectric absorption is the most likely interaction. Between energies of 250 keV and 7 MeV, Compton scattering is most likely. For high-energy gamma rays above 7 MeV, pair production is most likely. A common scenario for a gamma ray detected in the present experiment is a series of Compton-scatter interactions until the remaining gamma-ray energy is low enough that a final photoelectric absorption takes place.

    In photoelectric absorption, the gamma ray transfers all of its energy to an absorber

---

[1]The nucleus also recoils and carries away part of the energy difference between the two states as kinetic energy, but the kinetic energy of the nucleus is small compared to the energy of the gamma ray for the systems discussed in this work.
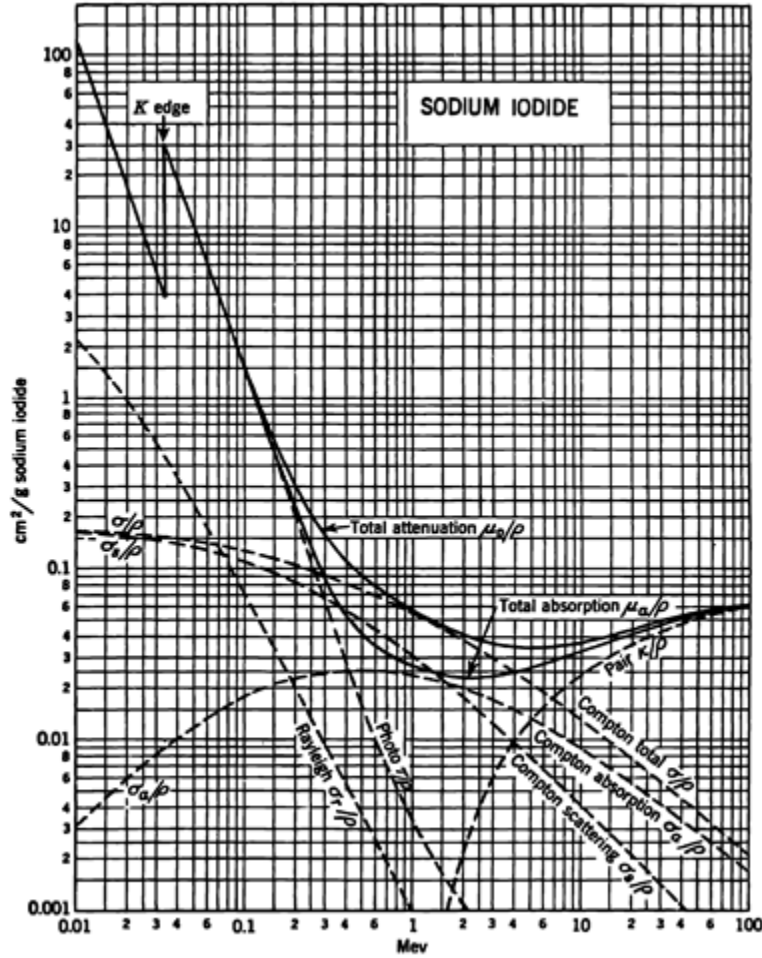
Figure 2.1: The mass attenuation coefficients for gamma-ray interactions in sodium iodide. Photoelectric absorption, Compton scattering and pair production interactions account for nearly all of the attenuation. The figure is from Ref. [47].

atom [48]. The energy deposited into the atom removes an electron from binding. Any energy from the gamma ray that is in excess of the electron binding energy provides the electron with initial kinetic energy. The gamma rays of interest in this experiment were all above 100 keV in energy so the ejected electron carries away most of the gamma-ray energy as kinetic energy, and the energy lost to unbind the electron is negligible. The likelihood of photoelectric absorption increases with proton number by Z^n where n is between 4 and 5. High-Z materials are often used in gamma-ray detectors to enhance the likelihood of photoelectric absorption.

In Compton scattering, the gamma ray scatters off an electron in the material [48]. The gamma ray transfers only a portion of its energy and is deflected by the angle θ relative to its incoming trajectory. The remaining energy of the gamma ray is

$$E' = \frac{E}{1 + \frac{E}{m_0 c^2}(1 - \cos\theta)} \qquad (2.1)$$

where E is the initial energy of the gamma ray, and m_0 is the electron rest mass. Eq. 2.1 is true for gamma rays that Compton scatter with a free electron. For the more likely case of Compton scattering with an electron bound in an atom, the binding energy of the electron must be included, but this is small enough that Eq. 2.1 can be reliably used [48].

Pair production can only occur for gamma rays with energy above 1.02 MeV. In this interaction the gamma ray is fully absorbed to create an electron-positron pair. Any gamma-ray energy that is greater than 1.02 MeV contributes to the kinetic energy of the pair. The positron can then annihilate with another electron in the material which generates a subsequent pair of gamma rays with energy of 511 keV.

When these gamma-ray interactions occur in a detector, they result in free energetic electrons inside the material. These electrons cause an electric signal which is proportional to the energy deposited by gamma rays. Through the observation of this electric signal, the gamma-ray energy can be measured.

2.1.2 Relativistic Doppler Shift

Gamma rays which are emitting from a source that is moving in-flight relative to a stationary observer experience Doppler shift. This is a result of the fundamental wave-like nature of photons and special relativity. Two observers which are moving relative to one another will

disagree on the measured frequency of a gamma ray, and thus the energy. This is the case for in-flight nuclear experiments. The laboratory itself including the gamma-ray detectors are considered stationary compared to the nucleus which is moving at relativistic speeds. Any gamma rays emitted from the in-flight nucleus will be emitted with energy that is Doppler-shifted in the laboratory frame.

The Doppler-shifted energy observed in the laboratory frame of reference is

$$E_S = \frac{E_U}{\gamma} \frac{1}{1 - \beta \cos \theta} \qquad (2.2)$$

where E_U is the unshifted energy of the gamma ray in the frame of the ion, β is the velocity of the ion relative to the speed of light c, and θ is the angle between the trajectory of the ion and the direction of emission of the gamma ray. γ is the Lorentz factor

$$\gamma = \frac{1}{\sqrt{1 - \beta^2}}. \qquad (2.3)$$

The ion-frame energy E_U is often the quantity of greatest interest since it is used to find the excitation energy of the nuclear states. To determine E_U from the observed lab-frame energy E_S, a Doppler-shift correction must be applied which is the inverse of the Doppler shift in 2.2,

$$E_U = E_S \gamma (1 - \beta \cos \theta). \qquad (2.4)$$

To obtain the energy between two states of an isotope moving at relativistic speeds, it is necessary to measure not only E_S, but also β and θ. The instruments used to measure these quantities are described in Chapter 3.

The resolution of E_S varies depending on the gamma-ray detector being used and often

comes at a trade-off with efficiency. Excellent gamma-ray energy resolution can be obtained by using high-purity germanium detectors [49]. For gamma rays emitted in-flight, the uncertainties in β and θ lead to error in E_U which is larger than the error in E_S and is known as Doppler broadening. The angle θ can have several different sources of error. The position uncertainty of the gamma-ray interaction is a source of error in θ. Since θ depends on the position and trajectory of the ion when the gamma ray is emitted, the uncertainty in θ is also affected by any uncertainty in the ion position and trajectory. The lifetime of the excited state contributes to the error in θ since the reaction products will travel different distances before decaying. Sources of error in β come from the momentum distribution of the reaction product, and additional momentum broadening can be caused as the product passes through a material. β can be measured by detectors downstream of the gamma-ray emission.

While the Doppler-shift of gamma rays emitted in-flight is often a challenge for detection, the Doppler-shift effect can actually be a valuable property for many lifetime measurement techniques. As mentioned in the previous paragraph, the lifetime of an excited state causes in-flight reaction products to decay at various positions along the beamline, changed the angle θ in Eq. 2.2 event-by-event. The gamma-ray energy spectrum can be sensitive to the lifetime of the excited state based on the distribution of these decay positions. This method of analyzing the lifetime is called the lineshape method and more details can be found in Ref. [50]. Other lifetime measurement techniques cause the parameter β in Eq. 2.2 to depend on the lifetime. This is done by placing degrader or stopper foils in the path of the recoiling ion. The ion slows as it moves through the material so that in-flight decays occur at a β that depends on the amount of material the ion has passed through, and hence depends on the lifetime. This is the premise of methods such as the Recoil-distance Method and the Doppler-shift Attenuation Method [51].

27

2.2 Lifetime Measurement Techniques

The excited states of a nucleus can spontaneously decay, transitioning to another state. A sample of N_0 nuclei will decay according to the law of radioactive decay

$$N(t) = N_0 e^{-t/\tau} \tag{2.5}$$

where τ is the lifetime of the state. Two different nuclear states are connected by an operator $\hat{O}$ which is related to the lifetime of the initial state

$$\frac{1}{\tau_i} \propto \|\langle \psi_f \| \hat{O} \| \psi_i \rangle\|^2. \tag{2.6}$$

Therefore, lifetimes are connected to the fundamental radioactive nature of nuclear states, and can provide an understanding of the transition strength between two states. The transition strengths in turn can illuminate profound nuclear structure properties such as collectivity, configuration mixing, and shape coexistence.

The lifetime of an excited state can span orders of magnitude from 1 attosecond to thousands of years. Many sensitive techniques shown in Fig. 2.2 have been developed to measure lifetimes throughout this range [51]. It is necessary to use different techniques for measuring different ranges of lifetimes. When possible, the direct methods shown in Fig. 2.2 are preferred because they do not rely on external inputs from theoretical calculations.

The details of lifetime measurement techniques used in this dissertation are discussed in the following sections. The discussions cover the Doppler-Shift Attenuation Method, the Recoil-distance Method, and the Cascade Doppler-shift Method which is a novel technique designed to study isomers decaying in-flight.
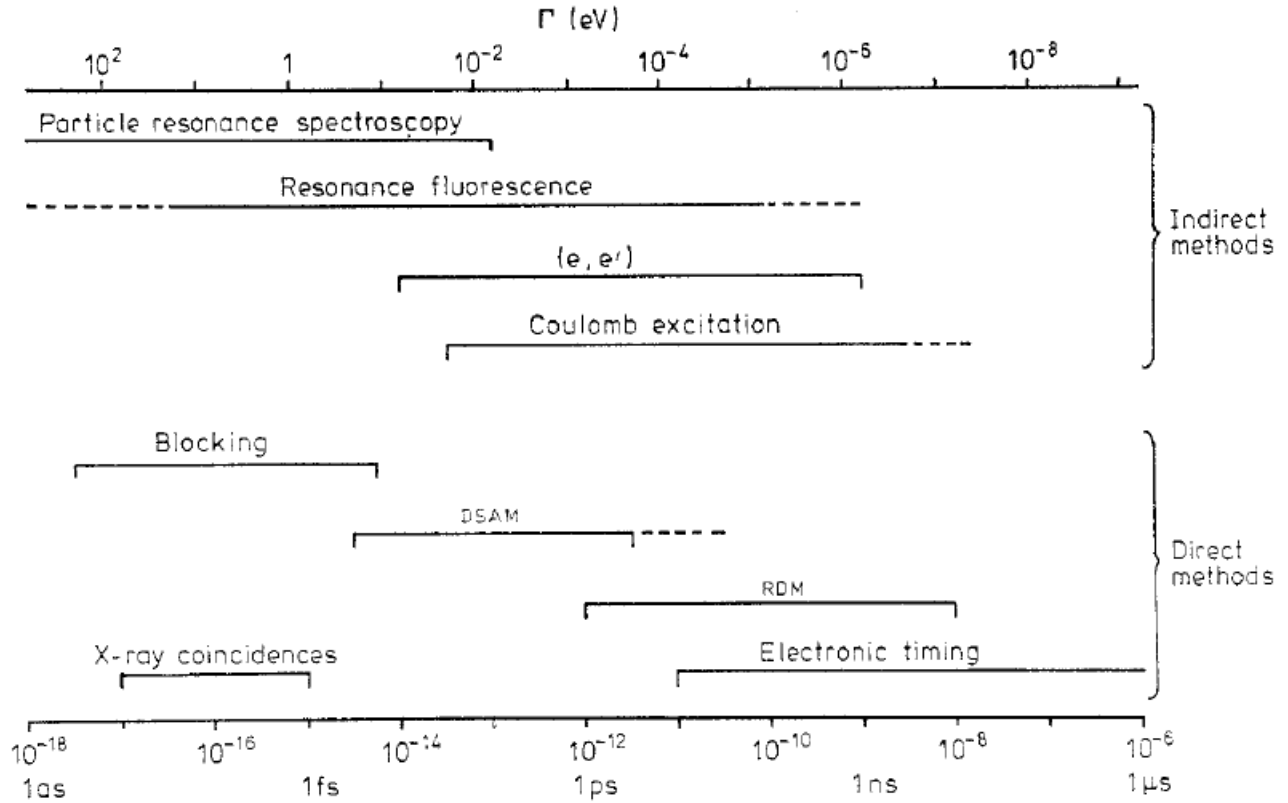
Figure 2.2: A depiction of the methods used to measure the lifetimes of excited states. The figure is from Ref. [51].

2.2.1 Doppler-shift Attenuation Method

The Doppler-shift Attenuation Method (DSAM) can be applied to measure lifetimes ranging from 1 fs to a few ps. DSAM relies on the slowing of the nucleus as it travels through a material on the same time scale as the lifetime of the state of interest. The moving ion emits gamma rays that are Doppler-shifted according to Eq. 2.2. As the ion travels through a material the ion loses energy and slows. Often a stopper or backing is applied to the target to increase the energy loss of the reaction product shortly after it is produced. As the ion slows, the Doppler-shifted energy of the emitted gamma ray changes. If the lifetime of the excited state is on the same order as the time the ion spends slowing through the material, the Doppler-shifted gamma-ray energy results in a spectral shape that is sensitive to the

29

lifetime.

The analysis of DSAM data relies on understanding the slowing of the ion as it moves through the target and backing material [51]. The experimental average velocity $\bar{v}$ is found from the observed shift in the gamma-ray energy centroid

$$\bar{E}_s = E_0(1 + \bar{\beta}\cos\theta_\gamma) \tag{2.7}$$

at various angles θ_γ, where $\bar{\beta} = \bar{v}/c$. The experimental velocity is expressed as $F = \bar{v}/v_0$ and compared to a theoretical function $F(\tau)$ which is sensitive to the lifetime. To produce sufficient slowing of the ion in the backing foil, it is often practical to use a high-Z material such as tantalum or gold. One must have a precise understanding of the stopping power of the nucleus as it travels through the material to extract a precise lifetime from an observed DSAM gamma-ray energy lineshape. The stopping power is a result of numerous interactions including electron stopping with the atomic electrons of the material, and nuclear stopping with the nuclei of the material itself. This is a largely statistical process and many models of stopping power are available. Thus, the lifetime from a DSAM measurement is ultimately dependent on the choice of stopping power model which are based on experimental measurements of stopping powers. By varying any assumptions made in the stopping power model, a statistical distribution of the lifetime results can be found and used to evaluate the model-based uncertainty of the final result. In practice, these stopping power models can be included in a simulation that incorporates the other experimental conditions. The gamma-ray energy spectrum from the simulation can be directly compared to the experimental spectrum to determine the lifetime.

2.2.2 Recoil-distance Method

For lifetimes on the order of 1 ps to a few ns, the Recoil-Distance Method (RDM) can be an appropriate method, depending on the experimental setup. While in DSAM measurements a foil is placed immediately after the target, in RDM measurements, the second foil is positioned with a well-measured space between it and the target. Most decays in RDM measurements occur either between the target and second foil, or after the second foil where the ion is at a lower velocity. This method is practical for measuring lifetimes that are on the same order as the time it takes for the ion to traverse the gap between the two foils. The additional foil can either be used as a stopper where the ions come to rest, or a degrader where the ions are slowed but then continue along the beamline. For the experiment presented in this dissertation a degrader foil was used.

Often the detection of gamma rays is used to determine whether the decay occurred before or after reaching the second foil. Figure 2.3 shows a device called a plunger which is used to arrange the foils for an RDM measurement [52]. In this setup, the gamma rays are emitted with energy that is Doppler-shifted according to Eq. 2.2. The ion is moving at a greater velocity before reaching the second foil so gamma rays emitted in this region are emitted with greater lab-frame energy for detectors at forward angles. After reaching the second foil the ion velocity is reduced so the lab-frame energy for detectors at forward angles is also reduced. As a result, the gamma-ray energy spectrum has two components corresponding to the decays of fast-moving ions and slow-moving ions. This provides a measurement of the number of decays occurring before and after reaching the second foil.

The mathematical formalism for the RDM is outlined in Ref. [51]. The number of decays
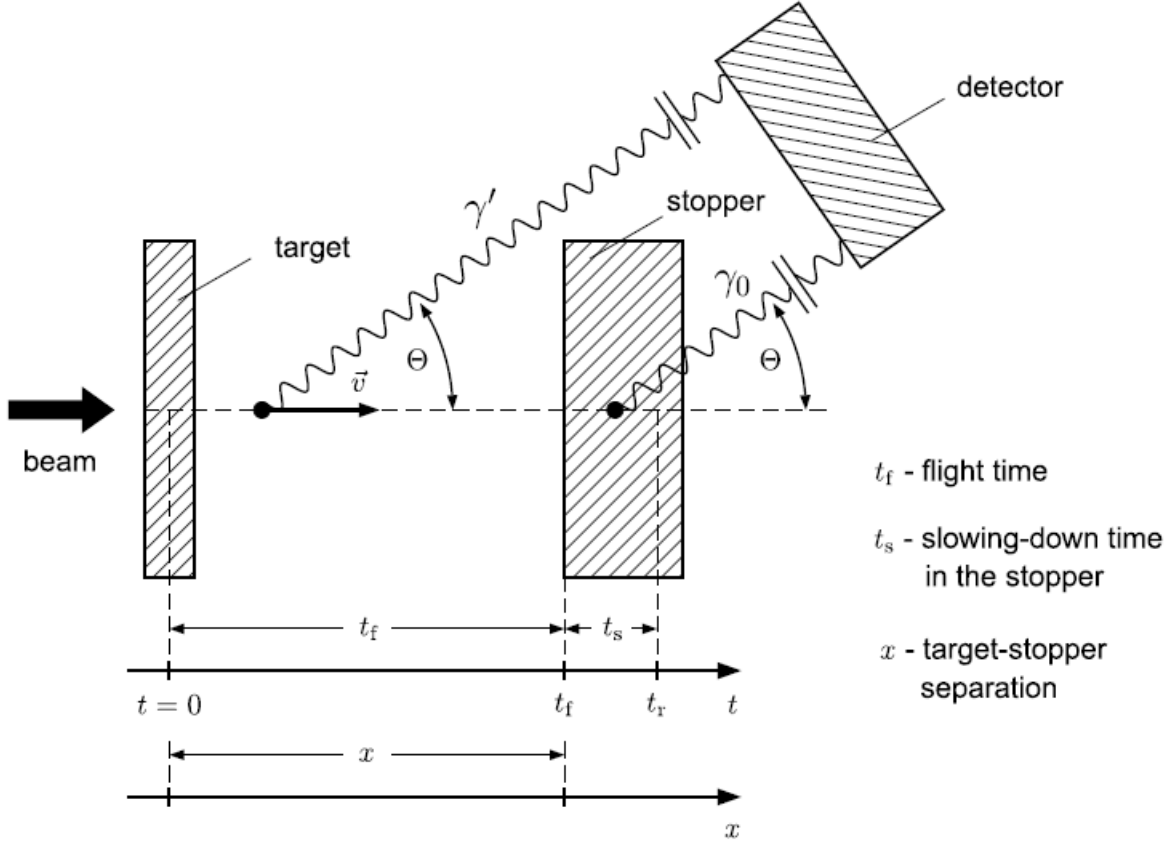
Figure 2.3: A schematic of a generic plunger device used in Recoil-distance Method (RDM) measurements. The image is from Ref. [52].

that occur while the ion is moving at the faster velocity before reaching the degrader is

$$I_f = N_0(1 - e^{-d/v\tau}) \tag{2.8}$$

where d is the distance the ions recoil and v is the velocity of the ion before the second foil. The number of decays at the slower velocity is

$$I_s = N_0 e^{-d/v\tau}. \tag{2.9}$$

Then, we can find the ratio

$$R = \frac{I_s}{I_f + I_s} = e^{-d/v\tau}. \tag{2.10}$$

The quantities v and d can be experimentally known, allowing the lifetime τ to be extracted.

There are numerous experimental complications that are not expressed in the above equations. For instance, the velocity is not the the same for each ion. The trajectory of the ion is not always a straight line through the center of the foils but makes an angle relative to the central beam axis. The gamma-ray energy spectrum also becomes complicated by in-flight decays occurring within the foils themselves and by the presence of neutron-induced background. In practice, these complications can be included in a simulation that reproduces the experimental configuration and makes an assumption about the lifetime of the excited state. By systematically modifying the lifetime assumption in the simulation, the physical value can be extracted by comparing the simulated gamma-ray energy spectrum to the experimentally observed spectrum.

The feeding of the excited state of interest provides a complication to any lifetime measurement. In the presence of strong feeding, the time for a state to decay does not reflect that state's lifetime, but instead reflects the total time for that state to decay, plus the time for each of the higher-lying feeding states. To correct for the feeding effect, one must know the amount of feeding present in the experiment, and the branching ratio and lifetime of any feeding state. These can be used in a system of equations that properly portray the population of the excited state as it is directly fed from the reaction, indirectly fed by the feeding states, and depopulated by its own decay. Equivalently, the simulation can be used to reproduce the feeding from these higher lying states if their feeding is well-understood.

2.2.3 Cascade Doppler-shift Method

For longer lifetimes ($\tau > 100$ ps) the decay does not occur near the reaction target. Therefore, an alternative approach is required to apply Doppler-shift corrections to emitted gamma rays. The novel Cascade Doppler-shift Method (CDM) described here has been developed to make Doppler-shift corrections and to measure lifetimes as well. The essential problem is to find another way to track the emission point of the gamma ray without relying on the assumption that the emission occurs near the target. When the gamma ray is a part of a cascade of gamma rays that are emitted nearly simultaneously (within $t \leq 100$ ps) it is possible to use the timing information of the cascade to locate the common decay position [53]. Another novel approach [54] is to use the energy information of the gamma-ray cascade to find the common decay position, which is now feasible using detectors with high gamma-ray energy and position resolution such as GRETINA [49].

In practice, we have a cascade of gamma rays γ_1 and γ_2 such as those shown in Fig. 2.4. In
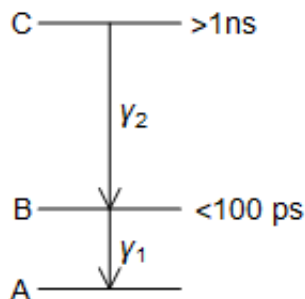
Figure 2.4: A generic level scheme in which the highest state C has an long lifetime and is followed by a cascade of gamma rays γ_1 and γ_2 involving a short-lived intermediate state B and a ground state A.

an in-flight experiment, these gamma rays are each Doppler-shifted in the laboratory frame according to their own emission angle, θ_1 or θ_2, as shown in Fig. 2.5. However, both gamma rays are emitted at a common velocity and from a common position. If the ion-frame energy
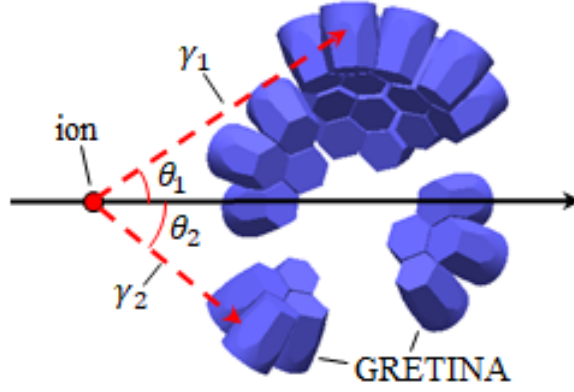
Figure 2.5: A generic experimental setup in which two gamma rays γ_1 and γ_2 are emitted at angles θ_1 and θ_2 from an in-flight ion and are detected. The gamma-ray detector array GRETINA is depicted here [49].

E_U of γ_1 is known, then the emission angle θ_1 can be found from the measured Doppler-shifted energy E_S and the ion velocity β using Eq. 2.2. Using the gamma-ray position information of a high-resolution detector such as GRETINA [49], the emission point of γ_1 can be determined. Since the state between γ_1 and γ_2 is short-lived (state B in Fig. 2.4), it can be assumed that γ_2 is emitted from the same location as γ_1. Then, it is possible to make a Doppler-shift correction to the observed lab-frame energy of γ_2 using the emission angle θ_2 and Eq. 2.4.

One key assumption in a CDM measurement is that both gamma rays are emitted from the same location. However, due to the non-zero lifetime of the state between the emission of the gamma rays (state B in Fig. 2.5), the ion does travel through a distance between the emissions of γ_1 and γ_2. This complication can be neglected if the lifetime of state B is short enough (< 10 ps). For longer lifetimes, the spectral lineshape of the peak corresponding the γ_2 is affected.

A practical difficulty of this method is that the gamma-ray cascade can be emitted at any position after the target, allowing θ_1 and θ_2 to take on any value. This causes the

35

lab-frame energies of γ_1 and γ_2 observed over many events to span a large range of values. This leads to a significant background contribution since *a priori*, every observed energy in the Doppler-shifted range of γ_1 must be treated.

The distribution of the common decay points for many cascade events provides a probe of the lifetime of the isomer (state C in Fig. 2.4). Longer lifetimes will result in a greater proportion of the cascade decays occurring far from the target while for shorter lifetimes, the decays points accumulate close to the target. For many applications, the observed distribution of decays along the beamline is coupled with the efficiency of the gamma-ray detector which is not uniform along the beamline. To account for this, precise information of the detector efficiency must be known at several points along the beam path. If a simulation that incorporates the true detector efficiency as a function of position is developed, it can be compared with the observed decay trend to extract the lifetime.

2.3   Direct Reactions

This section describes the properties of direct reactions that are relevant to the main reaction in this work, $^9\text{Be}(^{34}\text{Si}, {}^{32}\text{Mg})\text{X}$. Direct reactions are nuclear reactions which excite very few of the degrees of freedom of the system [55, 56]. One example of a direct reaction is the two-nucleon knockout reaction depicted in Fig. 2.6. The dynamics of the nucleus which losses two nucleons can be approximately treated by considering only the two removed nucleons and the remaining nucleus A. The complex behavior of the several individual nucleons within A can be neglected in a direct reaction.

The direct reaction is a valuable experimental tool because the reaction mechanism is sensitive to the wave functions of the few nucleons involved. One-nucleon removal reaction
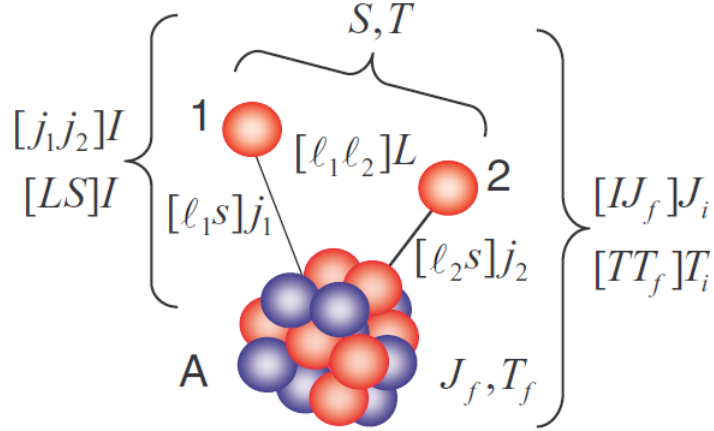
Figure 2.6: A depiction of a two-nucleon knockout reaction. The relevant angular momentum couplings are shown. This figure is from Ref. [56].

experiments have led to a more general understanding of nuclear halo systems [57]. A direct knockout reaction was used in the discovery of the proton bubble in ^{34}Si [58].

It has been shown that two-nucleon knockout reactions act as a direct reaction [59], indicating the sensitivity of this reaction to the wavefunctions of the two removed nucleons. In the present experiment, two-proton knockout is used to populate neutron-rich ^{32}Mg from the parent nucleus ^{34}Si. The two-proton knockout reaction should primarily affect the two removed protons, leaving the remaining nucleons mostly unaffected. The ground state of ^{34}Si is considered to have a closed shell structure [31, 60] which makes direct reactions from ^{34}Si suitable to probe the wavefunction of states in ^{32}Mg. The final states in ^{32}Mg with the largest overlap with the closed-shell ground state of ^{34}Si are expected to have the greatest cross section. This provides a criteria to determine the relative amount of normal and intruder configurations in states of ^{32}Mg.

Chapter 3

Setup and Calibration of

Experimental Devices

The results in this dissertation are from an experiment performed at the National Superconducting Cyclotron Laboratory (NSCL) in 2017 to study collectivity in ^{32}Mg by measuring the lifetimes of excited states. The excited states of interest include the yrast 2_1^+ and 4_1^+ states which have short lifetimes ($\tau < 100$ ps) and the isomeric 0_2^+ state which has a long lifetime ($\tau > 10$ ns [13]). Due to the large difference in the lifetimes involved in this study, it was necessary to use two experimental setups at the target chamber that were each optimized for a different lifetime range. The experimental devices present in the beamline before and after the target chamber were the same between the two experimental setups. In this chapter, the common experimental devices are described, then the different target chamber configurations are explained. The relevant calibrations of the experimental devices is also explained in this chapter.

The experiment in question involves a direct reaction with a rare-isotope beam. There are only a handful of facilities available in the world that can support such experiments and the NSCL is one of them. Several different devices are required to work in tandem to result in a successful experiment. For this experiment, this included the following devices: the Superconducting Source for Ions (SuSI) [61], the coupled cyclotrons K500 and K1200 [62, 63],

the A1900 fragment separator [64], and the S800 spectrograph [65]. The measurement of gamma rays is crucial for the measurement of excited state lifetimes and in this experiment was managed with GRETINA [49, 66] which is discussed in a later section of this chapter. For the measurement of the lifetimes of the yrast states, the TRIPLEX device was used.

3.1   Superconducting Source for Ions (SuSI)

The Superconducting Source for Ions (SuSI) [61] was used to ionize atoms of ^{48}Ca to be used in the primary beam of this experiment. A metallic source of ^{48}Ca was placed in an oven and heated until gaseous ^{48}Ca atoms could escape and can be used in the ion source. SuSI ionizes atoms under the principle of electron cyclotron resonance [67]. The ions and free electrons are trapped within a magnetic field. Both the ions and the electrons oscillate at their respective cyclotron frequencies

$$\omega_c = \frac{qB}{m} \tag{3.1}$$

where B is the strength of the transverse magnetic field and q and m are the charge and mass of the particle. Since an electron has far less mass than an ion, its cyclotron frequency is much greater. A resonance frequency (RF) field is applied to the gas at the cyclotron frequency of the electrons to increase their temperature without directly heating the ions which would cause more ions to escape the trap. The increased temperature of the electrons leads to more collisions between the ions and the electrons and causes more electrons to be ionized from the ion. Ions eventually escape the trap with a moderate charge state (^{48}Ca^{8+} in this experiment) and an electric field sweeps them to the K500 cyclotron.

3.2 The Coupled Cyclotrons, K500 and K1200

The cyclotron accelerators [68] K500 and K1200 are used to accelerate the ions produced by the ion source to velocities of up to 50% the speed of light for the primary fragmentation reaction. A cyclotron has a vertical magnetic field that is transverse to the direction of the ion motion. This sets the ions in a circular trajectory. The ions pass through electrodes called dees that each alternate between positive and negative charge over time at the RF of the ions. The ions experience steady acceleration from the dees throughout their motion. With increasing speed, the ion cycles at larger radii until it reaches the limit of the cyclotron and is guided out.

The K500 cyclotron receives partially ionized atoms from the ion source and accelerates them to roughly 10% the speed of light. Once emitted from the K500 cyclotron, the ions encounter a stripper foil which removes the remaining electrons from the ions. Now in their greatest charge state, the ions enter the K1200 and are accelerated further to 50% the speed of light. In this experiment, the ^{48}Ca primary beam reaches 140 MeV/nucleon. The primary beam is delivered to the ^{9}Be production target where it undergoes a fragmentation reaction.

3.3 A1900 Fragment Separator

The A1900 fragment separator [64] accepts the many species of reaction products from the primary fragmentation reaction and separates the secondary beam of interest from the rest. There are twenty-four superconducting quadrupole magnets and four superconducting dipole magnets in the A1900 fragment separator. The dipole magnets are tuned to the magnetic

rigidity of the desired secondary beam. The magnetic rigidity is

$$B\rho = \frac{mv\gamma}{q} \tag{3.2}$$

where m, v, and q are the mass, velocity, and charge of the ions which pass along the central trajectory of the fragment separator, $\gamma = \frac{1}{\sqrt{1-\beta^2}}$ is the Lorentz factor, B is the strength of the magnetic field created by the dipole magnets, and ρ is the bending radius.

While moving through the first half of the fragment separator, the magnetic rigidity in Eq. 3.2 depends only on the mass and charge of the ions. The velocity v is the same for all the fragmentation products since the primary beam ions exit the K1200 cyclotron with the same velocity, and velocity is approximately unchanged by the fragmentation reaction. Slits are placed at the exit of the first half of the fragment separator to select the desired mass to charge ratio A/Z for the secondary beam.

An aluminum wedge divides the first half of the fragment separator from the second and acts as a degrader. The ions pass through the wedge and lose energy proportional to the square of their atomic number. These ions now have different velocities in the second set of magnets. As a result, the magnetic rigidity of the ions is related to the mass and proton number of the ions by roughly $B\rho \propto A^{2.5}/Z^{1.5}$ [69]. This allows an isotopic selection in the second half of the A1900 fragment separator that is complementary to the selection made by the first half of the fragment separator. Another set of slits at the exit of these magnets is used to select the separated secondary beam of interest, which for this experiment was ^{34}Si. The secondary beam is then guided to the experimental hall where the experiment is carried out.

3.4 S800 Spectrograph

The S800 spectrograph shown in Fig. 3.1 is a superconducting spectrograph at the NSCL coupled-cyclotron facility [65, 70]. The S800 consists of an analysis line before the secondary
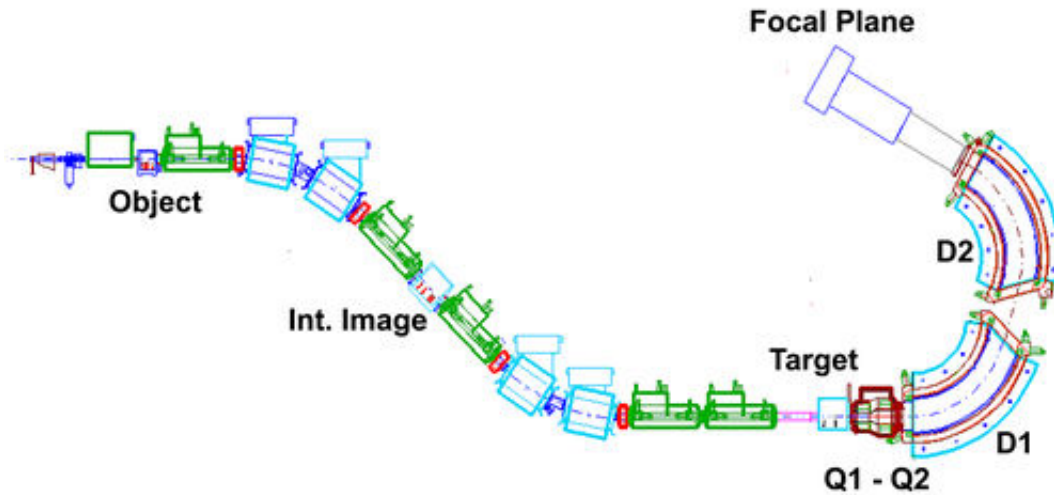
Figure 3.1: A schematic of the S800 spectrograph. The figure is from Ref. [70].

target position, and a spectrograph line after the secondary target. The secondary reaction occurs at the secondary target position, and reaction products continue into the spectrograph. In the spectrograph portion, the reaction products are focused by two quadrupole magnets. The trajectory of the reaction products are then bent along the dispersive axis by two dipole magnets and reach the focal plane of the S800.

At the focal plane, several detectors shown in Fig. 3.2 are used to identify the nucleus and measure its trajectory and momentum [70, 71]. The E1 scintillator is a plastic scintillator at the S800 focal plane used to measure the time-of-flight (TOF) of the nucleus. The position and angular trajectory of the nucleus are measured at the focal plane using a pair of cathode readout drift chambers (CRDC's). An ionization chamber is used to identify the Z of the nucleus based on the energy loss of the nucleus through the chamber. Finally, a CsI(Na) ho-
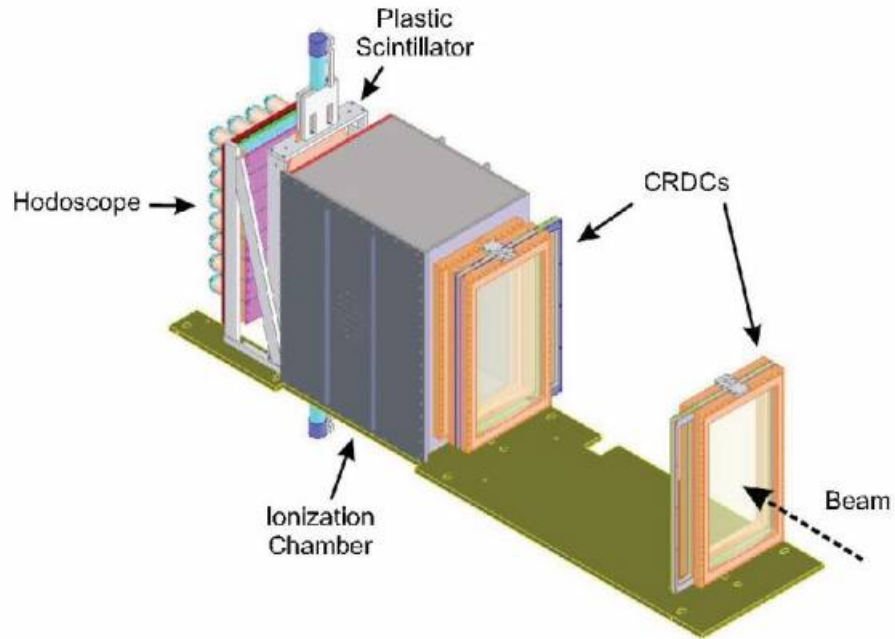
Figure 3.2: The S800 focal plane. The cathode readout drift chambers (CRDC's), plastic scintillator (E1 scintillator), ionization chamber, and IsoTagger hodoscope are depicted. The image is from Ref. [70].

doscope, called IsoTagger, is positioned at the end of the focal plane and, in this experiment, is used to observe gamma rays from isomers implanted in an aluminum stopper [72, 73].

The S800 supports two modes of operation: the focus mode which was used in this experiment, and the dispersion-matching mode. The focus mode is designed to deliver the secondary beam to the secondary target chamber with a small spatial focus (±0.5 cm) and allow a large momentum acceptance ($\Delta p/p = \pm2\%$) in the spectrograph. In focus mode the ion energy resolution is limited to roughly 1 part in 1000. In dispersion-matching mode the beam is momentum-dispersed at the target position leading to a large position distribution. As a result the momentum acceptance is reduced to $\Delta p/p = 0.5\%$ but the energy resolution

is improved to 1 part in 5000. The angular acceptance for secondary reactions at the target position is 100 mrad for both operation modes.

3.4.1 Cathode Readout Drift Chambers

Each of the two Cathode Readout Drift Chambers (CRDC's) shown in Fig. 3.3 is composed of cathode pads and an anode wire to measure the dispersive and non-dispersive positions of the reaction product. The volume of each CRDC is filled with gas consisting of 80% CF_4 and 20% C_4H_{10}. As a nucleus passes through a CRDC it ionizes atoms in the gas and the ionized electrons drift to the anode wire, while the positive charges drift to the cathode pads. Charge is collected on several of the pads. Instead of choosing the pad with the greatest
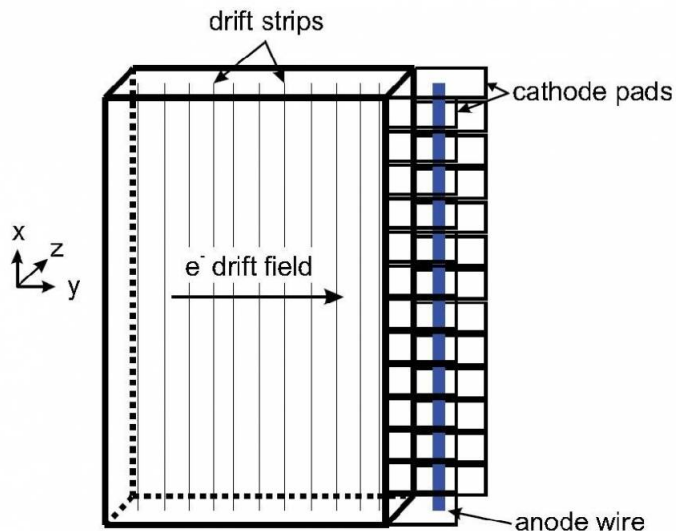
Figure 3.3: A schematic of a CRDC detector used in the S800 focal plane. The beam axis z, dispersive axis x, and non-dispersive axis y are shown. The image is from Ref. [70].

charge deposit as the location of the reaction product, the entire distribution is used to provide sub-pad resolution along the dispersive direction. The drift time of the electrons to

44

the anode wire is sensitive to the position along the non-dispersive direction. In this way, the first CRDC is used to obtain the x and y positions of the ion at the focal plane (x_{fp} and y_{fp}) relative to the central z-axis. The second CRDC is 1 m past the first CRDC and is used to find the angles a_{fp} and b_{fp} of the trajectory of the ion relative to the z-axis in the x and y directions, respectively. These coordinates are depicted in Fig. 3.4. The CRDC's
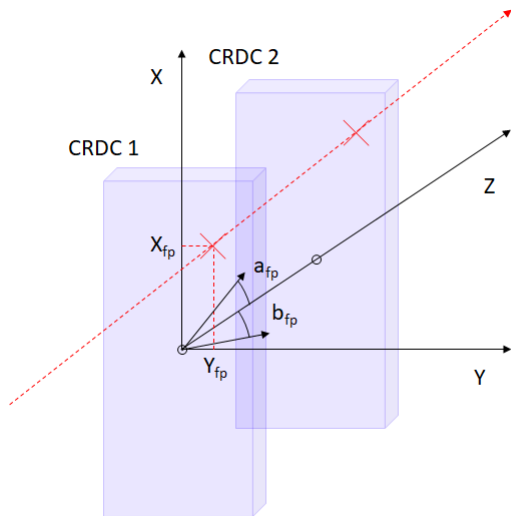
Figure 3.4: A schematic of the CRDC detectors used in the S800 focal plane and the position and angular information of the ion. The beam axis z, dispersive axis x, and non-dispersive axis y are shown. The first CRDC provides a measurement of the x and y position at the focal plane, x_{fp} and y_{fp}. The angle information a_{fp} and b_{fp} comes from the difference in the x and y positions between the two CRDC's.

are limited to a rate of about 5000 ions per second, mostly due to the long drift time of the positive ions.

The CRDC position and angle information is used to reconstruct the trajectory of the nucleus at the target position. This is done with the ion optics code COSY INFINITY to determine the transfer matrix S [74]. S represents the transformation of the ion parameters as it travels from the target position to the focal plane due to the S800 magnets and includes magnetic field aberrations up to the 5th order. The inverse matrix, S^{-1}, is used to map the parameters measured at the focal plane back to the parameters at the target position.

The parameters determined by the CRDC's at the focal plane are denoted x_{fp}, y_{fp}, a_{fp}, b_{fp}. Because the dipole magnets bend the beam in the x-direction, the x_{fp} parameter is used to determine the kinetic energy of the ion. As a result, the x-position of the ion at the target position is not known, but the kinetic energy is known. The parameters at the target position are the y-position y_{ta}, the angle of the trajectory in the x-direction a_{ta}, the angle in the y-direction b_{ta}, and the kinetic energy of the ion relative to the reference kinetic energy that would pass through the center of the S800 dipoles d_{ta}.

Each CRDC consists of 224 pads and each pad carries an electric signal. The signals of all the pads of a CRDC must be matched to one another by adjusting the voltage gain and offset. Three different isotope species that illuminate all the pads are used to calibrate all the gains and offsets. When they are properly calibrated, the CRDC pad energy for a single isotope appears as a straight line across all of the pads. The process is iterative, typically requiring fewer than five iterations to converge on final offset and gain values. An example of the uncalibrated and calibrated CRDC voltages for one isotope is shown in Fig. 3.5.

The cathode pad voltage and drift time information of each CRDC must be related to absolute values of x and y, respectively. This is done by placing an aluminum plate with holes at known positions in front of each detector. This aluminum plate is called a mask. The absolute position of the holes in each mask is known. During the experiment, a mask is placed in front of each CRDC one at a time and the secondary beam is delivered to the CRDC, illuminating only the positions on the pad where a hole in the mask is located. Figure 3.6 shows a typical depiction of a CRDC illuminated by ions passing through the holes of a mask. The known positions of these holes can then be associated with signals from the CRDC. A linear calibration consisting of a slope and an offset is used to relate the y (non-dispersive) position to the drift time of the signal. This calibration depends on
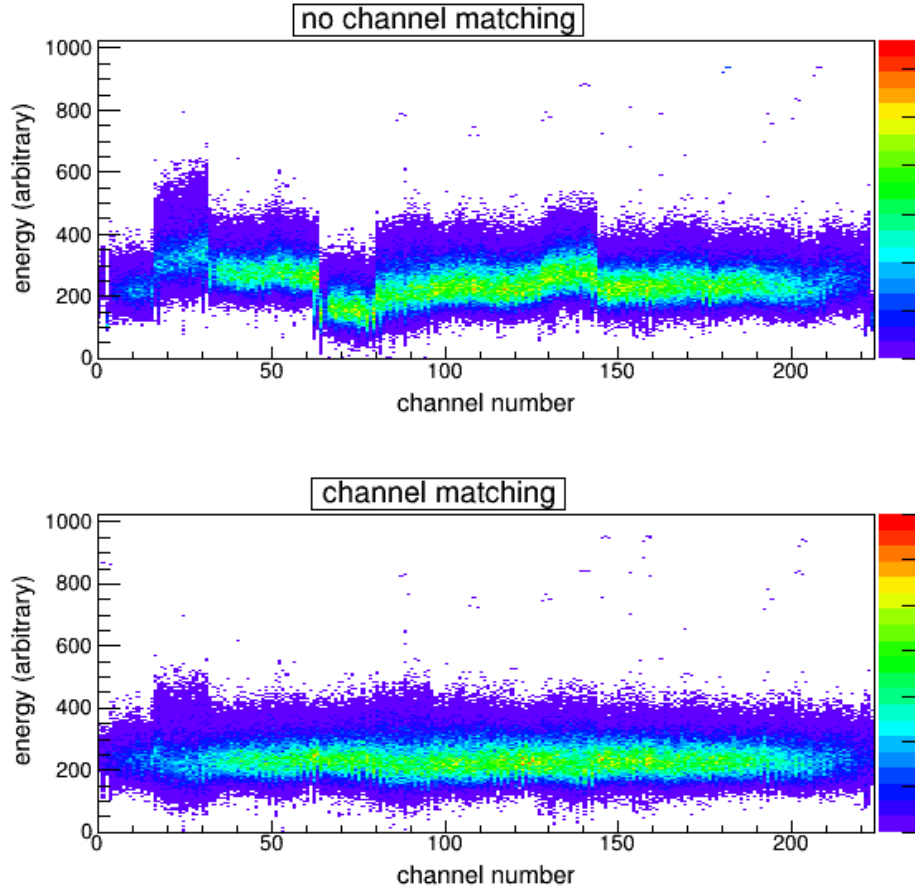
Figure 3.5: The 224 channels of each CRDC must have their signals matched so that there is no bias for a particular channel due to the variations in the gain of the electronics. The signal from the channels before matching is shown in the top spectrum for the first CRDC, and the signal from the same channels after matching is shown in the bottom spectrum. The events are for the incoming ^{34}Si secondary beam and ^{32}Mg reaction product observed at the focal plane.

the properties of the gas inside the CRDC's and can therefore change over the course of the experiment. An example of the calibration done for the non-dispersive direction is shown in Fig. 3.6. A mask calibration was performed just before lifetime data was taken with each of the target chamber setups. The x (dispersive) position is constrained by the known absolute position of the pads in the CRDC's, so the mask calibration is only used to confirm the linear calibration from the physical arrangement of the pads.

47
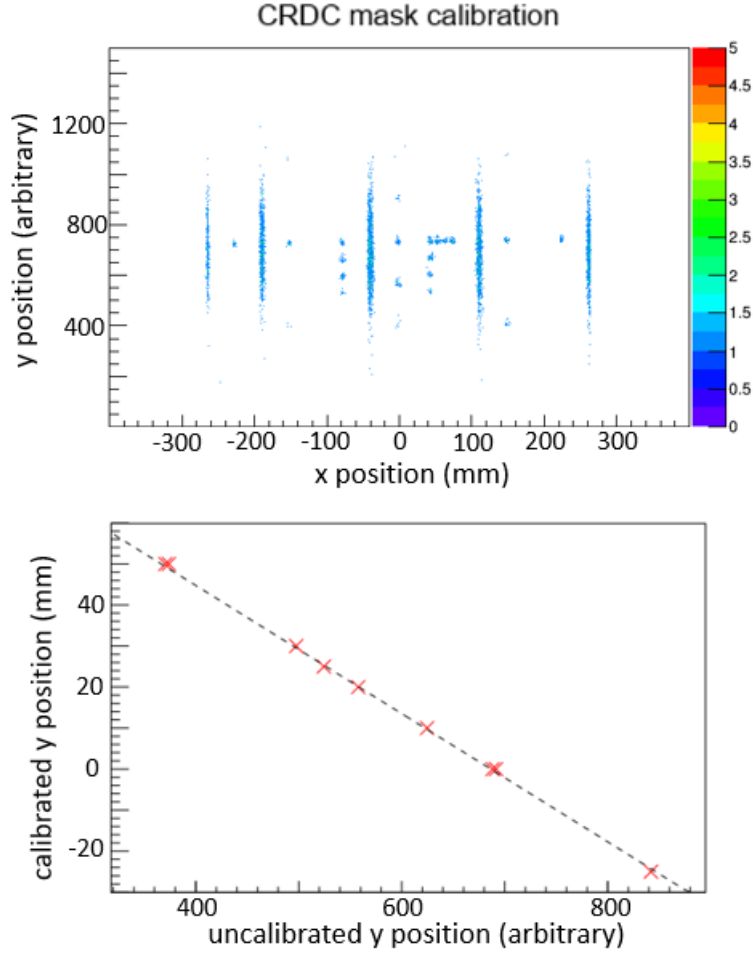
Figure 3.6: The top section shows the uncalibrated x and y positions of the first CRDC with the mask placed in front. The holes in the mask allow ions to pass through to the CRDC. The lower section shows the linear calibration between the raw position values ch and the calibrated positions y. The line is defined by $y = -0.156248ch + 107.28$

3.4.2 Ionization Chamber

The ionization chamber at the focal plane of the S800 measures the energy lost by the ion as it travels through the chamber. The stopping power is the energy lost per unit length by an ion passing through a medium and is described by the Bethe formula [48],

$$\frac{dE}{dx} = \frac{4\pi e^4 z^2}{m_0 v^2} NB \tag{3.3}$$

where

$$B \equiv Z \left[\ln \frac{2m_0 v^2}{I} - \ln \left(1 - \frac{v^2}{c^2} \right) - \frac{v^2}{c^2} \right]. \tag{3.4}$$

In this equation the properties of the heavy ion are the proton number z and the the velocity v, while the atomic properties of the absorbing medium are described by the number density N, the atomic number of the atoms Z, and the average excitation and ionization energy of the electrons I. e is the fundamental charge, m_0 is the electron mass, and c is the speed of light. The Bethe formula shows the energy loss of a heavy ion is proportional to z^2/v^2. Thus the energy loss can be effectively used to identify the element of the ion.

The stopping medium used in the S800 ionization chamber is P10 gas (90% argon and 10% methane). The chamber is divided into sixteen flat segments stacked parallel to one another and perpendicular to the beam axis. Averaging over the sixteen segments reduces the statistical fluctuation that would result from using only a single chamber. For elements with higher proton number, the relative difference in stopping power decreases, but the ionization chamber is capable of resolving elements up to $Z = 50$.

The sixteen pads of the ionization chamber each deliver a voltage signal which must be matched to one another. Every pad has its energy adjusted by a slope and offset parameter to match the value of a chosen reference pad. To perform the calibration, at least three different reaction products are selected. For each reaction product, the mean energy loss in each of the sixteen pads is found. One pad is chosen as the reference pad for each other pad to be matched to. Then, for each other pad, the mean energy loss values are matched to the mean energy loss of the chosen reference pad by a least squares fit method.

The energy loss in the ionization chamber is sensitive to the element of the ion but it also depends on the path length of the ion's trajectory as it moves through the chamber.

Since the ions in the spectrograph are bent in the dispersive x direction, the path length in the ionization chamber depends mostly on x_{fp}. This effect causes the energy loss for a particular element to lose resolution, hindering the particle identification. A correction for this is made by selecting one element and viewing the ionization chamber energy loss versus x_{fp} for all those ions. An example of the trend is shown in Fig. 3.7. The trend is fit with
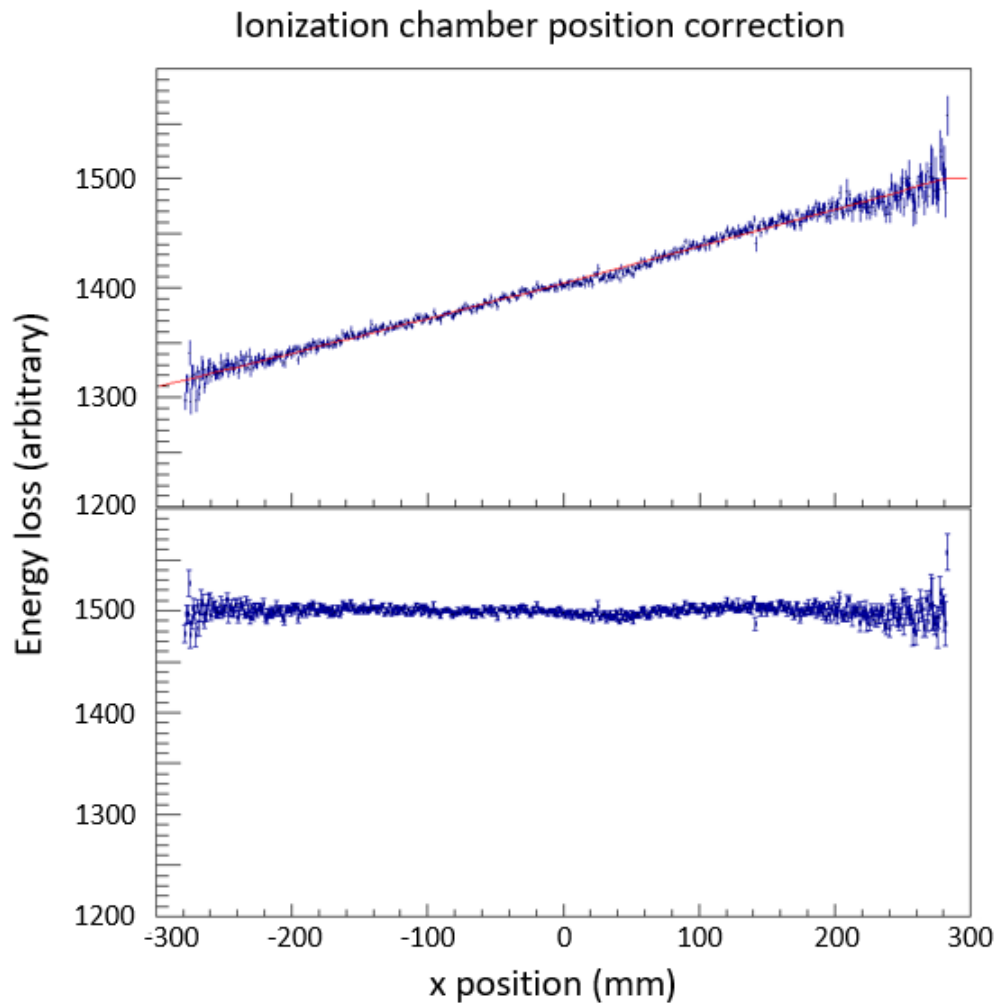
Figure 3.7: The top section shows the uncalibrated energy loss measured by the ionization chamber as a function of x_{fp}. A line is fit to the data and shown in red. The bottom section shows the ionization chamber energy loss calibrated for x_{fp}.

an exponential function

$$dE(x) = dE_0 e^{-p(x_0 - x)} \qquad (3.5)$$

where $dE(x)$ is the energy loss at a position x along the dispersive direction, and dE_0, p, and x_0 are parameters to be fit, with x_0 representing the reference x value, and dE_0 representing the energy loss at x_0. Then, the effect that x_{fp} has on the path length is corrected by applying the factor $e^{p(x_0-x)}$ to each event.

3.4.3   E1 Timing Scintillator

The E1 scintillator is a plastic scintillator at the S800 focal plane used to measure the time-of-flight (TOF) of the incoming nucleus. This is done by comparing the E1 scintillator time with the either the S800 object scintillator (OBJ), the A1900 extended focal place scintillator (XFP), or the timing provided by the cyclotron resonance frequency (RF).

The TOF is a critical component of identifying the nucleus in the S800. As the ion passes through the S800 dipoles it experiences uniform circular motion under the force caused by the magnetic fields. The uniform circular motion is described by

$$\frac{F}{m} = \frac{v^2}{r} \tag{3.6}$$

where the force causing the circular motion is

$$F = Bqv \tag{3.7}$$

and B is the strength of the magnetic field, q is the charge of the ion, v is the ion's velocity, m or A is the ion's mass, and r often denoted ρ is the radius of the circular motion. Then,

the mass to charge ratio can be related to the TOF t

$$\frac{A}{q} = \frac{B\rho}{v} = \frac{B\rho}{d}t \qquad (3.8)$$

where d is the distance traveled by the ion. In practice, the quantity $\frac{B\rho}{d}$ is fixed so $\frac{A}{q}$ is proportional to t. The E1 scintillator also serves as the trigger for readout for the S800. It can withstand a rate of up to 10^6 particles per second and has a timing resolution of 100 ps. The rate however is more constrained by the other focal plane detectors, for instance, the CRDC's which have a limit of about 5000 particles per second.

In this experiment, the TOF was determined using the E1 scintillator and the OBJ scintillator. A signal from the E1 scintillator was used as the start signal and the OBJ scintillator signal was used as a stop signal. The time difference between the two signals is digitized by three different devices in order to provide redundant backups of this important quantity. A Phillips 7186 time-to-digital converter (TDC), an ORTEC 566 time-to-analog converter (TAC), and a Mesytec 32-channel multi-hit TDC are available. The Phillips TDC malfunctioned during this experiment. The Mesytec multi-hit TDC was used in the data analysis due to its slightly better resolution than the ORTEC TAC.

The TOF is sensitive to the mass-to-charge ratio of ions, allowing the experimenter to differentiate between isotopes of the same element. However, the TOF also depends on both the x-position and the angle a that the ion trajectory makes in the x-direction. This is because, for instance, an ion with a large x_{fp} and a_{fp} will travel through the S800 spectrograph in a broader arc than an ion with a smaller x_{fp} and a_{fp}, causing it to take a longer time to reach the E1 scintillator. The x_{fp} and a_{fp} dependence hinders the good separation between different isotopes and should be corrected for. The correction is an adjustment

to the time-of-flight which is linear with both x_{fp} and a_{fp}. Figure 3.8 demonstrates how

the time-of-flight depends on x_{fp} and a_{fp} and how the correction reduces this dependence.

This correction to the TOF and the above corrections to the energy loss measured by the
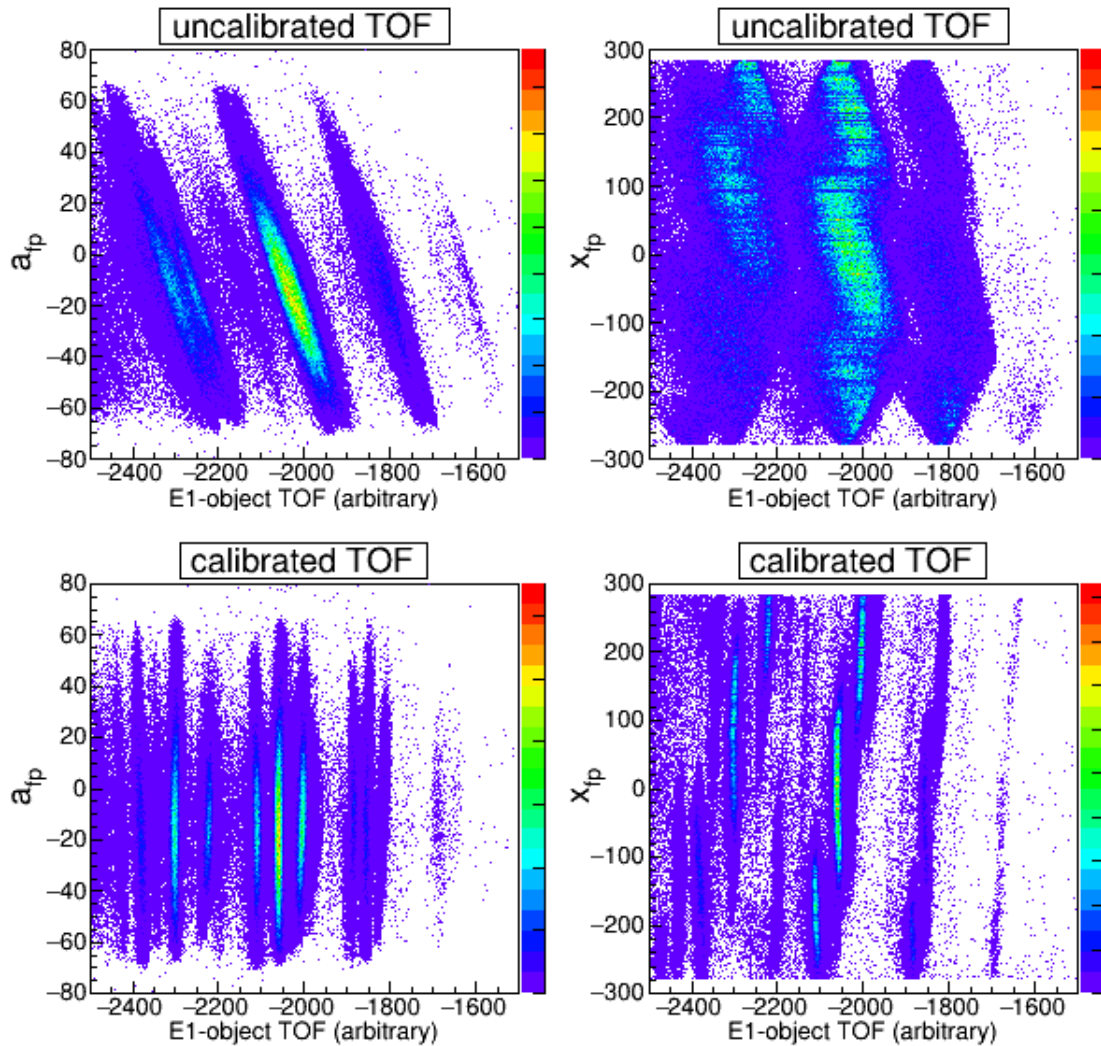
Figure 3.8: The uncalibrated time-of-flight (TOF) is shown with respect to a_{fp} and x_{fp}. The calibrated TOF is also shown, presenting a more uniform TOF distribution which allows for a more accurate particle identification with the S800 spectrograph.

ionization chamber were sufficient to identify the isotopes of interest in this experiment.

3.4.4 IsoTagger Hodoscope

Located at the end of the beam line is a CsI(Na) hodoscope called the IsoTagger. The IsoTagger consists of 32 sodium-doped cesium iodide crystals arranged into eight rows of four detectors as depicted in Fig. 3.9. The IsoTagger hodoscope can be used either to measure
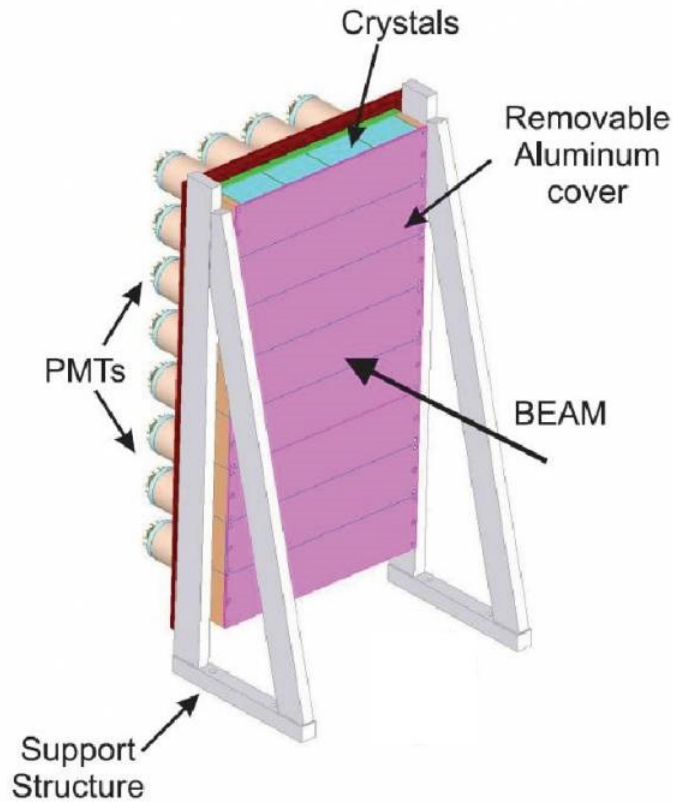
Figure 3.9: A diagram of the IsoTagger hodoscope. The 32 sodium-doped cesium iodide crystals are arranged into eight rows of four detectors each. The beam is stopped in an aluminum plate and gamma rays emitted from the decay of isomers are detected by the IsoTagger hodoscope.

the total kinetic energy of the ion to identify charge states, or to measure the energy of gamma rays emitted from isomers that survive to the end of the S800 focal plane. In the present experiment, the IsoTagger was used to identify isomers. In this setting an aluminum plate is placed in front of the IsoTagger causing ions to come to a stop just before the device. Gamma rays that are emitted following beta decay or the decay of an isomeric excited state

are observed by IsoTagger. The trigger from the E1 scintillator is directed to the IsoTagger to read out the signals when a reaction product reaches the focal plane.

The energy calibration for the IsoTagger can be accomplished using a known isomer among the reaction products. The reaction product ^{32}Al reaches the aluminum stopper in front of the IsoTagger and has a strongly-populated isomer with an excitation energy of 956.6 keV and a lifetime of 290(30) ns [75]. The decay of this isomer in the aluminum stopper will produce a cascade of two gamma rays with energies of 221.9(3) and 734.6(3) keV which are detected in IsoTagger. These known gamma-ray energies were used to calibrate the IsoTagger CsI(Na) detectors. Figure 3.10 shows the calibrated energy spectrum from IsoTagger gated on ^{32}Al reaction products detected at the focal plane. A timing gate is used to select events in the IsoTagger energy spectra that occur shortly after the trigger in the E1 scintillator. To use the IsoTagger to measure the lifetime of isomers, the total time for the ion to travel from the target to the focal plane in addition to the time for the readout trigger from the E1 scintillator to reach the IsoTagger must be determined. Since the isomer in ^{32}Al is already known, it was used to estimate the target reaction-to-IsoTagger readout time as 420 ns. While the IsoTagger hodoscope is effective at observing sufficiently long-lived isomers such as the isomer in ^{32}Al used in the calibration, it becomes less effective as the isomer lifetime becomes shorter ($\tau < 100$ ps).

3.4.5 Run-by-run Corrections

This experiment spanned about one week in time. Over such a time span, it may be necessary to consider changes to the calibrations of the S800 detectors over the course of the experiment. A single run of the experiment lasts one hour and the properties of the detector systems can change over the course of these runs. Hence run-by-run corrections to the detectors can
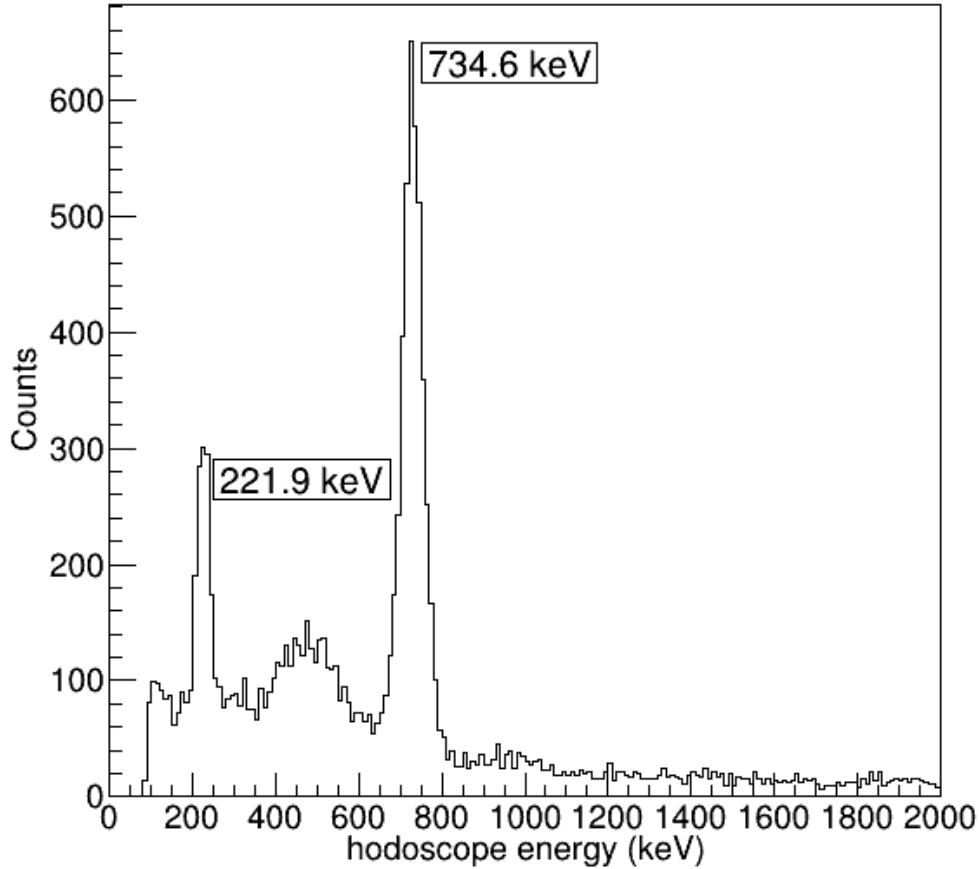
Figure 3.10: An IsoTagger spectrum gated on ^{32}Al ions at the focal plane of the S800 spectrograph. The gamma-ray transitions at 221.9 and 734.6 keV which follow the decay of the isomer at 956.6 keV are observed [75].

provide an important improvement of the experimental resolution.

The y-positions measured by the CRDC's comes from the drift time of the positive ionization charges, which in turn depends on the thermodynamic properties of the gas inside the CRDC's. The pressure and temperature of the gas in the CRDC's can change over the course of the experiment, resulting in the need for run-by-run corrections to the CRDC y calibration. Figure 3.11 shows the y_{fp} parameter for ^{32}Mg reaction products before and after run-by-run corrections were applied over all of the runs with the plunger setup. Without
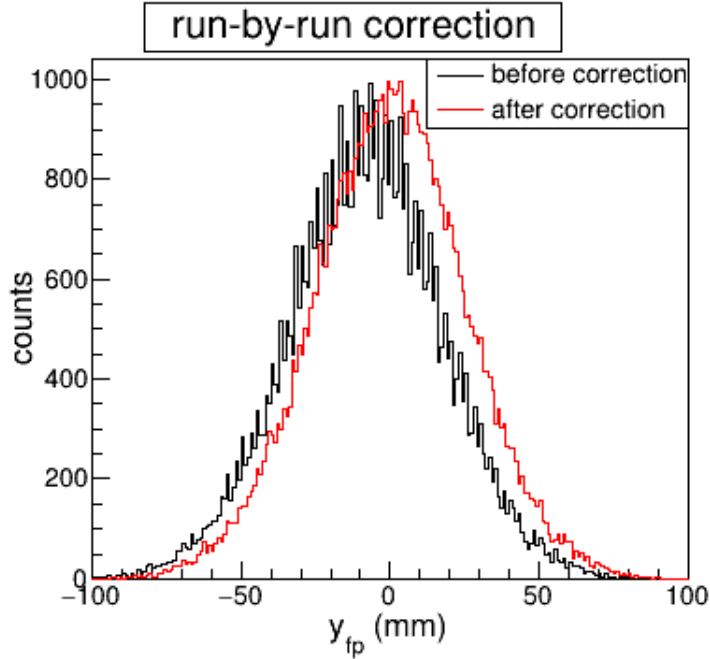
Figure 3.11: y_{fp} distributions, gated on ^{32}Mg reaction products. The distribution before run-by-run corrections is shown in black, while the distribution after run-by-run corrections is shown in red. The correction causes the distribution to be centered in the CRDC and slightly narrower.

the run-by-run corrections, the y_{fp} distribution for ^{32}Mg is centered slightly away from zero. The incoming beam was checked with a viewer at the beginning of the experiment and was observed to be centered on the nominal z-axis. The off-center y_{fp} can be caused by the changing characteristics of the CRDC gas over time and by shifts in the beam spot. To correct for this, the association between raw and calibrated y-values determined by the mask calibration above is adjusted. The offset value of the mask calibration is adjusted run-by-run to re-center the ^{32}Mg y_{fp} distribution. The final distribution is shown in Fig. 3.11 in red and is now centered and slightly narrower than the y_{fp} distribution before run-by-run corrections.

3.5 Gamma-Ray Energy Tracking In-beam Nuclear Array (GRETINA)

The Gamma-Ray Energy Tracking In-beam Nuclear Array (GRETINA) is an array of high-purity germanium gamma-ray detectors that combines high energy resolution, high position resolution, and large efficiency. At the time of this experiment, GRETINA consisted of ten cryostat modules,each of which house four high-purity germanium detectors. This section will describe the mechanical composition including the crystal shape and segmentation, and the technical properties including the methods for signal decomposition and gamma-ray tracking. While a full gamma-ray tracking algorithm was not implemented in the analysis, its discussion is included in this section for completeness. Following the description of the general characteristics of GRETINA, a description of the setup and calibration which are specific to this experiment are provided.

3.5.1 GRETINA Description

A single GRETINA module contains four individual high-purity germanium crystals as shown in Fig. 3.12 [66]. The crystals have a hexagonal face pointed to the center of GRETINA. The face is concave so that the center-facing edge of the crystal is equidistant from the center. Moving outward from the hexagonal face, the crystal smoothly becomes larger to compactly rest next to the adjacent crystals. In each module there are two crystals of type A and two of type B, with slightly different geometries. Each crystal is electrically segmented into 36 segments, as shown in the top-right part of Fig. 3.12. Each crystal also has a central core contact which reports the total energy from the entire crystal. The central signal provides the best energy resolution, while the signals from the segments provide more
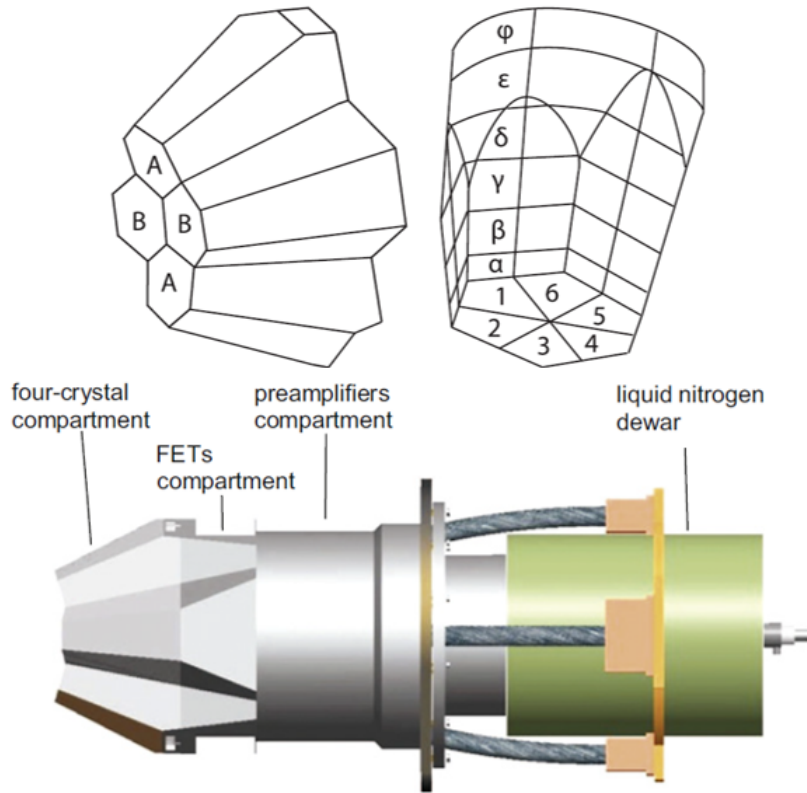
Figure 3.12: Diagram of a GRETINA module. The full module is shown in the bottom section. The four high-purity germanium crystals in a single module are depicted in the top-left. The segmentation of a single crystal is depicted in the top-right. The figure is adapted from Ref. [66].

position information [49]. Each segment signal is digitized and processed on a dedicated digitizer board at a rate of 100 MHz [76, 77]. Each of the modules are held in the same aluminum frame which is aligned in front of the the S800 spectrograph [49].

GRETINA incorporates technical advances in gamma-ray spectroscopy including signal decomposition and gamma-ray tracking. Signal decomposition refers to the practice of analyzing the digitized waveforms of the segment signals to determine sub-segment position information of the gamma-ray interaction [66]. A single incoming gamma ray can interact multiple times with the germanium crystal, including in the same segment. Therefore, one segment signal represent the superposition of multiple interactions with different positions

and energy deposits. The segment containing the gamma-ray interaction is sensitive to the energy, but the neighboring segment signals caused by image charges are critical for understanding the position of the interaction. The digitized waveforms from the segments are compared to a library of waveforms that correspond to gamma-ray interactions at various known points in the segment. In this way the observed waveform is decomposed into the components that best match the possible expected waveforms and contain the energy and position information of the one or several interactions in each segment Ultimately, the signal decomposition can achieve a position resolution of 2 mm.

After signal decomposition, the event can contain multiple interaction points including Compton scattering and photoelectric interactions, and can comprise the total energy of a real gamma ray, or the partial energy due to a backscatter event. It is the role of gamma-ray tracking algorithms to group together the interactions caused by a common gamma ray, put them in the correct order, and exclude interactions caused by other gamma rays. A typical gamma-ray tracking routine follows several steps to find the best arrangement of the interaction points according to a calculated figure-of-merit (FoM). First, several nearby interaction points are grouped together and assumed to be likely from the same gamma ray. Then, the most likely order of the interactions is found assuming the set of interactions involves a single photoelectric interaction preceded by one or several Compton scatter interactions. This is done by trying all possible orders of the interactions and using the measured energy and positions information to estimate how nearly it matches the expected values according to the Compton-scatter formula (Eq. 2.1). One possible representation of the FoM is

$$FoM = \sum \frac{(\cos \Theta^i_{en} - \cos \Theta^i_{vec})^2}{w_i} \tag{3.9}$$

where the sum is over all Compton-scatter interactions i, Θ_{en}^i is the scattering angle determined by the Compton-scatter formula and the measured energies, Θ_{vec}^i is the scattering angle according to the measured positions of the interactions, and w_i is a weight which is often chosen as the number of interactions [49]. The order of interactions that results at the smallest FoM is considered the most likely order. Gamma-ray tracking algorithms can then attempt ungrouping and regrouping the sets of gamma-ray interactions to try to achieve a smaller FoM.

For the present experiment, the signal decomposition approach described above was used for both online and offline data analysis. The gamma-ray tracking routine above, including the calculation of a FoM, was not implemented. Following the technique used in Ref. [49], the interaction point with the largest energy deposit was chosen as the first interaction point of one gamma ray. Then an add-back routine analogous to that used in Ref. [78] was implemented to sum energies within an $r = 80$ mm sphere centered on the first interaction point. Using the remaining interaction points, a second gamma ray was reconstructed with the first interaction point and add-back energy found in the same manner. In general, if interaction points still remain, the same add-back routine was repeated to define additional gamma rays.

3.5.2 GRETINA Calibration

The electric signal from GRETINA must be calibrated to relate it to a real gamma-ray energy. This is done by placing a radioactive source with a known decay information near the detectors. For this experiment, the energy calibration made use of a ^{152}Eu source. The calibration used in this experiment was made before the beginning of the experiment. To check the energy calibration, a ^{152}Eu source was placed at the TRIPLEX device target

position shortly before data was taken.

The methods used in this work rely on precise knowledge of the efficiency of GRETINA as well as the energy. For each circumstance where the efficiency of GRETINA must be understood, a radioactive ^{152}Eu source with a known activity was used. Figure 3.13 shows the measured efficiency of GRETINA at several energies corresponding to intense gamma radiations from the ^{152}Eu source. The efficiency of GRETINA is used when determining
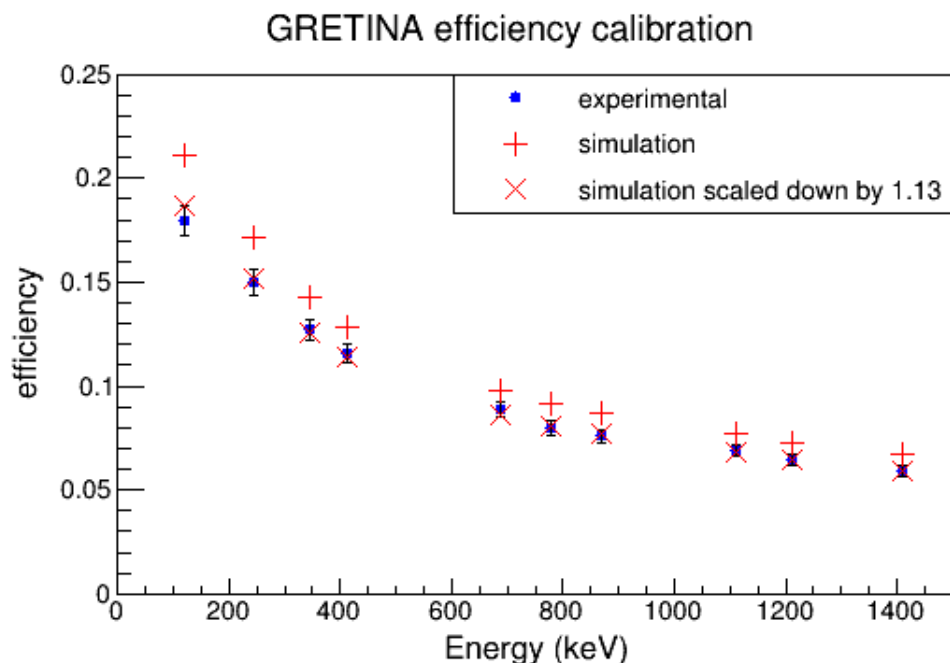
Figure 3.13: The efficiency of GRETINA measured using a ^{152}Eu radioactive source. For this measurement, the source was placed at the center of GRETINA. The efficiency of GRETINA in the GEANT4 simulation used in this work is also shown with red cross (+) symbols. The simulation efficiency is greater than the experimental efficiency by a factor of 1.13(2). The simulation efficiency scaled down by 1.13 is shown with red saltire (×) symbols and matches the data well.

the intensity of gamma-ray transitions from their observed peak area. The multiple foils used in the RDM measurement also play a role in the effective efficiency of GRETINA. The

attenuation of a gamma ray passing through a material is

$$\frac{I}{I_0} = e^{-\frac{\mu}{\rho}\lambda} \tag{3.10}$$

where I_0 is the initial gamma-ray intensity, I is the gamma-ray intensity after the material, ρ is the density, μ is the linear attenuation coefficient, λ is the areal density of the material. The areal density is related to the density and the length l over which the attenuation takes place by $\lambda = \rho l$. The quantity μ/ρ is also referred to as the mass attenuation coefficient. Tantalum has mass attenuation coefficient for 1 MeV gamma rays of $\mu/\rho = 0.06567$ cm^2/g [79]. Then for a 1 MeV gamma ray passing through 0.3 mm of tantalum, the remaining intensity is $I/I_0 = 0.968$. For lower-energy gamma rays, this attenuation plays an even greater role. For 0.1 MeV gamma rays, tantalum has a mass attenuation coefficient of $\mu/\rho = 4.302$ cm^2/g, which leads to significant attenuation, leaving only $I/I_0 = 0.116$ of the original gamma-ray intensity after the tantalum. To understand the effect that the gamma-ray attenuation by the TRIPLEX foils plays on gamma-ray efficiency, the ^{152}Eu source was placed on the face of each of the foils, one at a time, while efficiency calibration data was collected.

The RDM and CDM measurements both use a target located upstream of the center of GRETINA. In the CDM measurement, the gamma rays can be emitted all along the beam axis. Therefore it is necessary to understand how the efficiency of GRETINA changes for gamma rays emitted from various positions along the beam axis. Efficiency calibration data was taken with the ^{152}Eu source at several different positions along the beam axis upstream of the center of GRETINA. Figure 3.14 shows how the efficiency of GRETINA changes with the distance of the gamma-ray emission point from the center of GRETINA, and compares this with the same trend in the GEANT4 simulation package used in the analysis. The
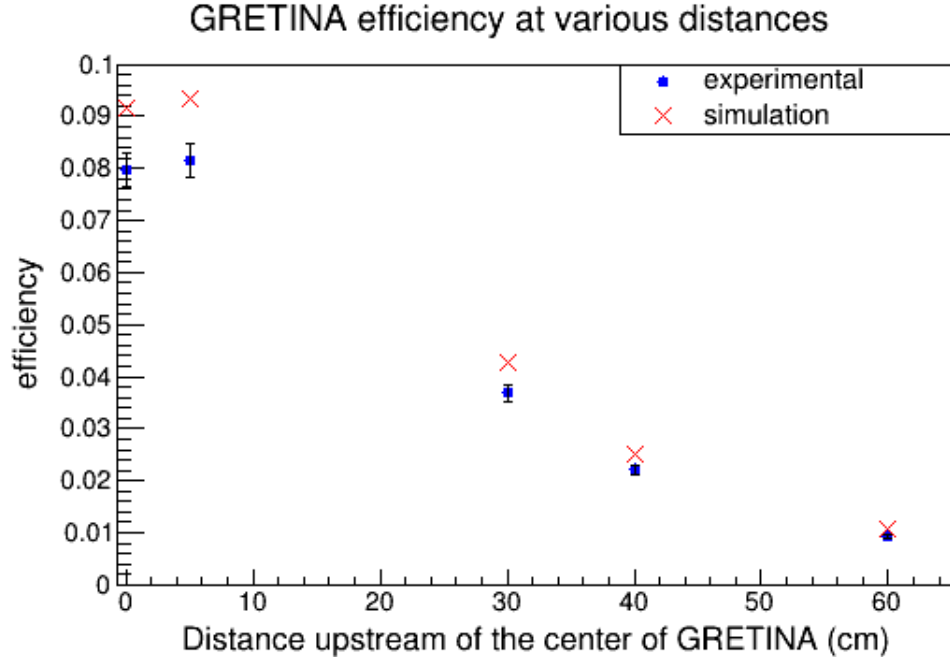
Figure 3.14: The efficiency of GRETINA for the 779-keV gamma ray from a ^{152}Eu radioactive source placed at various distances upstream of the center of GRETINA. The measured efficiency is shown with blue circles and error bars and the efficiency of GRETINA in the GEANT4 simulation is shown as red saltire ($\times$) symbols.

simulation follows the same trend as the data but with an efficiency that is 1.13(2) higher than the true efficiency at all points. This is consistent with the enhancement in efficiency in the simulation that is seen for all gamma-ray energies with a source at the GRETINA center as shown in Fig. 3.13.

3.6 TRIple PLunger for EXotic Beams (TRIPLEX)

The TRIple PLunger for EXotic Beams (TRIPLEX) device [80] is the dedicated plunger device at the NSCL for the in-flight measurement of short lifetimes in rare-isotope beam experiments. Plunger devices have been a valuable tool for lifetime measurements for many decades through RDM measurements [52, 81, 82]. The principle of a plunger device it to

hold a target foil and a degrader foil at a known distance so that nuclei recoiling from the target travel with a known flight time between the two foils which is near the lifetime of interest. Later, the Differential Recoil-distance Method [83] led to the design of plungers with a total of three foils [80, 84]. The TRIPLEX device was designed to hold up to three foils to allow the Recoil-distance Method and the Differential Recoil-distance Method [83]. In this section the details of the TRIPLEX device will be described, then the calibrations of the TRIPLEX device components will be explained.

3.6.1 TRIPLEX Description

The TRIPLEX device shown in Fig. 3.15 has three main components: the bearing unit, the foil system, and the support structure [80]. The bearing unit holds in place the immobile parts of the device, while allowing for smooth motion of the components associated with the moveable foils. This portion of the plunger consists of three concentric tubes and four sliding bearings that allow the inner and outer tubes to move relative to the middle tube. The middle tube is stationary and is the basis that all other stationary components are attached to. The motors are attached to the middle tube and are connected to the mobile inner and outer tubes by a small wire to drive these tubes with a minimum of force on the sliding bearings. Other stationary components including the connectors for the electrical components of the device, the micrometers, and the outer casing of the device which are attached to the middle tube.

In the foil system, each foil is attached to a circular mounting frame which in turn attaches to a ring on the appropriate tube of the bearing unit. The target connects to the inner-most tube, the first degrader to the middle tube, and the second degrader to the outer tube. The target and the first degrader foils are each a 5 cm × 5 cm square. Each foil is attached

65
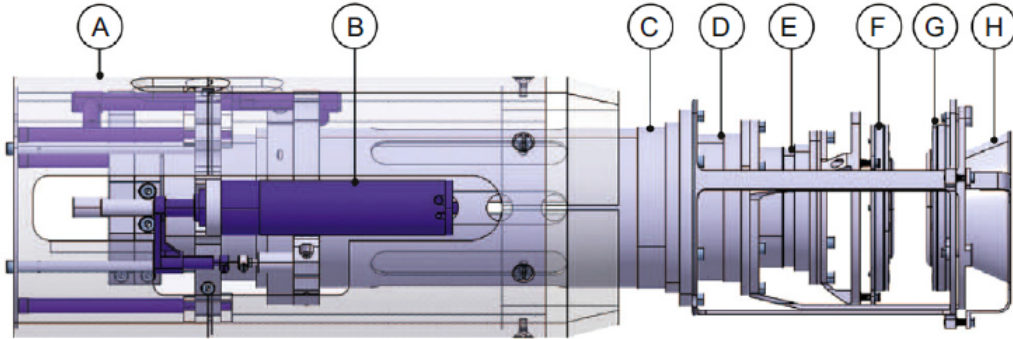
Figure 3.15: The TRIPLEX device used in this experiment. The schematic shows (A) the outer casing, (B) a piezoelectric motor, (C) the outermost tube, (D) the middle stationary tube, (E) the innermost tube, (F) the target positioned by the innermost tube E, (G) the first degrader held stationary by the middle tube, and (H) the second degrader positioned by the outermost tube. The figure is from Ref. [80].

to a conical mounting frame that then is connected to the ring of the appropriate cylinder by three screws. The target and first degrader frames and foils face one another and the separation between these two foils can be seen by eye. The second degrader foil is mounted on a frame that aligns concentric with the first degrader frame and can extend inside the first degrader frame. Though the first and second degrader foils can come into contact, the first degrader frame blocks any visual check of the separation between the first and second degrader at short distances. To accommodate the space within the first degrader frame, the second degrader foil is circular in shape with a diameter of 4.8 cm. Each frame is electrically isolated from the cylinder and the rest of the plunger structure to facilitate the voltage capacitance and feedback functionality of the device. The first degrader is held rigidly by

66

three screws. The target and second degrader have springs along the screws between the frames and the rings so that the springs are compressed as the screws are tightened. This arrangement holds the foils so that the target and second degrader can be smoothly adjusted to align with the rigid first degrader.

The support structure allows the TRIPLEX device to be positioned along the beamline and is specifically designed to be used alongside the S800 spectrograph and either SeGA (Segmented Germanium Array) or GRETINA. The main component of the support structure is the beam pipe which is wider than the standard GRETINA beam pipe to allow the TRIPLEX device to be positioned inside. The beam pipe attaches on its downstream end to an S800 magnet by a flange that allows for rough adjustments to the alignment of the beam pipe. Fine adjustments to the position of the TRIPLEX device are made within the beam pipe using a set of aligning screws that connect the device itself to the supporting beam pipe. The center of the foils can typically be aligned with the defined beam axis of S800 to within 1 mm. Electronic feedthroughs are located near the upstream end of the support beam pipe and are used to connect the electrical components of the plunger device to the control components outside the beam pipe while maintaining vacuum inside the beam pipe. When installed in the support system, the plunger target and degrader foils rest about 13 cm upstream of the center of GRETINA.

Several electrical components are used to set and measure the separation between the foils of the TRIPLEX device. The motors are N-381 NEXACT linear actuators made by Physik Instrumente (PI) [85] as shown in Fig. 3.16. The motors operate via linear actuators depicted in Fig. 3.17. The motors provide the force on the inner and outer tubes that move the target and second degrader foils relative to the first degrader foil. The motors also provide a displacement measurement that is accurate to within 1 μm. Another measurement
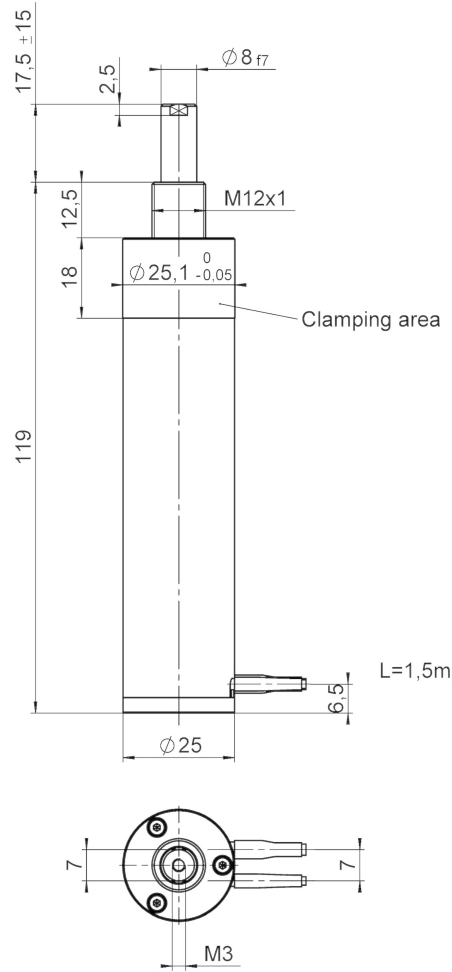
Figure 3.16: A schematic of a motor used to drive a tube and foil in the TRIPLEX device. The image is from Ref. [85].

of the displacement of each foil is made using a pair of micrometer GTL21 probes made by the TESA group [86]. These are attached to the immobile middle tube and are oriented to be compressed as the other two tubes move. The micrometers have a measurable range of about 2 cm and are accurate to within 1 μm, however accuracy degraders near the edge of their range. Nevertheless, when they are adjusted to the appropriate range, the micrometers are a valuable complementary measurement of the displacement measured by the motors.

A third method to measure the distance between two foils is to use the capacitance between the foils when a pulse is applied to the first degrader. This is possible since the

Figure 3.17: A cartoon depicting the operation of the linear actuators used within the motor of the TRIPLEX device. The image is from Ref. [85].

three foils are electrically isolated from one another. When a voltage pulse is applied to the first degrader, an induced signal can be measured from both the target and the second degrader. A pair of foils behaves approximately like a parallel-plate capacitor, where the capacitance is inversely proportional to the separation between the plates. Therefore, the induced signal is most sensitive to short separations between the two foils because in this range the signal size changes dramatically. The signal also gives a clear indication of when the two foils are touching because electrical contact between two foils will cause a sudden electrical short across the capacitor. ORTEC modules are used to manipulate these voltage signals. A pulser sends a pulse directly to the first degrader. An amplifier module and a linear gate and stretcher module are used to produce useful signals from each of the target and second degrader induced responses. A multi-channel analyzer (MCA) receives the induced responses and a trigger signal from the pulser after being sent through a gate and delay module.

To operate the motors and monitor the signals from the motors, the micrometers, and the induced pulser response, the Plunger Feedback Control software suite for Linux (PFCL)

is used [52]. The PFCL software was first developed to control the Cologne plunger [52] and contains tools that were not used in this experiment and will be omitted from this description. Three graphical user interfaces (GUI's) are provided by the PFCL software and are based on the LabVIEW programming language. The Motor GUI is used to control the motion of the motors and monitor the relative displacement of the motors as it moves. The Micrometer GUI provides a readout of the signal of the TESA micrometers. The MCA GUI is responsible for receiving the pulser trigger and induced response signals and reports the signal height of the response. All three of these programs are controlled by a PC located near the TRIPLEX device in the experimental hall and can be operated remotely while the experiment is running using a second PC. A diagram showing the connections among the PC, the GUI's, the electronic modules and the TRIPLEX components is shown in Fig. 3.18.

3.6.2   TRIPLEX Calibration

Using the TRIPLEX device and the associated hardware and software components, a precise understanding of the separation between the foils can be achieved. One simple check of the device is to compare the displacement reported by the motor with the displacement according to the micrometer when it is within range. Studying this correspondence shows that the motor and micrometer agree within 1 μm for both the target and the second degrader systems. Deviation does occur near the edge of the micrometer range of the micrometer since it loses precision at the limit of its range as mentioned earlier. Another deviation occurs when the motor and the foil change direction. In this case, the motor and micrometer can disagree by about 5 μm but come into sub-1 μm agreement again while the foil continues to be driven in the same direction.
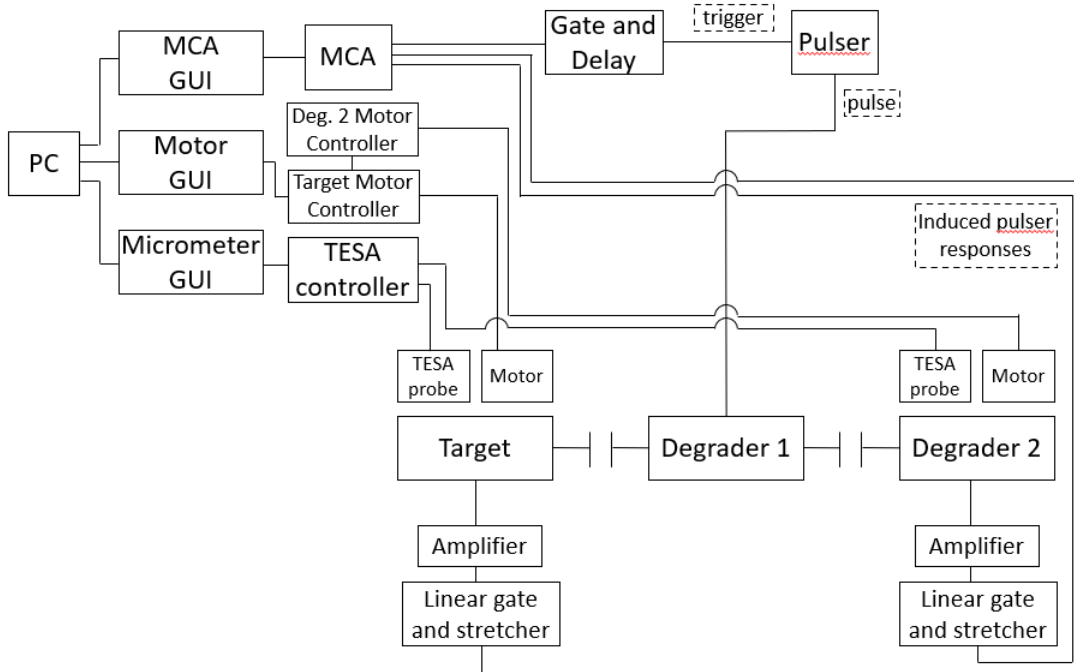
Figure 3.18: A diagram showing the connections between the TRIPLEX systems and the PC. The PC uses the multi-channel analyzer (MCA) GUI, the Motor GUI, and the Micrometer GUI to access the three systems represented here. The Pulser sends a trigger to the MCA and a pulse to Degrader 1 which causes induced pulse responses on Target and Degrader 2 due to the capacitance with these foils. NIM modules are used to manipulate the trigger signal and the induced pulse responses. A motor controller operates and reads the displacement value from each motor. The TESA controller reads the measurements from the TESA micrometers.

Much care is given to the alignment of the faces of the foils. This ensures that the ions experience the same separation between the foils, regardless of their x and y positions along the faces of the foils. For experiments involving small separations between the foils, the alignment becomes a large component in the uncertainty in the absolute separation between the foils.

The first foils to be aligned are the target and first degrader foils. The first degrader is held rigidly in place with screws attaching it to the plunger device, while the target can be adjusted by tightening or loosening its screws against the springs that hold the target steady. First, the alignment is roughly performed by eye when the foils have about $0.1 - 0.5$ mm of separation. Then the voltage response of the target is used to optimize the alignment

71

beyond what can be accomplished by eye. The induced voltage signal increases as the foils become closer, then saturates suddenly when they come into electrical contact. In practice, the target foil is aligned to the degrader to achieve the maximum possible induced voltage without the onset of electrical contact. The maximum induced voltage response signifies that the target and first degrader are as parallel as possible and with a minimum of separation. Any smaller voltage means that one of the edges of the target is misaligned further away from the first degrader.

At the maximum induced voltage response, we have a theoretical zero-distance separation between the two foils. This relies on a number of assumptions about the foils, including that they are perfectly flat parallel plates, that there is no non-conductive material on the foil faces causing them to touch without reaching electrical contact, and that the surface deformation of the foils is negligible. To test the error of this zero-separation position, the target is driven away from the first degrader and the height of the induced voltage signal is recorded over a number of different separations between the foils. Due to the properties of parallel plates, the inverse of the induced voltage is linear with the distance between the plates. We compare the nominal zero separation from the alignment with the parallel-plate capacitor trend extrapolated to where the separation becomes zero. The difference between these two zero-separation values is associated with our error in the separation between the foils. The difference depends on the quality of the foils but is typically be from tens of μm to 100 μm. To align all three foils, the target and first degrader are aligned first, then the first degrader is removed and the second degrader is aligned to the target, and finally the first degrader is replaced to its original position and the alignment between the first degrader and second degrader is checked for consistency.

The offset calibration of the TRIPLEX foils was performed before, during, and after the

experiment. Figure 3.19 shows the inverse induced voltage on the target at various nominal separations from the first degrader which was used in the offset calibration check while the TRIPLEX device was in the experimental beam pipe. The zero-separation offset values
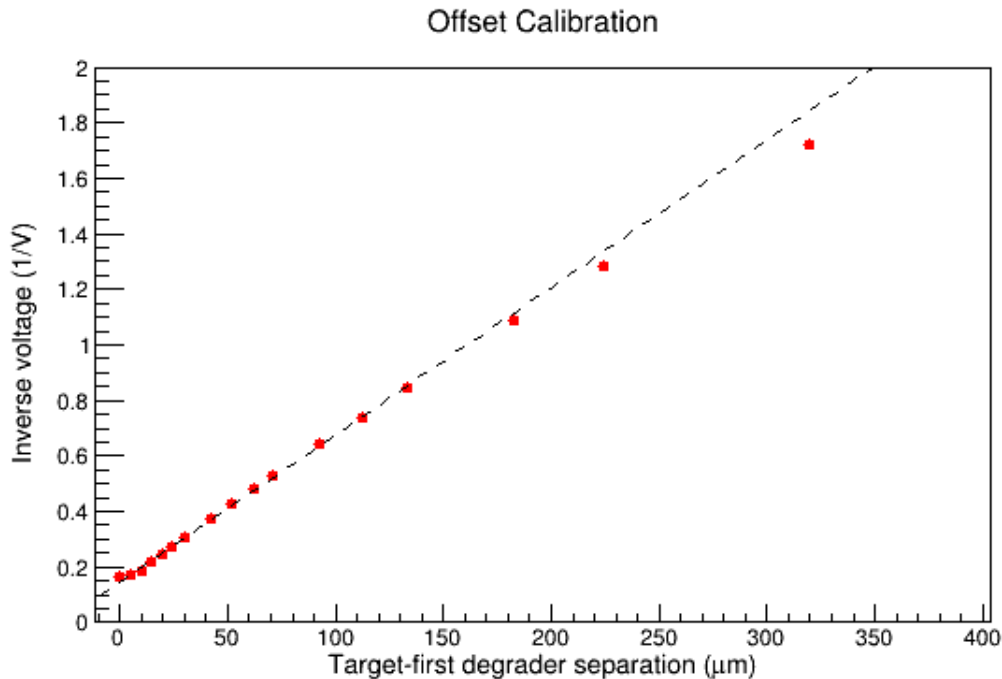
Figure 3.19: The inverse of the induced voltage on the target foil at various separations from the first degrader. The separation is measured relative to the location where the induced voltage saturated, indicating electric contact between the foils. The change in separation is measured by the motor displacement.

found throughout the experiment remained consistent for any pair of foils. The offset was 30 μm for the target-first degrader offset and 80 μm for the first degrader-second degrader offset. The offsets were used in the estimation of the uncertainty of the separation between two foils.

Another critical property of the TRIPLEX device is its absolute location relative to GRETINA and S800. The position of GRETINA relative to the S800 spectrograph is maintained across all S800-GRETINA experiments through the use of alignments rails and a mounting shell that holds the GRETINA modules in place. The position of the TRIPLEX

device is defined by the position of the first degrader relative to the center of GRETINA. For every TRIPLEX-GRETINA-S800 experiment, the same support system is used including the dedicated TRIPLEX beam pipe and flanges. The TRIPLEX device is inserted into the beam pipe using a push stick that has a known length, positioning the bearing system of the plunger at the same location in each experiment. The first degrader is occasionally installed with spacers placed on each screw to ensure that the target, first degrader, and second degrader can achieve the desired separation settings and the best range of the micrometers can be used. The length of the spacers in this experiment was 2.0 mm and caused a corresponding shift of the first degrader. Altogether, the upstream face of the first degrader is 12.9 cm upstream of the center of GRETINA. The value is consistent with previous TRIPLEX-GRETINA-S800 experiments that use a similar setup.

3.7   Experimental Setup to Study Short-lived States

As mentioned before, the TRIPLEX device was used only during the portion of this experiment designed to study lifetimes in the 1 ps to 100 ps range alongside GRETINA and the S800 spectrograph. For both portions of this experiment the primary beam was ^{48}Ca at 140 MeV/nucleon and the secondary beam was ^{34}Si. When the TRIPLEX device was in place, the energy of the ^{34}Si secondary beam was 60.0 MeV/nucleon with a rate of 8670 pps per pnA of primary beam and a purity of 67.4% at the focal plane of the A1900 fragment separator. The energy of the secondary beam in this portion of the experiment is lower than in the experimental setup designed to study long-lived states (86 MeV/nucleon) because a lower energy results in greater energy loss through the degraders. This increases the energy difference between the peak components in the RDM analysis and increases the sensitivity

of the peak shape in the DSAM analysis to short lifetimes. The momentum acceptance of the secondary beam was $\frac{\Delta p}{p} = 1\%$.

The target for this part of the experiment was a 52.9 mg/cm^2-thick ^{9}Be foil. The beryllium target in this part of the experiment is less thick than the target used in the experimental setup to study long-lived states in order to reduce the energy straggling here. The first and second degrader foils were made of tantalum and were 420 mg/cm^2 and 427 mg/cm^2 thick, respectively. Using tantalum for the degraders increases the energy loss as the reaction product passes through each degrader so that the energy difference between the target, first degrader and second degrader peak components is large enough to be clearly identified. The thicknesses of the foils were found by measuring the mass of each foil, then from the known dimensions of the foils and density of the material, the thicknesses were then calculated.

Placing three foils on the TRIPLEX device in a rare-isotope beam results in numerous parameters that must be constrained to arrive at useful lifetime results. The strategy to do this is to start with a simple target configuration, constrain a quantity, then move to progressively more complicated configurations. The settings discussed here are summarized in Table 3.1. The first and simplest setting has no foils installed. This setting is used to observe the ^{34}Si secondary beam itself with the S800 spectrograph, measuring it energy, position, and angular distributions. Then, the target is installed in the TRIPLEX device and the degraded energy of the ^{34}Si secondary beam is measured to understand the energy loss through the target foil. Data is also taken for the target-only setting with the S800 spectrograph tuned to accept the ^{32}Mg reaction product. This is used to constrain the population of excited states in the reaction of interest. The first and second degraders are then added one by one and the S800 spectrograph is tuned to the ^{34}Si unreacted beam to to understand the energy loss through each of the degrader foils as well.

Foils	S800 setting	T-1D separation	1D-2D separation	quantity of interest
none	^{34}Si	NA	NA	beam energy
T	^{34}Si	NA	NA	T thickness
T	^{32}Mg	NA	NA	gamma-ray intensity
T, 1D	^{34}Si	10.0 mm	NA	1D thickness
T, 1D, 2D	^{34}Si	10.0 mm	10.0 mm	2D thickness
T, 1D, 2D	^{34}Mg	25.0 mm	22.0 mm	reaction ratio
T, 1D, 2D	^{34}Mg	0.0 mm	0.5 mm	lifetime
T, 1D, 2D	^{34}Mg	0.0 mm	0.7 mm	lifetime
T, 1D, 2D	^{34}Mg	0.0 mm	1.0 mm	lifetime
T, 1D, 2D	^{34}Mg	0.0 mm	2.0 mm	lifetime

Table 3.1: The separations between the foils in the TRIPLEX device. T refers to the target, 1D refers to the first degrader, and 2D refers to the second degrader. The S800 setting refers to whether the S800 spectrograph was tuned to the unreacted ^{34}Si secondary beam or the ^{32}Mg reaction product.

Data was also collected with the foils placed at large separation so that the reaction population of states in ^{32}Mg could be understood. For this so-called large-separation setting, the target-first degrader separation was 25 mm and the first degrader-second degrader separation was 22 mm. With the large separations, the excited states in ^{32}Mg that are populated in reactions occurring on the target all decay to the ground state before the first degrader is reached. Then, the first-degrader component is due only to reactions on the first degrader and has no contribution from reactions on the target that survive long enough to decay after the first degrader. Similarly, the second degrader component is due only to reactions on the second degrader, not on the target or the first degrader. Thus, from the large distance setting it is possible to quantify the relative reaction rate for the three foils. This is a critical piece of information when analyzing the lifetime with the short distance settings. In the short distance settings the peak components are due to reactions on the corresponding foil as well as reactions on an upstream foil that decay past the relevant foil. Having quantified the reaction ratio from the large distance setting, the peak components

can be fully understood and a sensitive lifetime can be extracted.

Finally, the settings with short separation between the foils can be used to determine the lifetimes. One priority of this experiment was to measure the lifetime of the 2_1^+ state of ^{32}Mg which has been determined from past Coulomb-excitation experiments to have a lifetime of $\tau = 16(3)$ ps [87]. To be sensitive to this lifetime range, the second degrader was positioned with a separation of 0.5 mm, 0.7 mm, 1.0 mm, and 2.0 mm from the first degrader corresponding to approximate travel times of the nucleus between these two degraders of 5 to 20 ps. The lifetime of the 4_1^+ state is another property of interest and has not been measured in the past. The lifetime of the 4_1^+ state was estimated to be near 1 ps and so the separation between the target and first degrader was made to be as small as possible, nominally 0.0 mm. As the separation between the first degrader and second degrader was changed among the four settings above, the target and first degrader separation was left at 0.0 mm to accumulate as much data as possible at the smallest separation possible. This setup takes advantage of the capabilities of the TRIPLEX device to simultaneously measure lifetimes near 1 ps and 16 ps by setting each of the degraders at a sensitive separation.

During the experiment, a plastic 7 mg/cm^2 polyethylene foil was added to the TRIPLEX device to reduce the amount of different charge states seen by S800. The plastic foil was attached to the downstream edge of the frame holding the second degrader foil. There was 2.2 cm of separation between the second degrader and the plastic foil. Different charge states of the reaction products are created when the fully stripped ion gains one or several electrons while passing through the target and degrader foils. The various charge states have different mass-charge ratios which causes a portion the desired ^{32}Mg reaction products to fail to reach the focal plane of the S800 spectrograph and remain undetected. The charge states can also lead to unwanted contamination in the particle-identification spectrum or can cause large

numbers of unwanted reaction products to overwhelm the the CRDC's which are limited to a rate of 5000 Hz. The plastic foil is effective at stripping the electrons from ions, returning them to a fully-stripped state. The additional energy loss caused by the plastic foil was required the S800 spectrograph to be retuned in order to center the ^{32}Mg reaction products at the focal plane.

3.8 Experimental Setup to Study Isomeric States

An alternative approach was necessary to observe decays from states such as the 0_2^+ state of ^{32}Mg which was observed only once previously with an estimated lifetime of $\tau > 10$ ns [13]. The TRIPLEX device is not useful to observe this state since most decays will occur past the second degrader, over a range on the order of 1 m at the relativistic beam velocities of this experiment. It was necessary to use the Cascade Doppler-shift Method (CDM) discussed in Section 2.2.3 in order to observe the Doppler-corrected energy of gamma rays emitted from this state.

This portion of the experiment was also performed using a ^{34}Si secondary beam but at an energy 86 MeV/nucleon. The resultant beam had an intensity of 9×10^5 pps and a purity of 82%. The 0_2^+ state of ^{32}Mg was populated in the ^{9}Be(^{34}Si, ^{32}Mg)X reaction on a 0.57 g/cm^2-thick ^{9}Be target using the setup shown in Fig. 3.20. To validate our method, we examined the ^{31}Mg products created simultaneously from the same setup which populates a $(7/2^-)$ isomer at 461 keV with a lifetime of $\tau = 15.1(12)$ ns [88]. Reaction products were identified by TOF and energy-loss measurements from the S800 spectrograph [65].

Various alterations were made to the experimental setup to prioritize the application of the CDM measurement of the 0_2^+ state of ^{32}Mg. Instead of using the TRIPLEX device, a
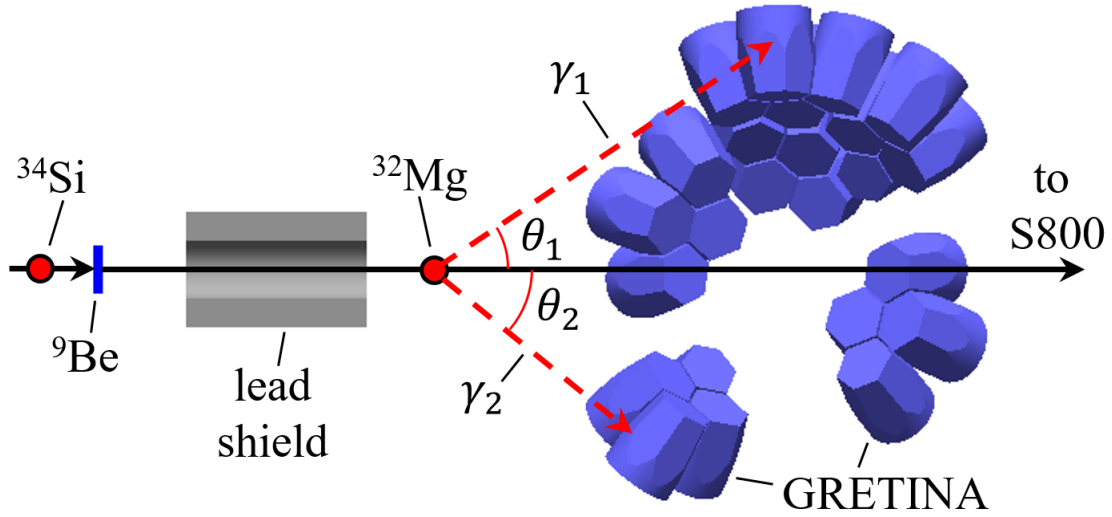
Figure 3.20: The setup for the part of the experiment with the upstream target, designed to measure the 0_2^+ isomer of ^{32}Mg. The ^{9}Be(^{34}Si,^{32}Mg)X reaction populates the 0_2^+ isomer which emits a cascade of gamma rays γ_1 and γ_2 at angles θ_1 and θ_2 relative to the ion trajectory.

single Be target foil was used with a thickness of 0.57 g/cm^2. Though a thicker target foil increases the energy straggling of the products more than a thin one, this was offset by the lack of degrader foils. With a thicker target, the yield of the product was directly increased.

In order for GRETINA to be as efficient to decays from the 0_2^+ state as possible, the target was placed 72 cm upstream. This brought more of the decays occurring over a range of about 1 m closer to the center of GRETINA where the array has higher efficiency. A specialized beam pipe was constructed to hold the target at this upstream location while allowing space for GRETINA to close around the target and beam pipe. Due to the angular spread of the reaction products, one concern is that reaction products of interest might not be accepted by the angular coverage of S800. By placing the target further upstream, this problem can be exacerbated because the products will spread further from the center of the beam axis before they reach S800. In this experiment, the angular acceptance of S800 was 90(2)% for products created at the upstream target.

The background produced near the target position was attenuated by placing a hollow cylindrical lead shield around the target. This shield was 19.05(5) cm long and 6.03(5) cm in radius with a hollow bore through the center with a radius of 3.02(5) cm, allowing the reaction products to pass through the center. The shield was held in place by a collar that attached to the support shell of GRETINA and closed around the beam pipe. The target was about 8 cm upstream of the upstream edge of the shield. In this arrangement, the shield covered the full angular range of gamma rays emitted from the target that could otherwise be detected by GRETINA.

The standard GRETINA setup at the time of this experiment had four detectors at forward angles and the remaining six positioned at 90 degrees to the center of GRETINA in order to have the greatest efficiency and resolution to gamma rays emitted from the center of GRETINA. However in this experiment, the decays occur along the beamline for a considerable distance and sensitivity to the lifetime depends on observing decays of the 0_2^+ state at various points along the 1 m range. To accomplish this, GRETINA was arranged to have four detectors at backwards angles, two at 90 degrees, and four at forward angles relative to the beam axis measured from the center of GRETINA. This arrangement was also used during the TRIPLEX device portion of the experiment.

3.9   Data Analysis Tools

The data analysis in nuclear structure experiments typically requires the handling of large amounts of data. This subsection will introduce the main software suites that are used to sort the data into structures that are useful for the experimenter, and simulation tools that probe the details of the quantities of interest.

3.9.1 SpecTcl Online Data Analysis

During the experiment, the data is quickly analyzed to provide the experimenters with timely information so that they can make informed decisions about the next steps of the experiment. The main tool for this purpose is SpecTcl [89]. SpecTcl is a data analysis tool used for many experiments at the NSCL. SpecTcl is based on a C++ framework and allows the fast processing of data streams from several sources into customizable graphical user interfaces such as histograms.

3.9.2 GrROOT and ROOT Offline Data Analysis

The analysis of data after the experiment is an iterative process using the GrROOT package based on the CERN ROOT toolkit [90]. GrROOT was developed to unpack data from experiments using S800 and GRETINA. The original code can be modified to accommodate additional data streams or alternative analysis methods, such as the CDM method used in this experiment. GrROOT sorts the data in three individual steps: first the raw data is unpacked from its hexadecimal form into ROOT trees of decimal values, then the raw data is calibrated, and finally the ROOT trees are sorted into histograms. The calibration and histogram-building steps are often repeated several times as additional calibrations and corrections are applied to the data stream as they become understood by the experimenter. In fact, most of the device calibration steps described in the sections above were carried out using GrROOT. GrROOT allows the user to make two-dimensional graphical cuts to select events corresponding to the incoming beam and outgoing reaction product of interest.

3.9.3 G4Lifetime Simulation

The data from the experiment can be compared to simulated properties as a systematic probe of the true physics values. G4Lifetime is a simulation program based on GEANT4 [91], a package effective at simulating the interaction of particles with matter, that has been developed to extract lifetime results from TRIPLEX experiments [92]. All relevant properties of the experiment can be handled within G4Lifetime including the incoming beam properties, the TRIPLEX foil setup, the reaction process, the emission of decay particles and gamma rays, and the detection of these radiations. G4Lifetime was also modified to allow for the upstream experimental setup and the CDM measurement used to observe the 0_2^+ state.

There are many aspects of G4Lifetime that must be constrained by physical measurements to consistently reproduce a final lifetime result. The experiment and simulation are designed so that the only free parameter in the simulation is the final lifetime result, and every other physical property is measured.

The first G4Lifetime parameters to be constrained are the incoming beam parameters. These are experimentally determined with the setting with no foils installed in the beamline. A comparison between the experimentally measured and the simulated incoming beam properties are shown in Fig. 3.21. Using the CRDC's of the S800 spectrograph the ion profile distribution is known at the target position in terms of y_{ta}, a_{ta}, b_{ta}, and d_{ta}. The simulated distribution of the incoming beam position, trajectory, and kinetic energy are all Gaussian distributions where the centroid and width can be adjusted to fit the observed distribution.

The target and degrader foils are implemented in the foil next, one by one. Each foil is reproduced in the simulation by providing the thickness based on the mass measurement. The default energy loss through the foils in the simulation does not perfectly reproduce the
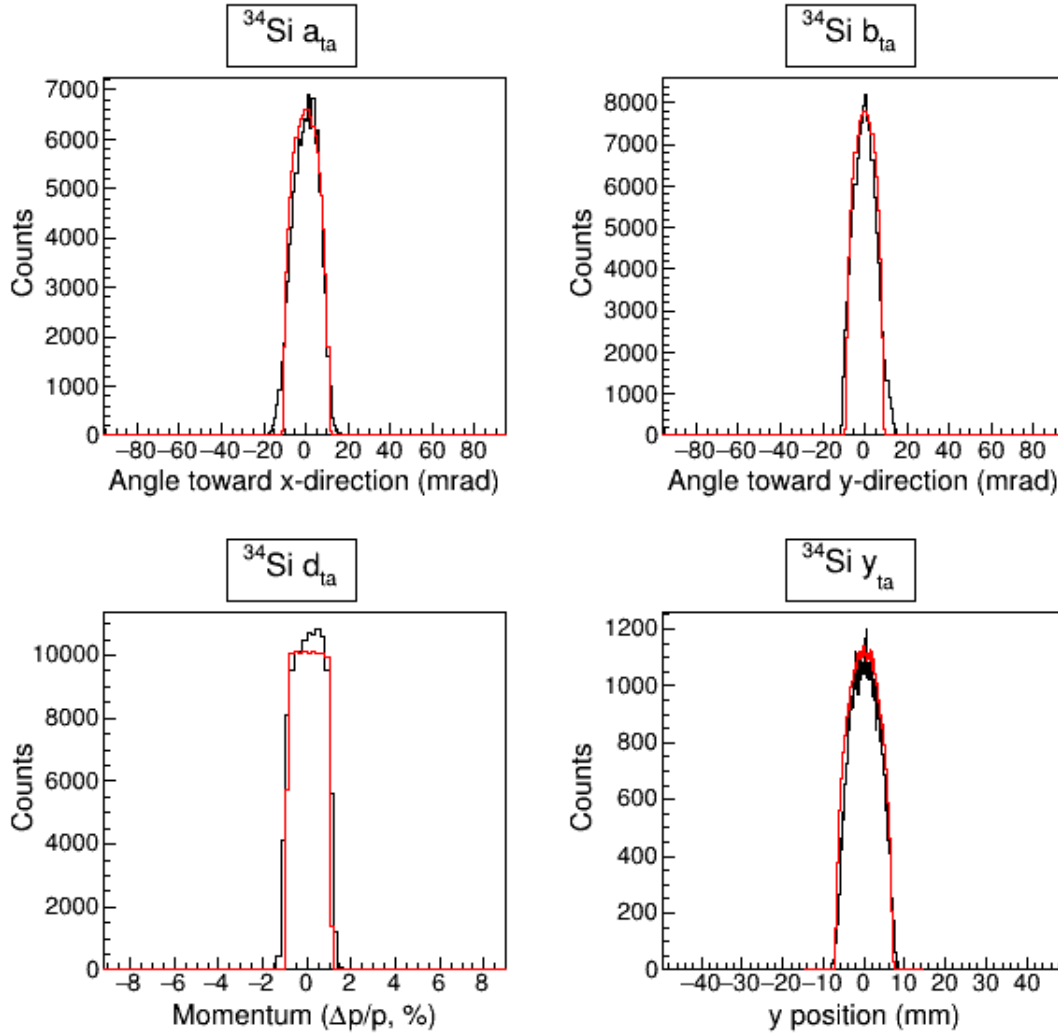
Figure 3.21: The a_{ta}, b_{ta}, d_{ta} and y_{ta} distributions of the ^{34}Si secondary beam. Data is shown as a black line and a scaled simulation is shown as a red line.

the experimental energy loss through the foils. The experimental energy loss through each foil was measured by adding the foils one at a time and measuring the reduced energy of the unreacted ^{34}Si beam with the S800 spectrograph. A correction to the energy loss of the foils in the simulation is made by scaling the density of the foil to match the observed energy loss. In this experiment the scale density factors are 0.990, 0.983, and 0.992 for the target, first degrader, and second degrader foils of the TRIPLEX device respectively, and 1.000 for the target in the upstream configuration.

The nuclear reaction that results in the ^{32}Mg product causes a change in the momentum of the ion based on the reaction kinematics involved. A comparison between the simulated and the experimentally observed ion profile distribution is shown in Fig. 3.22. In the simulation
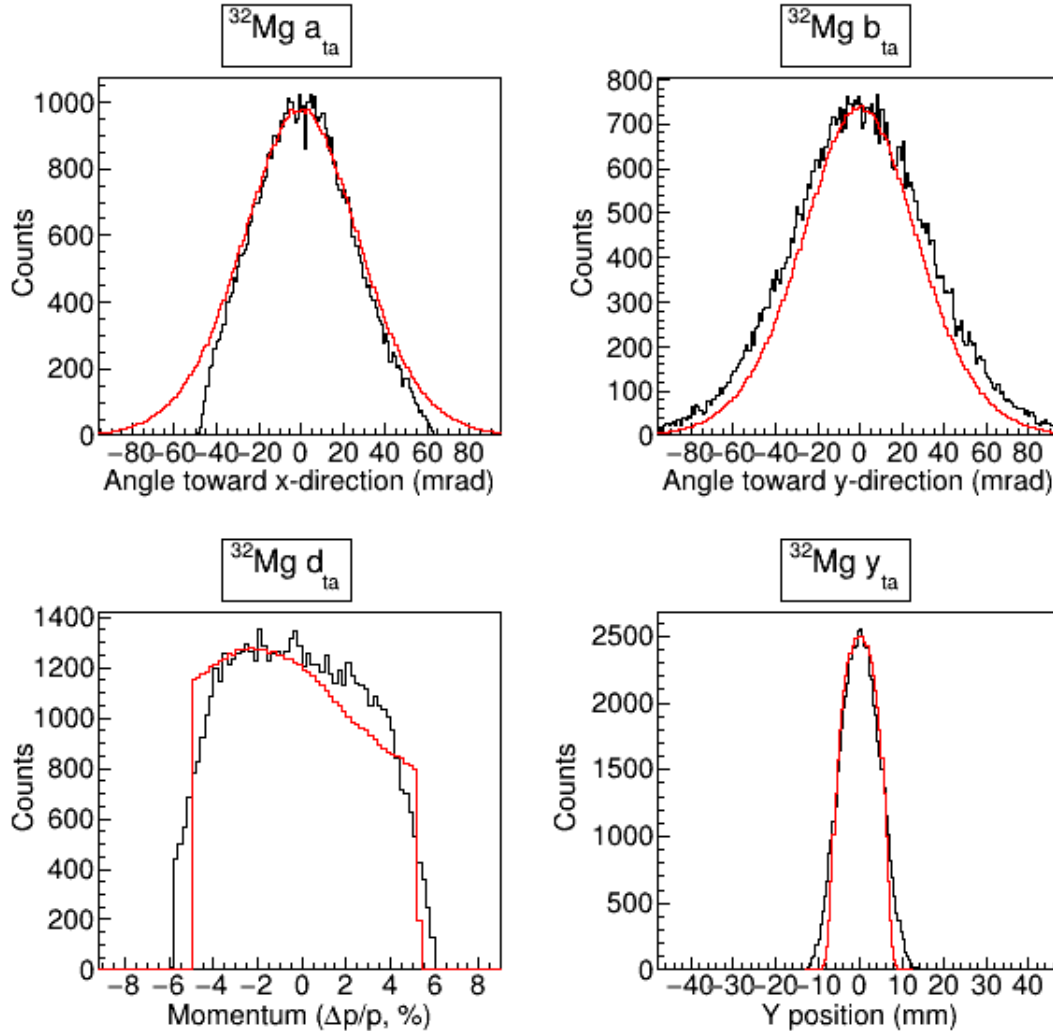
Figure 3.22: The a_{ta}, b_{ta}, d_{ta} and y_{ta} distributions of the ^{32}Mg reaction product with all three foils installed in the TRIPLEX device. Data is shown as a black line and a scaled simulation is shown as a red line.

each reaction event has its momentum scaled by the change in mass and by a parameter called dp_frac. Then the width of the outgoing momentum is adjusted by adding a vector ΔP to the outgoing momentum. The direction of ΔP is chosen at random. The magnitude

of ΔP is also random, but chosen from a Gaussian distribution centered about the parameter `dp` with width controlled by the parameter `dpFWHM`. In practice, the centroid of the kinetic energy distribution d_{ta} is sensitive to the `dp_frac` parameter. The widths and tails of the d_{ta}, a_{ta}, b_{ta}, and y_{ta} distributions of the reaction product are controlled by the `dp` and `dpFWHM` parameters which are varied to match the observed distributions. The G4Lifetime simulation can also control the edges of the reaction product distributions to match the acceptance of S800. This effect can be seen as the sharp cutoff in the d_{ta} distribution of Fig. 3.22.

The excited state properties of the product nuclei are specified by listing each state, excitation energy, gamma-ray transition energy, lifetime, and the fraction of reactions that populate that state. When the reaction product is produced, the ion will continue to travel along its trajectory and emit Doppler-shifted gamma rays with a random direction according to the specified lifetime and energy of the excited states.

The gamma-ray efficiency in the simulation was compared to that observed with calibration sources before and after the experiment. A comparison is shown in Fig. 3.13. The simulated efficiency is systematically greater than the measured efficiency across all gamma-ray energies by a factor of 1.13(2). This is believed to be caused by the fact that in the simulation not all of the material between the ion and the GRETINA crystals is included. This includes materials such as portions of the beam pipe, the TRIPLEX device, and the housing for the GRETINA crystals. As a result, gamma rays are not attenuated in the simulation as much as they are in reality. To correct for the difference in efficiency, the gamma-ray yield in the simulation is simply scaled down by the enhancement factor. Since for part of the experiment the target is 72 cm upstream, it was important to see how the efficiency of GRETINA changes along the beam axis. Figure 3.14 shows that the efficiency enhancement in the simulation remains consistent for gamma rays emitted from various distances from

the center of GRETINA.

G4Lifetime generates simulated gamma rays according to the provided excited state parameters. One must determine the relative population of each of these excited states by fitting the sum of the gamma-ray responses for each populated state plus an exponential background to the data taken during the target-only setting. This is accomplished with the target-only setting of the TRIPLEX experimental setup. The number of counts in each gamma-ray energy peak can be more easily quantified with only the target in place than with multiple foils installed in the TRIPLEX device. The results of this portion of the G4Lifetime setup for the reaction products analyzed in this work are provided in Chapter 4.

Turning to the three-foil settings, the gamma-ray spectra become complicated by the fact that each peak now has three components, each corresponding to decays occurring just past each of the three foils. The relative height of these components contains information on the lifetime for reactions in the target, but they also have contributions due to reactions on each of the degraders. The relative number of reactions on each of the three foils is quantified with the large-separation setting. In the large separation setting, the only contribution to each component is due to reactions on the corresponding foil since the lifetimes of the excited states are much shorter than the time it takes a nucleus to travel between the foils.

With the simulation prepared according to the above steps, the only unknown quantity is the lifetime of the excited states. These lifetimes are determined following a chi-squared analysis. A lifetime is assumed in the simulation, and the resulting gamma-ray energy spectrum is fit to the experimental data and a chi-squared value is calculated. In the fitting procedure, the simulation has an exponential background added to it. The background is fit to the experimental data at energy regions far from the gamma-ray peaks. Then, the only free parameter to fit the simulation is the scale of the simulated response. In cases with low

statistics, the number of counts in the bins of the experimental gamma-ray energy spectrum can be quite small (< 20 counts). This requires the use of a Poisson chi-squared statistic [93]

$$\chi^2 = 2 \sum_i y_i - x_i + x_i \log \frac{x_i}{y_i} \tag{3.11}$$

instead of the more common Gaussian chi-squared statistic

$$\chi^2 = \sum_i \frac{(x_i - y_i)^2}{x_i} \tag{3.12}$$

where x_i is the number of observed counts in a bin and y_i is the predicted response. For bins with large counts the Gaussian chi-squared statistic is approximately the same as the Poisson chi-squared statistic and the 1σ uncertainty in the number of counts N in a bin is approximately $\sqrt{N}$. For bins with few counts, the $\sqrt{N}$ approximation does not hold and the uncertainty in the observed number of counts becomes asymmetric with greater uncertainty in the positive direction than the negative direction. This can be seen in the low-statistics spectra shown in the next chapter where the error bars for bins with few counts have slightly larger positive error than negative error.

Chapter 4

Data Analysis and Results

The lifetimes that were studied in ^{32}Mg have very different time scales and required different experimental techniques. The yrast 2_1^+ and 4_1^+ states have short lifetimes of roughly 16 ps and 1 ps respectively. These are best measured with the TRIPLEX device setup which can cover both lifetime ranges simultaneously. The results of this experimental setting will be discussed first and will include lifetime results for the 2_1^+ and 4_1^+ states of ^{32}Mg. Also presented are the results of the analysis of byproduct data which yield the lifetime results of the 2_1^+ state in ^{30}Mg and the 2_1^+ state in ^{20}O. The ^{30}Mg and ^{20}O results are valuable to confirm the techniques against previously measured data sets.

Another goal of this research is to confirm the once-measured 0_2^+ state of ^{32}Mg [13] and constrain its lifetime. The isomeric 0_2^+ state of ^{32}Mg has a long lifetime that cannot feasibly be measured with the same RDM method used to study the 2_1^+ and 4_1^+ states and instead requires the CDM method. The energy and lifetime results for the 0_2^+ state are reported later in this chapter. The exclusive cross section that populates the 0_2^+ state in the ^{9}Be(^{34}Si, ^{32}Mg)X reaction is also discussed. Additional byproduct data regarding the $(7/2^-)$ state of ^{31}Mg is presented, confirming the CDM analysis with a known physics case.

4.1 ^{32}Mg Short-lived States

The diminished excitation energy of the 2^+_1 state in ^{32}Mg was one of the first evidences that the ^{32}Mg nuclide belonged in the $N = 20$ island of inversion [14]. The several past measurements of the $B(E2 : 0^+_1 \to 2^+_1)$ value agree with the picture of a collective yrast band [12, 35–39], although the results have varied considerably. The ratio $B(E2; 4^+ \to 2^+)/B(E2; 2^+ \to 0^+)$ remains undetermined since the $B(E2; 4^+_1 \to 2^+_1)$ has never been reported. To improve our understanding of collectivity in the ground-state band of ^{32}Mg it is the goal here to resolve the variation among the previous $B(E2; 0^+_1 \to 2^+_1)$ results and provide the first determination of the $B(E2; 4^+_1 \to 2^+_1)$ value.

A portion of this experiment was designed to measure the lifetimes of the 2^+_1 and 4^+_1 states in ^{32}Mg. The previous measurements of the $B(E2 : 0^+_1 \to 2^+_1)$ value have led to an estimate of the 2^+_1 lifetime as $\tau(2^+_1) = 16(3)$ ps [87]. A RDM measurement is appropriate to study this lifetime range. For ion velocities of $v = 0.3c$, the 2^+_1 state will travel about $d = 1.6$ mm in one lifetime so it is appropriate to place a degrader roughly 1 mm away from the target. Meanwhile, the 4^+_1 state may have a lifetime in a very different range, roughly $\tau(4^+_1) = 1.0$ ps. To study the lifetime near 1 ps with the TRIPLEX device a degrader is placed directly after the target with zero separation. A RDM measurement of the 2^+_1 lifetime is still simultaneously possible with a sufficiently thin degrader. In fact, the first degrader can act as an additional target for the measurement of the 2^+_1 lifetime. Thus, the TRIPLEX device allows for the simultaneous measurement of the rather different lifetimes near 16 ps and 1 ps estimated for the 2^+_1 and the 4^+_1 states, respectively.

The secondary beam of ^{34}Si was identified using the correlation between two time-of-flight (TOF) values shown in Fig. 4.1. Along with ^{34}Si, there was significant contamination
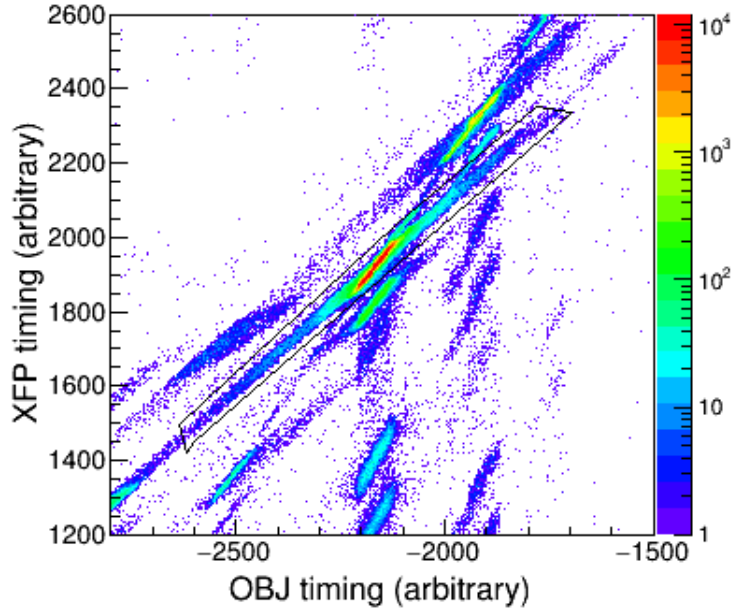
Figure 4.1: The particle identification (PID) for the ^{34}Si secondary beam. The x-axis is the TOF in arbitrary units between the E1 and OBJ scintillators of the S800 spectrograph. The y-axis is the TOF in arbitrary units between the E1 scintillator of the S800 and the XFP scintillator of the A1900 fragment separator. Both time values were digitized with the Mesytec multi-hit TDC. The software gate used to select ^{34}Si ions is shown as a solid black line.

from ^{35}P in the secondary beam. The desired secondary beam component was selected by applying a software gate to the TOF-TOF correlation plot. The ^{34}Si secondary beam was observed in the focal plane of the S800 spectrograph during the setting with no foils installed in the TRIPLEX device. The position, momentum, and angular distributions of the ^{34}Si secondary beam are shown in Fig. 3.21.

4.1.1 ^{32}Mg Target-only Setting

The target-only setting provides the simplest view of gamma-ray energies from the decay of ^{32}Mg excited states in this experiment. This setting includes only the ^{9}Be target in the TRIPLEX device. The purpose of the target-only settings is to observe the states that

are populated in this particular reaction. The energy and intensity of each gamma ray is measured in this setting.

The particle identification (PID) spectrum for ^{34}Si reaction products in the target-only setting is shown in Fig. 4.2. A software gate is placed on each of the reaction products using
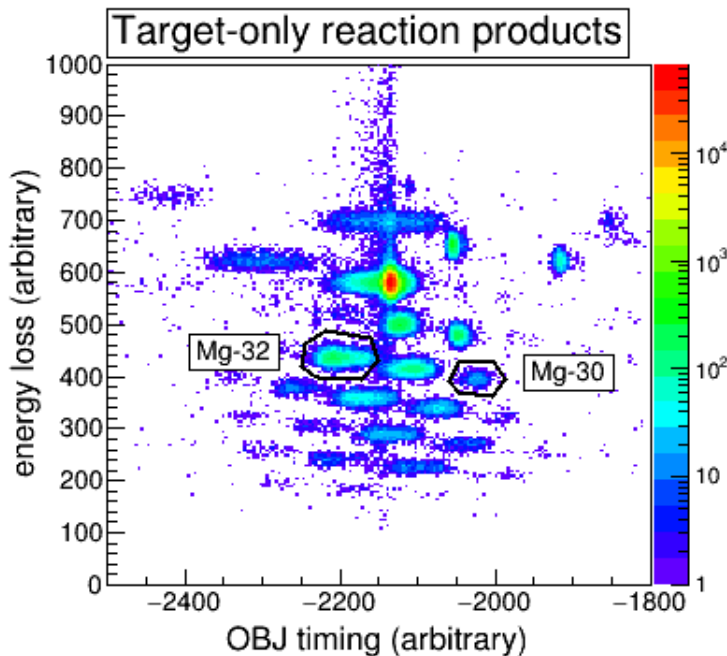
Figure 4.2: The PID for reaction products resulting from the ^{34}Si secondary beam and the ^{9}Be target in the target-only setting. The x-axis is the TOF in arbitrary units between the E1 and OBJ scintillators of the S800 spectrograph. The y-axis is the energy loss of ions traveling through the ionization chamber in arbitrary units. The software gates used to select the ^{32}Mg and ^{30}Mg reaction products are shown with solid black lines.

the energy-loss and TOF information in the PID spectrum. The ^{32}Mg reaction product is well-separated from the others so the reaction product PID gate allows most of the reaction product contaminants to be removed.

The momentum, position and angular trajectory distributions of the ^{32}Mg reaction products in the target-only setting are shown in Fig. 4.3. The y_{ta}, a_{ta} and b_{ta} distributions are all nearly Gaussian in shape. The d_{ta} distribution appears non-Gaussian because of the

91
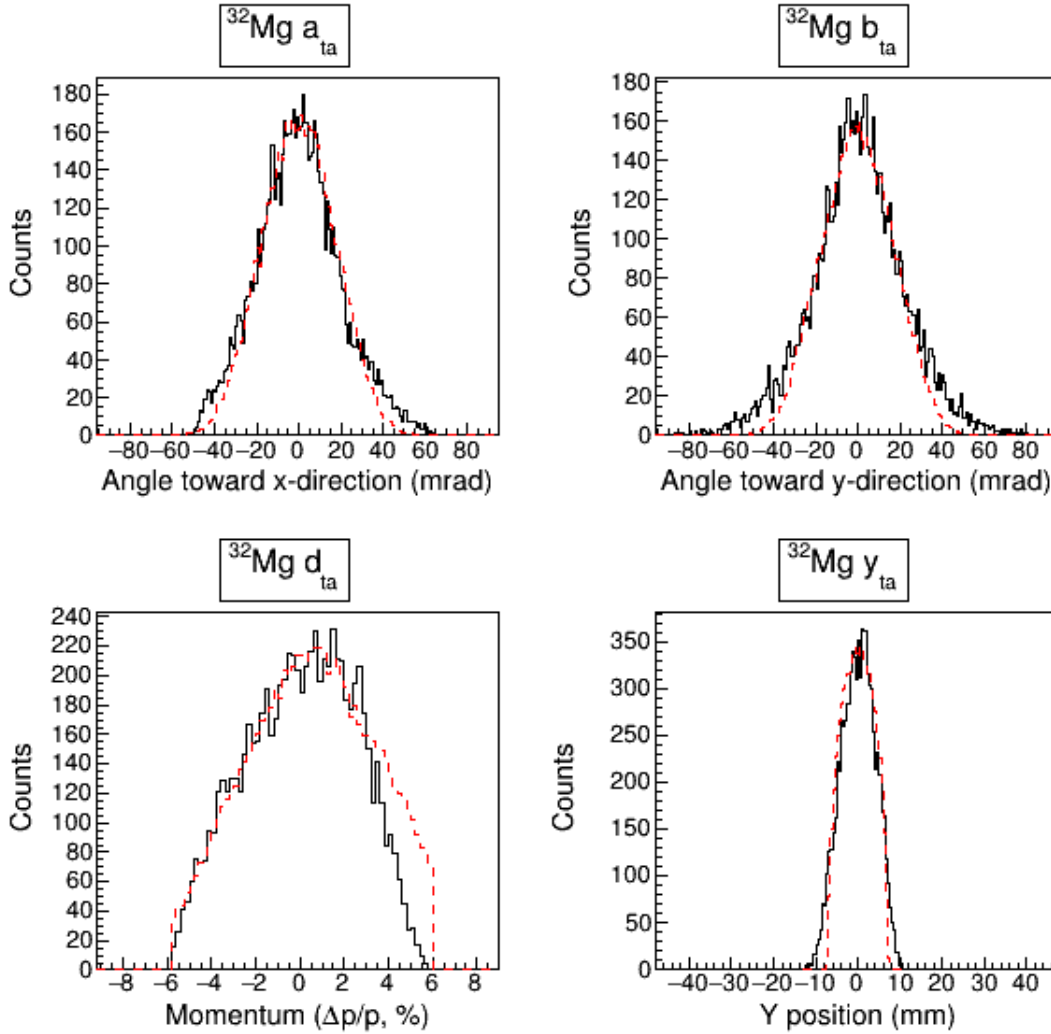
Figure 4.3: The a_{ta}, b_{ta}, d_{ta} and y_{ta} distributions of ^{32}Mg. Data is shown as a solid black line and a scaled simulation is shown as a dashed red line.

significant loss of momentum acceptance at the edges of the d_{ta} range. The profile is made by measuring the position and trajectory of the ^{32}Mg ions at the S800 focal plane event-by-event and reconstructing the parameters at the target position using an inverse map. The details on this process are provided in Chapter 3.

Gamma rays were detected with GRETINA in coincidence with the ^{32}Mg reaction products. The Doppler-shift corrected energies of the gamma rays observed in coincidence with ^{32}Mg ions during the target-only setting are shown in Fig. 4.4. The Doppler-shift correction
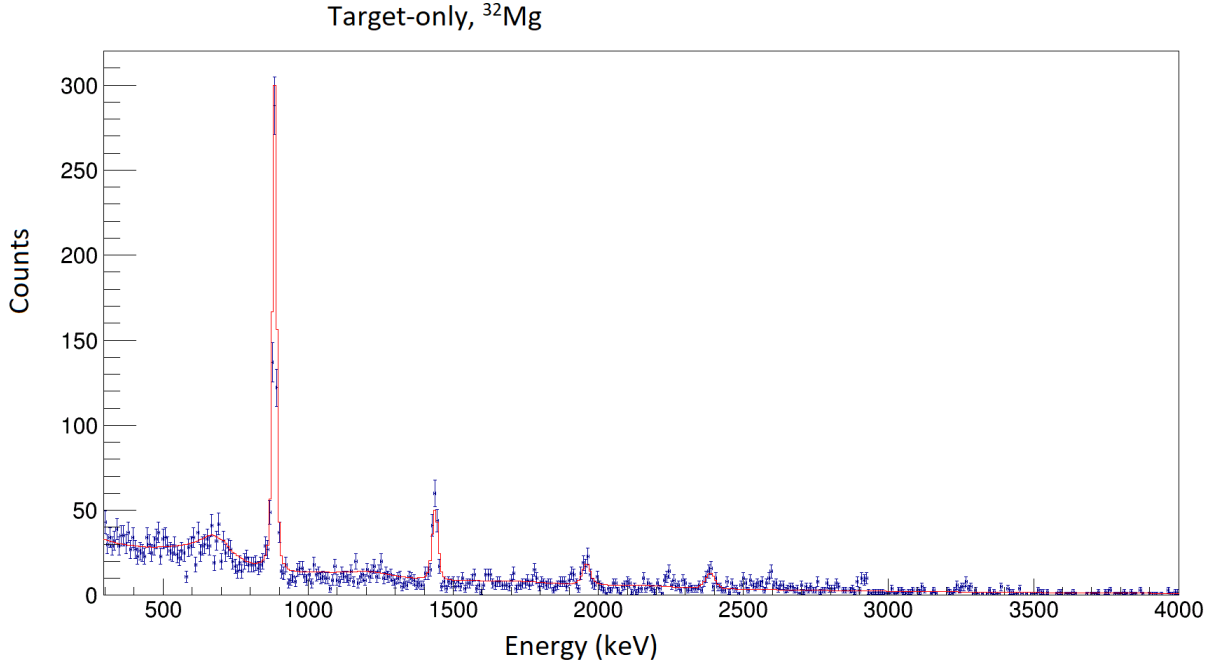
Figure 4.4: Doppler-corrected energy spectra showing four transitions in ^{32}Mg corresponding to prompt decays observed in this experiment. Data is shown with points and error bars while the simulation is shown with a solid red line.

was made assuming that the gamma rays were emitted from the back of the target foil. The value of β for the correction corresponded to the velocity of a ^{32}Mg reaction product that would travel along the center of the S800 analysis line, but is corrected by the d_{ta} value for each event. The y_{ta} position and the a_{ta} and b_{ta} angles for the ^{32}Mg ion were also included in the correction for each event.

Several gamma rays known to correspond to the decay of excited states in ^{32}Mg can be seen in Fig. 4.4. The decay of the 2_1^+ and 4_1^+ states are indicated by the 885 and 1437 keV gamma rays, respectively. Higher-lying excited states are observed as well. The 1958 keV transition feeds the 2_1^+ state while the 2384 keV transition feeds the 4_1^+ state [94]. These transitions are shown in the level scheme in Fig. 4.5. Other gamma rays with intensities below 7% can be observed as well. These gamma rays most likely correspond to the 2230-keV transition populating the 2_1^+ state from a $(3^-, 4^+)$ state at $E_x = 3117$ keV, a 2603-keV
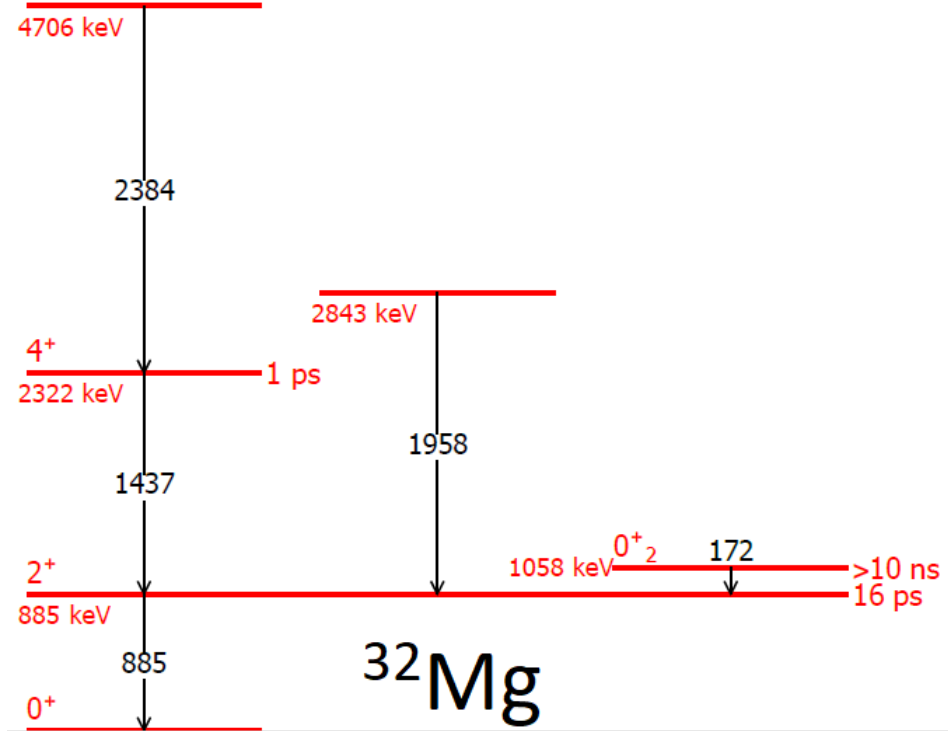
Figure 4.5: Partial level scheme of ^{32}Mg.

transition populating the 2_1^+ state from a $(1^-, 2^+)$ state at $E_x = 3490$ keV, and a 2882-keV transition populating the 4_1^+ state from a $(2^+, 3^-)$ state at $E_x = 5203$ keV [43]. There is also a possible transition at 3264(16) keV that has not been reported before. Due to the low intensities of these four transitions, they have been ignored in the lifetime analysis of the 2_1^+ and 4_1^+ states.

Table 4.1 shows the proportion of reactions that populate the four most relevant excited states in this work, scaled so that their total sums to 100%. These intensities are used in the G4Lifetime simulation for the target-only setting shown in Fig. 4.4 and are inputs for the three-foil settings. The measurement of this intensity is vital to understanding the contribution of feeding to the 2_1^+ and 4_1^+ states in order to obtain a lifetime result.

4.1.2 ^{32}Mg TRIPLEX Large-separation Setting

Data was collected with all three foils installed in the TRIPLEX device and set at a large separation: 25.0 mm between the target and first degrader, 22.0 mm between the first and second degraders. The purpose of this setting is to understand the relative number of reactions producing the ^{32}Mg excited states that occur on each foil. With three foils installed in the TRIPLEX device, each gamma-ray peak is split into three separate components. For large separations between the foils, each peak component depends only on the number of reactions that occur on a single foil, and not on the lifetime of the excited states. This is because the lifetimes of these states are all sufficiently short that an excited state populated by a reaction on one foil does not survive to pass through another foil before decaying. Any yield in the fast, reduced, and slow components of a peak are only due to reactions on the target, first degrader, and second degrader respectively.

In this experiment, no slow component was observed for any peak in the large-separation setting. This indicates that no reactions that take place on the second degrader were detected. It is almost certain that these reactions do occur, however the reaction products from the second degrader have lower momentum than reaction products from any other foil. This is because the ^{34}Si secondary beam has higher Z than any of the reaction products and therefore the ion loses more energy if it travels through the target and the first degrader

E_x (keV)	I^π	population (%)
885.3(1)	2^+	60(5)
2322.3(3)	4^+	14(3)
2843		13(2)
4706		13(2)

Table 4.1: Prompt decays in ^{32}Mg observed in this experiment. The populations observed in this work are consistent with Ref. [59].

as ^{34}Si than it would as the ^{32}Mg reaction product. In general, the ratio of the number of reactions between the first and second degraders would need to be considered, but it can be ignored in this experiment since no reactions on the second degrader were detected. The reaction ratio r will refer to the number of reactions on the target for every one reaction on the first degrader. The reaction ratios r can vary among the excited states in a single reaction product, so the ratios for the 2^+_1 state the 4^+_1 state, denoted $r(2^+_1)$ and $r(4^+_1)$, will be considered independently.

Due to the energy loss of reactions products moving through the additional foils, the velocity of the ions is lower than in the target-only setting. For the three-foil settings, a new PID for reaction products must be made. The PID spectrum for the ^{34}Si secondary beam in the three-foil settings is shown in Fig. 4.6. Due to the lower velocity, the TOF of the
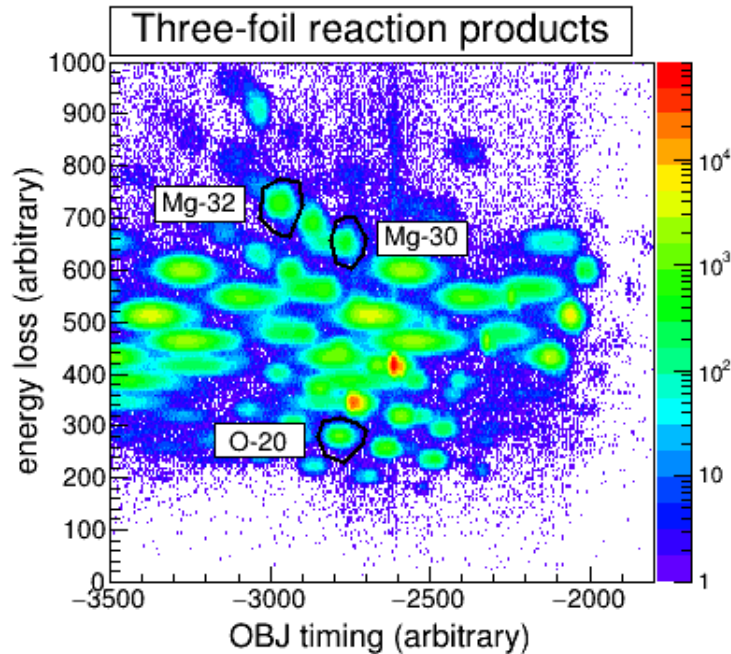
Figure 4.6: The PID for reaction products resulting from the ^{34}Si secondary beam and the ^{9}Be target in the three-foil settings. The x-axis is the TOF in arbitrary units between the E1 and OBJ scintillators of the S800 spectrograph. The y-axis is the energy loss of ions traveling through the ionization chamber in arbitrary units. The software gates used to select the ^{32}Mg, ^{30}Mg, and ^{20}O reaction products are shown with solid black lines.

reaction products changes as well.

The position, momentum, and angle distribution of ^{32}Mg ions at the target position during the three-foil settings are shown in Fig. 3.22. Every measurable parameter of the ^{32}Mg reaction product profile is wider in the three-foil setting than in the target-only setting. The additional foils cause the reaction product distributions to spread out as the ions pass through the additional foils. In the three-foil setting there is significant acceptance loss visible at the edges of the d_{ta} distribution and the a_{ta} distribution.

The Doppler-shift corrected gamma-ray spectrum in Fig. 4.7 shows the two components of the 885-keV peak in the large-separation setting. The Doppler-shift correction was optimized
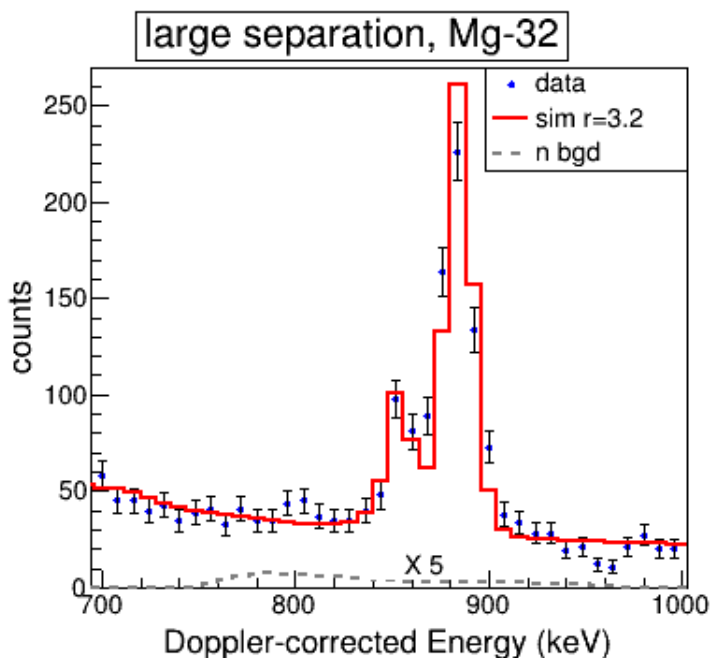
Figure 4.7: Doppler-corrected energy spectra showing the two components of the 885-keV peak in the large separation setting. Only gamma rays observed in the laboratory frame with an emission angle of $\theta < 70°$ are shown. The solid red line depicts the result of a G4Lifetime simulation that assumes a ratio of $r(2_1^+) = 3.2$ for the number of reactions on the target divided by the number of reactions on the first degrader that populate the 2_1^+ state of ^{32}Mg. The dashed gray line is the background contribution from the neutron-induced 1014-keV gamma ray from ^{27}Al and it is scaled by $\times 5$ in this image.

for decays occurring at the back of the target foil. However, due to the lifetime of the 2_1^+ state, decays can occur a few millimeters past the back of the foil in which the state was populated. This effect contributes to the width of the observed peak components. The width of the peak components is larger for emission angles θ closer to $90°$, but the width is smaller for forward-emitted gamma rays since the largest effect on the Doppler-shift for forward angles is the velocity β. Therefore, to cleanly resolve the peak components in the large-separation data, a cut was made on the gamma-ray emission angle which requires $\theta < 70°$.

In Fig. 4.7, the fast component of the peak which corresponds to reactions on the target foil appears at the nominal gamma-ray energy of 885 keV. The reduced component corresponding to the reactions on the first degrader lies at roughly 860 keV. The slow component does not appear in Fig. 4.7 due to the momentum of this reaction component lying outside of the S800 momentum acceptance.

The ratio of the number of reactions between the target and the first degrader are input into the G4Lifetime simulation. Several ratios were tested in the simulation and compared with the observed spectrum. Figure 4.8 shows the distribution of the χ^2 statistic for a number of ratio values. The best ratio is $r(2_1^+) = 3.2(6)$ reactions on the target for every one reaction on the first degrader. The simulation assuming $r(2_1^+) = 3.2$ is depicted in Fig. 4.7 as a solid red line. The 2_1^+ state has significant feeding from the 4_1^+ state which can affect the 2_1^+ lifetime result and ratio result shown here. The simulation in Fig. 4.7 and the χ^2 distribution in Fig. 4.8 include this feeding with the lifetime and ratio values for the 4_1^+ state that are determined from analyses described later in this chapter.

Neutron-induced background can play a significant role in the Doppler-shift corrected spectra when cuts are made on the emission angle θ [78]. This background occurs when
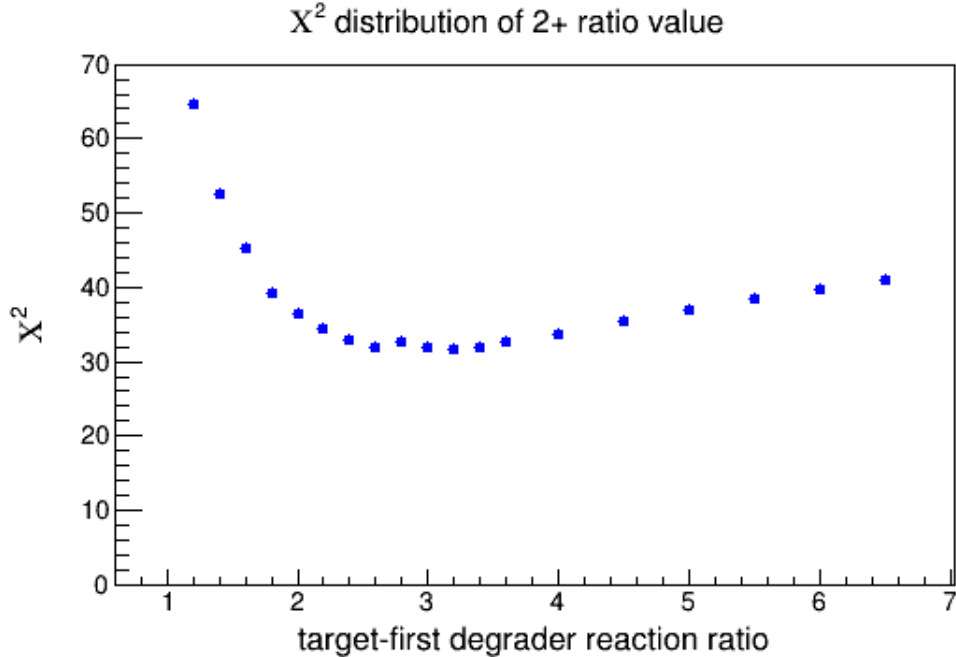
Figure 4.8: χ^2 distribution for the ratio of the number of reaction on the target to those on the first degrader for the 2_1^+ state of ^{32}Mg. The χ^2 statistic is minimized at $r(2_1^+) = 3.2(6)$. Another local minimum can be seen at a lower ratio value, but the absolute minimum is located at $r(2_1^+) = 3.2$.

residual neutrons from the reactions on the foils induce additional reactions on the materials in the laboratory. Most commonly, the neutrons encounter aluminum, such as in the beam pipe components, and germanium in GRETINA. The neutrons are captured by or scatter against these nuclei, populating excited states which emit gamma rays in the laboratory frame. When Doppler-shift corrections that are tuned to the reaction products moving at relativistic speeds are applied, the laboratory-frame neutron-induced background is spread over a large energy range and has negligible effect on the corrected spectra. However, a cut on the emission angle θ can result in the neutron-induced background becoming a significant part of certain energy ranges of the Doppler-shift corrected spectra.

In Fig. 4.7, the neutron-induced background relevant to the measurement of the reaction ratio for the 2_1^+ state is shown as a dashed gray line and is scaled up by a factor of

×5 in order to be seen. This particular neutron-induced background component is from the 1014.56-keV transition in ^{27}Al. The intensity of this background was measured in the laboratory-frame gamma-ray energy spectrum for the large separation setting where a total of 20(10) counts were observed. Then, the background was included in the G4Lifetime simulation and scaled to match the observed intensity. Ultimately, the inclusion of this background did not have a measurable effect on the reaction ratio obtained from Fig. 4.7. No other neutron-induced background was observed that would affect the Doppler-shift corrected energy range in Fig. 4.7.

The Doppler-shift corrected gamma-ray spectrum for the 4_1^+ state in the large separation setting is shown in Fig. 4.9. Like in Fig. 4.7, the Doppler-shift correction in Fig. 4.9 is
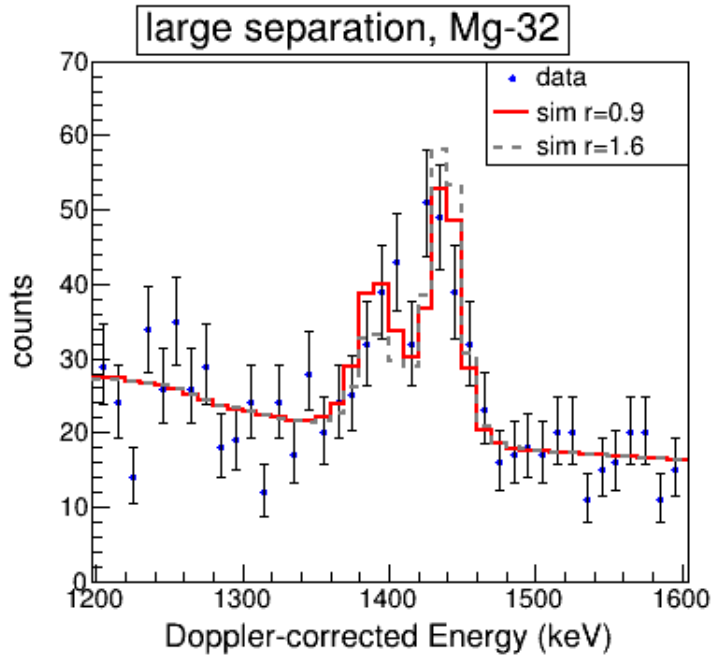
Figure 4.9: Doppler-corrected energy spectra showing the lineshape of the 1437-keV peak in the large separation setting. Only gamma rays observed in the laboratory frame with an emission angle of $\theta < 70°$ are shown. The solid red line depicts the result of a G4Lifetime simulation that assumes a ratio of $r(4_1^+) = 0.9$ for the number of reactions on the target divided by the number of reactions on the first degrader that populate the 4_1^+ state of ^{32}Mg. The dashed gray line assumes a ratio of $r(4_1^+) = 1.6$.

100

optimized for decays at the back of the target foil, and a gate is made on the gamma-ray emission angle $\theta < 70°$. The fast and reduced peak components are visible, but the slow component does not appear because reaction products produced in the second degrader are not accepted by the S800 spectrograph. The reaction ratio that best fits the above spectrum is $r(4_1^+) = 0.9(2)$, which is the value assumed in the simulation depicted with the solid red line. Figure 4.10 shows the χ^2 distribution for several different assumptions of this ratio value. The reaction ratio is quite different between the 4_1^+ and the 2_1^+ state, indicating the
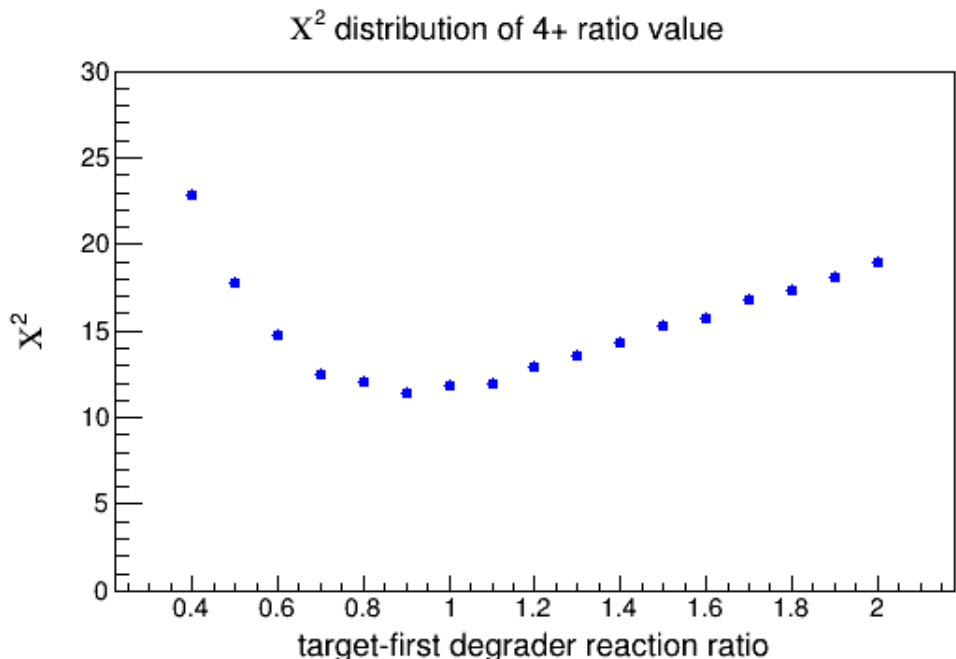
Figure 4.10: χ^2 distribution for the ratio of the number of reaction on the target to those on the first degrader for the 4_1^+ state of ^{32}Mg. A clear minimum is visible at $r(4_1^+) = 0.9(2)$.

importance of measuring the reaction ratios for the excited states separately.

4.1.3 ^{32}Mg TRIPLEX Short-separation Settings

To measure the lifetimes of the 2_1^+ and 4_1^+ states, the foils are placed so that the time it takes the reaction products to travel between them is similar to the excited state lifetimes.

Previous measurements of the 2_1^+ state suggest a lifetime of $\tau(2_1^+) = 16(3)$ ps [87]. In this experiment, reaction products travel at roughly $v = 0.3c$ so the 2_1^+ excited state will travel approximately 1.6 mm after it is produced. The second degrader was set at different distances from the first degrader to be sensitive to the 2_1^+ lifetime, as summarized in Table 3.1. To be sensitive to the shorter 4_1^+ lifetime, the target and the first degrader were positioned with zero separation. The number of observed counts of the 4_1^+ state were much smaller than for the 2_1^+ state, so the target and first degrader were left in this one setting to accumulate the necessary statistics to be sensitive to the 4_1^+ lifetime.

The foils installed in the TRIPLEX device for the short separation settings are the same as for the large separation setting. Therefore, the reaction product PID is the same as that shown in Fig. 4.6, and distributions of the position, momentum, and angular trajectory of the ^{32}Mg reaction products are the same as those shown in Fig. 3.22.

Figure 4.11 shows the 885-keV peak in the four settings used to determine the lifetime of the 2_1^+ state in ^{32}Mg. The Doppler-shift correction is optimized for decays occurring after the second degrader. The Doppler-shift effect is most significant at forward angles, so to enhance the sensitivity to the Doppler-shift and therefore the lifetime, a gate is placed on the gamma-ray emission angle, $\theta < 50°$. Two components of the 885-keV peak are clearly visible: the reduced component corresponding to decays after the first degrader, and the slow component corresponding to decays after the second degrader. The fast component is small enough that it is hardly visible against the background. The lack of fast component is expected since the previous 2_1^+ lifetime results suggest a value that is long enough for most ^{32}Mg reaction products to pass the target before decaying.

The lifetime of the 2_1^+ state was determined by comparing the data to simulations that assumed various values for the 2_1^+ lifetime in 1-ps increments. The lifetime result for each
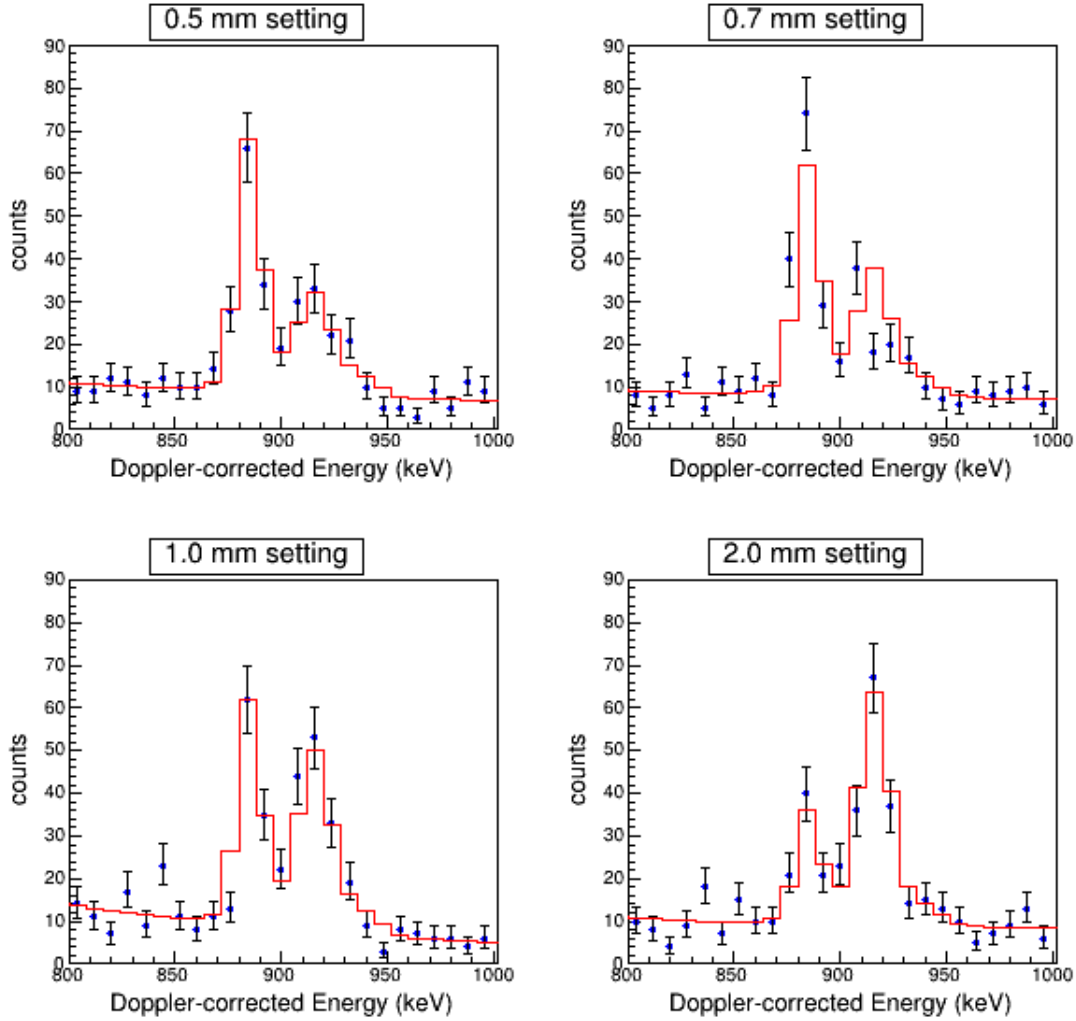
Figure 4.11: Doppler-corrected energy spectra showing the two components of the 885-keV peak. A gate is placed on the gamma-ray emission angle $\theta < 50°$. The red lines depict the results of G4Lifetime simulations that assume a lifetime of 19 ps for the 2_1^+ state of ^{32}Mg.

setting was found from the minimum of the χ^2 distribution, then the values from the four settings with different first degrader-second degrader separations were averaged. The lifetime of the 2_1^+ state when considering all four settings is $\tau(2_1^+) = 18.7(1.2)$ ps, considering only the statistical uncertainty. The solid red lines in Fig. 4.11 show the results of the G4Lifetime simulation with $\tau(2_1^+) = 19$ ps assumed. Feeding from the 4_1^+ and the $E_x = 2843$ keV states is included in the simulation in the proper proportions according to the intensity results of

Table 4.1. In this feeding scheme, the ratio $r(4^+_1)=0.9$ is used as determined from the large separation analysis and the lifetime of the 4^+_1 state is set to the value determined later in this section. The lifetime of the $E_x = 2843$ keV state could not be well-constrained in this dataset. The 2843-keV state has been observed previously but no lifetime or spin-parity assignment has been made [94]. In the simulated feeding of the 2^+_1 state the lifetime of the 2843-keV state is assumed to be $\tau = 1.0$ ps. Since feeding from the 2843 keV state is a small proportion of the population of the 2^+_1 state, the feeding state lifetime has a relatively small impact on the 2^+_1 result. For example, varying the $E_x = 2843$-keV state lifetime from 0.1 ps to 3 ps causes the 2^+_1 lifetime to change by only 1 ps. The systematic uncertainty in the lifetime of the 2^+_1 state is 1.1 ps where the largest contribution comes from the unknown lifetime of the $E_x = 2843$-keV state. The final result of this measurement concludes that the lifetime of the 2^+_1 state is $\tau(2^+_1) = 18.7 \pm 1.2(\text{stat.})\pm 1.1(\text{syst.})$ ps.

While $\tau(2^+_1) = 18.7 \pm 1.2(\text{stat.})\pm 1.1(\text{syst.})$ ps is the final result for the data over all settings, the individual settings randomly deviate from that value. This is clearest in the 0.7-mm setting where the slow component of the peak is larger than the corresponding simulated response based on the lifetime of $\tau(2^+_1) = 19$ ps. The best match to the 0.7-mm setting alone is $\tau(2^+_1) = 28^{+5}_{-4}$ ps and is shown in Fig. 4.12. Figure 4.12 shows the Doppler-shift corrected gamma-ray energy with 14 keV/bin instead of 8 keV/bin which was used in Fig. 4.11. The larger bin size reduces the impact of statistical fluctuations and makes the analysis of the 0.7-mm setting more sensitive to the height of the peak components and therefore the 2^+_1 lifetime. The Doppler-shift correction and emission angle θ gate used for the analysis of Fig. 4.12 is the same as with all the other short-distance settings shown in Fig. 4.11. The best-fit lifetime for each individual setting is shown in Fig. 4.13 along with the weighted average result. Figure 4.13 highlights the difference between the 0.7-mm
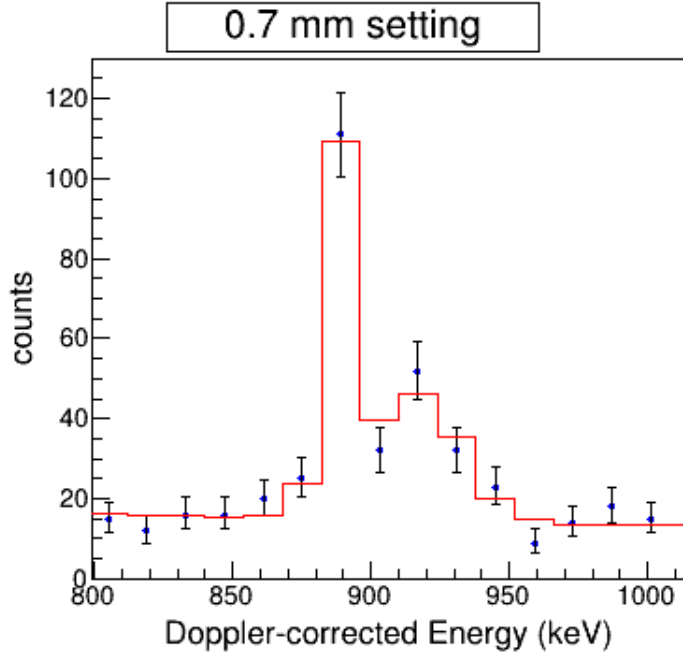
Figure 4.12: Doppler-corrected energy spectra showing the reduced and slow components of the 885-keV transition in the 0.7-mm setting. The red solid line depicts the results of G4LifeTime simulation that assumes a lifetime of 28 ps for the 2_1^+ state of ^{32}Mg.

setting and the other short-distance settings. The individual measurement from the 0.7-mm separation setting has little bearing on the weighted average due to the large uncertainty in the 0.7-mm setting. By excluding the 0.7 mm setting, the weighted average becomes $\tau(2_1^+) = 18.0(1.3)$ ps where the error is only from the statistical uncertainty. This result is consistent with the original conclusion that includes all four short separation settings.

Figure 4.14 shows the lineshape of the 1437-keV peak over all runs in which the target and first degrader were at 0.0 mm of separation from one another. The Doppler-shift correction in Fig. 4.14 is optimized for decays occurring at the back of the target. A gate is placed to show only the forward-emitted gamma rays, $\theta < 70°$. The gate on the emission angle θ is larger than in the study of the 2_1^+ lifetime in order to increase the counts for the 4_1^+ peak. In this case the lifetime of the 4_1^+ state is short enough that only the fast and the reduced components of the peak appear in the spectrum. Too few decays occur after the second

105
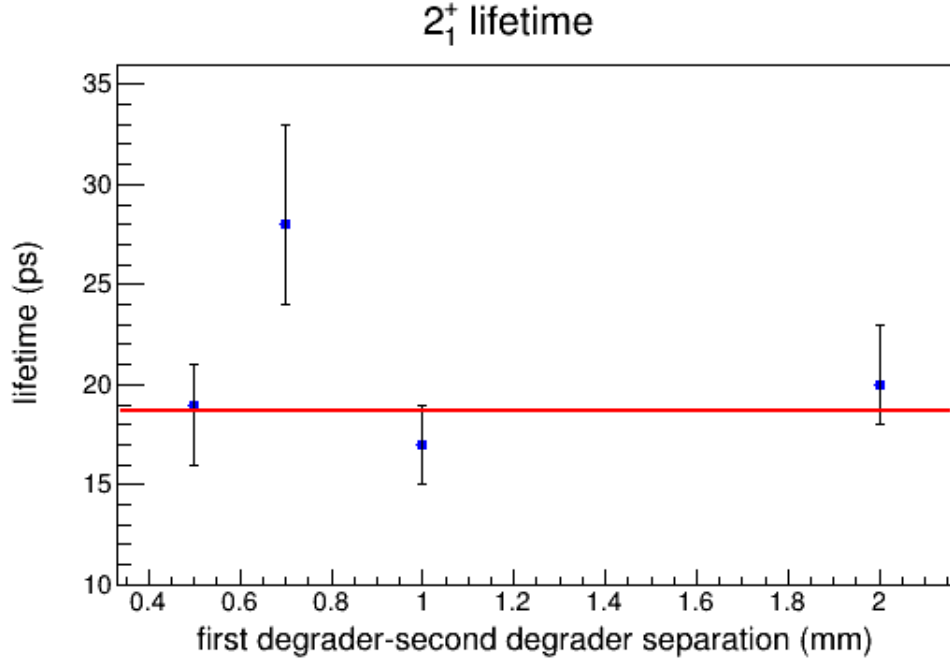
Figure 4.13: The best-fit lifetime for each of the four short-separation settings is shown with the points and error bars. The weighted-average lifetime of $\tau(2_1^+) = 18.7 \pm 1.2(\text{stat.})$ ps is shown as a solid red line.

degrader for the slow component to be visible against the background. Instead of appearing as two separate peaks, the fast and reduced components instead form a smooth lineshape which is sensitive to the short lifetime.

The lifetime result from this spectrum is $\tau(4_1^+) = 0.9(2)$ ps where the error is from statistical uncertainty alone. The solid red line shows the results of the G4Lifetime simulation when a 0.9-ps lifetime is assumed, while the dashed gray line assumes a 1.6-ps lifetime. Feeding from higher-lying excited states, such as the state at $E_x = 4706$ keV, may play a role in this result. Since the lifetime of the 4706-keV feeding state is unknown, the lifetime of the 4_1^+ state reported here is an effective lifetime which includes the time it takes for the higher-lying states to decay. Beside these feeding considerations, the major systematic uncertainty contribution is from the target-first degrader zero-distance offset which was found to be 30 μm. This contributes a systematic uncertainty of $+0.1$ ps. The final 4_1^+ lifetime is
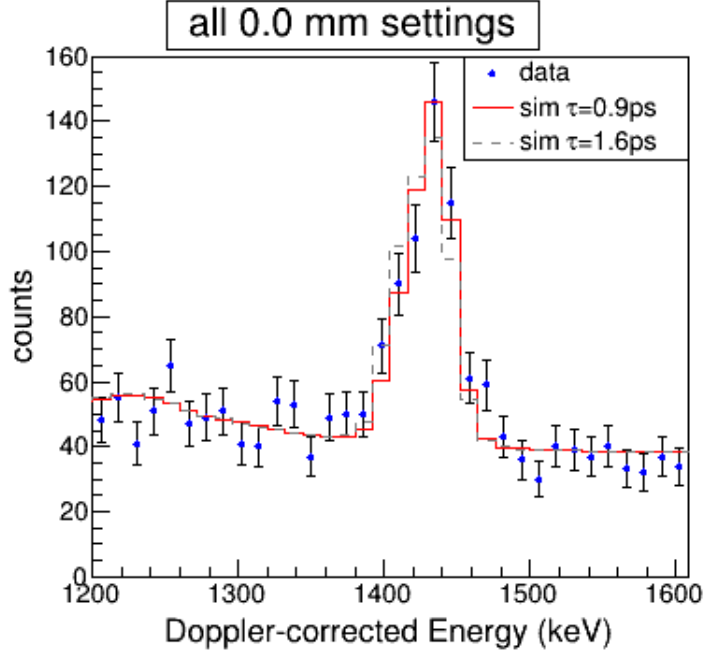
Figure 4.14: Doppler-corrected energy spectra showing the lineshape of the 1437-keV transition. The solid red line depicts the results of GEANT4 simulations that assume a lifetime of 0.9 ps for the 2_1^+ state of ^{32}Mg, while the gray dashed line assumes a lifetime of 1.6 ps.

$$\tau(4_1^+) = 0.9 \pm 0.2(\text{stat.}) \pm 0.1(\text{syst.}) \text{ ps.}$$

4.2 ^{30}Mg 2_1^+ State

Byproduct data for ^{30}Mg was also collected during the target-only and three-foil settings, as can be seen in the reaction product PID plots shown in Fig. 4.2 and Fig. 4.6. The 2_1^+ state of ^{30}Mg at $E_x = 1483$ keV has a lifetime of 2.2(3) ps [95] as shown in the level scheme in Fig. 4.15. The lifetime of this state can be measured using the same procedure that was used to measure the lifetime of the 4_1^+ state in ^{32}Mg. This known data set is valuable to confirm the the new results presented in this work.

In the target-only setting there were too few counts to obtain the intensity of the gamma rays in ^{30}Mg. Instead, the three-foil large-separation setting was used without a gate on the
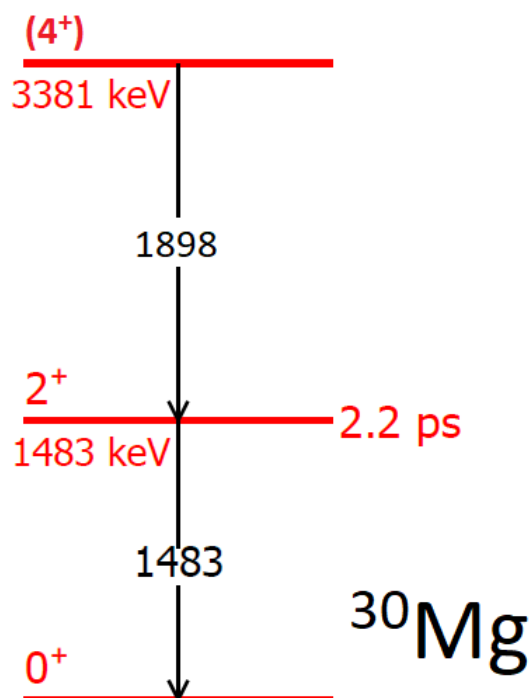
Figure 4.15: Partial level scheme of ^{30}Mg.

gamma-ray emission angle θ. Figure 4.16 shows the Doppler-corrected gamma-ray spectrum for ^{30}Mg in the three-foil large-separation setting. The 2_1^+ peak can be seen at 1483 keV and a second peak is observed near 1898 keV corresponding to the decay of the (4^+) state at $E_x = 3381$ keV to the 2_1^+ state. From this plot it was determined that 67(7)% of the ^{30}Mg reaction products populate the 2_1^+ state directly, while 33(7)% populate the 4_1^+ state either directly, or through the unobserved feeding transitions.

Only the ^{30}Mg reaction products that were produced on the target were accepted by the S800 spectrograph. The ^{30}Mg reaction products that were produced on either the first degrader or the second degrader had momentum that was too low and did not make it to the S800 focal plane. As a result, the only component of any gamma-ray peak from ^{30}Mg that can be observed is the target component. Therefore, it is not necessary to determine any of the ratios of reactions among the three foils.
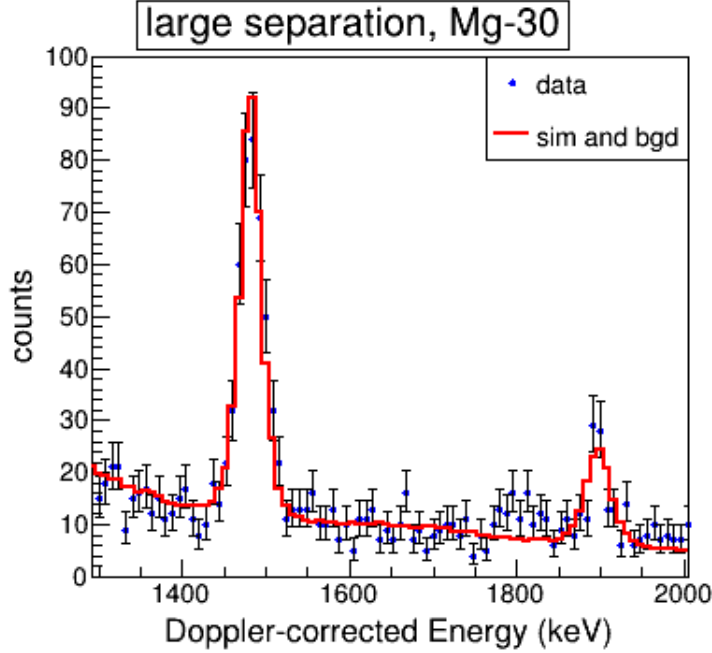
Figure 4.16: Doppler-corrected energy spectra of gamma rays from ^{30}Mg in the three-foil, large-separation setting. The red solid line depicts the results of G4Lifetime simulations with the best-fit intensity of the gamma rays. No gate was placed on the emission angle θ in order to increase the statistics of the observed peaks.

Due to the short nature of the 2_1^+ state lifetime ($\tau < 5$ ps), it was best to analyze the lifetime in the same manner the 4_1^+ state of ^{32}Mg was analyzed. All the short-separation settings were summed together to gain large statistics for the Doppler-shift corrected lineshape of the 1483-keV transition. The lineshape was the result of decays occurring through the target and first degrader materials. Figure 4.17 shows the lineshape of the 1483-keV gamma ray from ^{30}Mg. The Doppler-shift correction was optimized for decays at the back of the target. The gate on the gamma-ray emission angle is $\theta < 50°$. The lifetime of the 4_1^+ state is not known but was assumed to be $\tau = 0.5$ ps. As in the measurement of the 4_1^+ lifetime in ^{32}Mg, the lifetime of the 2_1^+ state in ^{30}Mg is also an effective lifetime. The main source of systematic uncertainty is the zero-distance offset in the target-first degrader separation, as it was in the measurement of the 4_1^+ lifetime in ^{32}Mg. The result from the 2_1^+ lifetime
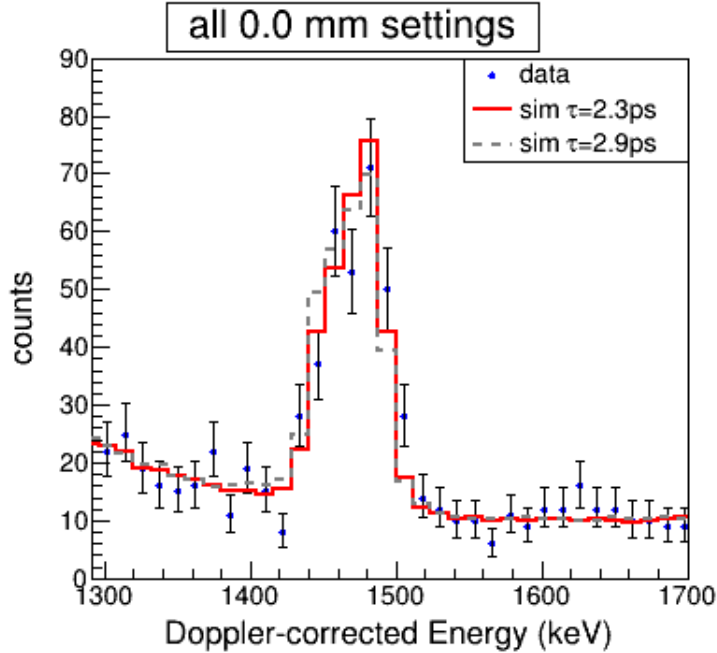
Figure 4.17: Doppler-corrected energy spectra of gamma rays from ^{30}Mg in the three-foil, short-separation setting. A gate was placed on the gamma-ray emission angle $\theta < 50°$. The solid red line depicts the simulation results assuming a lifetime of 2.3 ps. The dashed gray line corresponds to a simulation with a lifetime of 2.9 ps.

measurement in ^{30}Mg is $\tau(2_1^+) = 2.3 \pm 0.3$(stat.)$\pm 0.1$(syst.) ps. This is consistent with the previously measured value of 2.2(3) ps [95].

4.3 ^{20}O 2_1^+ State

Another measurable lifetime in this dataset is the 2_1^+ state of ^{20}O which is depicted in the level scheme in Fig. 4.18. Past measurements of the 2_1^+ lifetime have varied and they include the results of RDM measurements of $\tau = 10.7(4)$ ps [96] and $\tau = 14.2(8)$ ps [97], and a DSAM measurement of $\tau = 9.8(7)$ ps [98]. Whichever particular measurement is correct, the lifetime is within the applicable range for a RDM measurement in this experiment.

The ^{20}O reaction product was not observed in the target-only PID (Fig. 4.2). Therefore
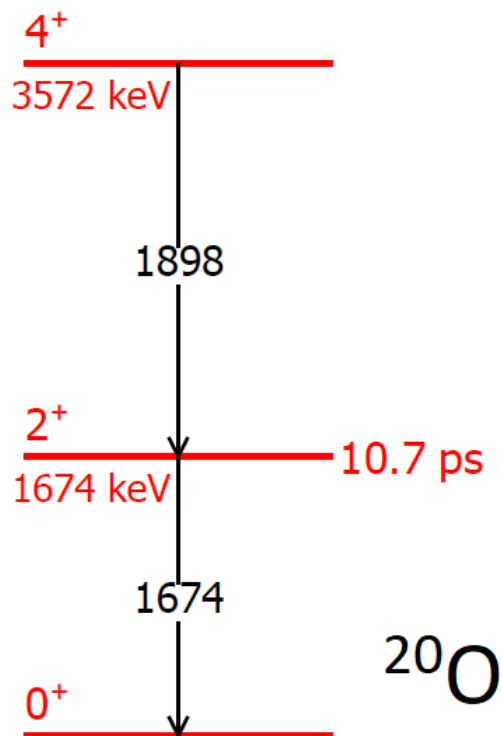
Figure 4.18: Partial level scheme of ^{20}O.

all available data for ^{20}O comes from the three-foil settings where the reaction product can be identified with the PID shown in Fig. 4.6.

Figure 4.19 shows the momentum, position and angular trajectory distributions for ^{20}O reaction products. An unusual momentum distribution was observed for ^{20}O, depicting two Gaussian peaks. This was found to be due to the threshold setting for the CRDC's. The threshold was chosen to be useful for reaction products near ^{32}Mg. For the reaction products with lower Z, the charge deposited in the CRDC's can be too low to reach the threshold and be recorded. The electronic behavior for the all the CRDC pads is not identical, but resulted in the loss of more low-Z reaction products which impinged near the central pads of the CRDC's than those near the edges. As a result, two peaks appear in the distribution where the pads accepted more of the low-Z reaction products. This was confirmed by checking the other oxygen reaction products as well as fluorine and nitrogen isotopes where similar
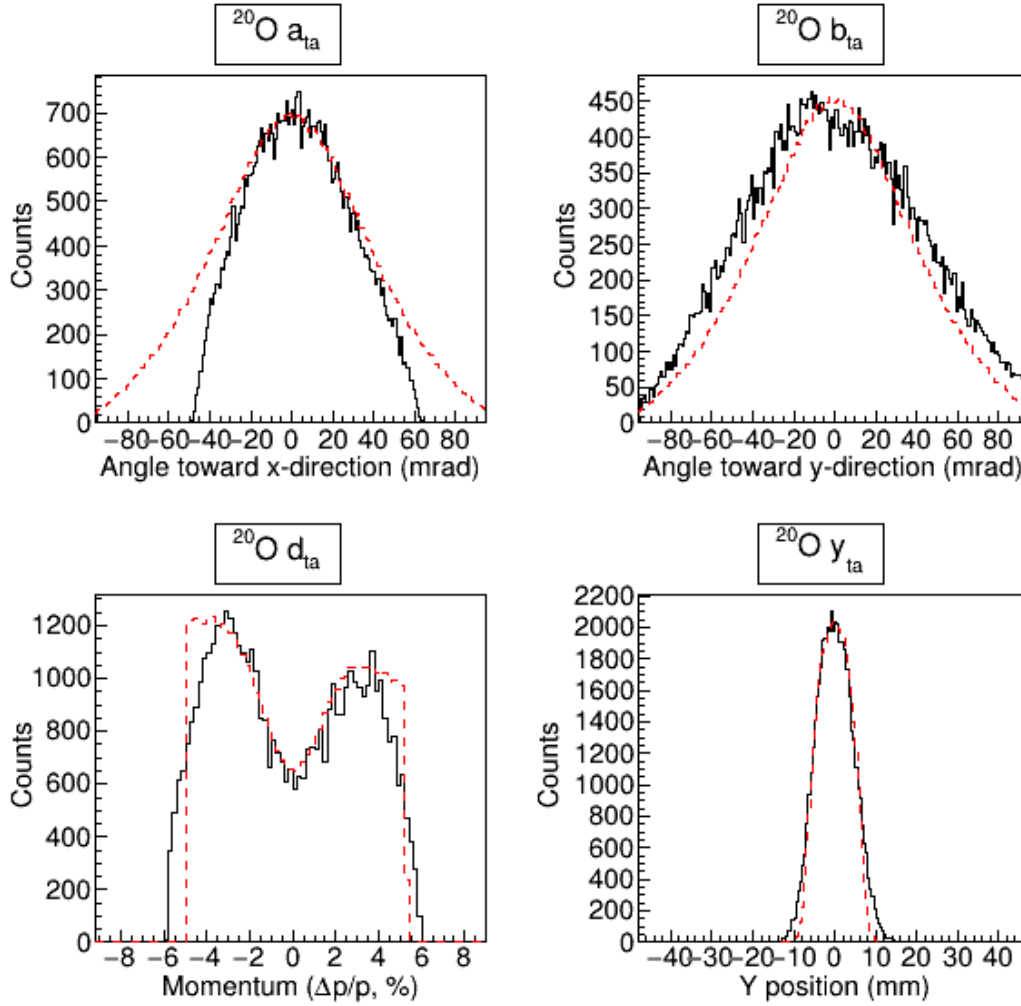
Figure 4.19: The a_{ta}, b_{ta}, d_{ta} and y_{ta} distributions of the ^{20}O reaction product in the three-foil settings. Data is shown as a solid black line and a scaled simulation is shown as a dashed red line.

momentum distributions were observed.

The Doppler-shift corrected gamma-ray energy spectrum for ^{20}O in the three-foil large-separation setting is shown in Fig. 4.20. No gate is placed on the emission angle θ in Fig. 4.20. The 1674-keV peak components correspond to the decay of the 2_1^+ state while the small contribution at 1898-keV is due to the 4_1^+ state which feeds the 2_1^+ state. The proportion of reactions that populate the 2_1^+ state is 80(9)% while the population of the 4_1^+ state is 20(9)%.
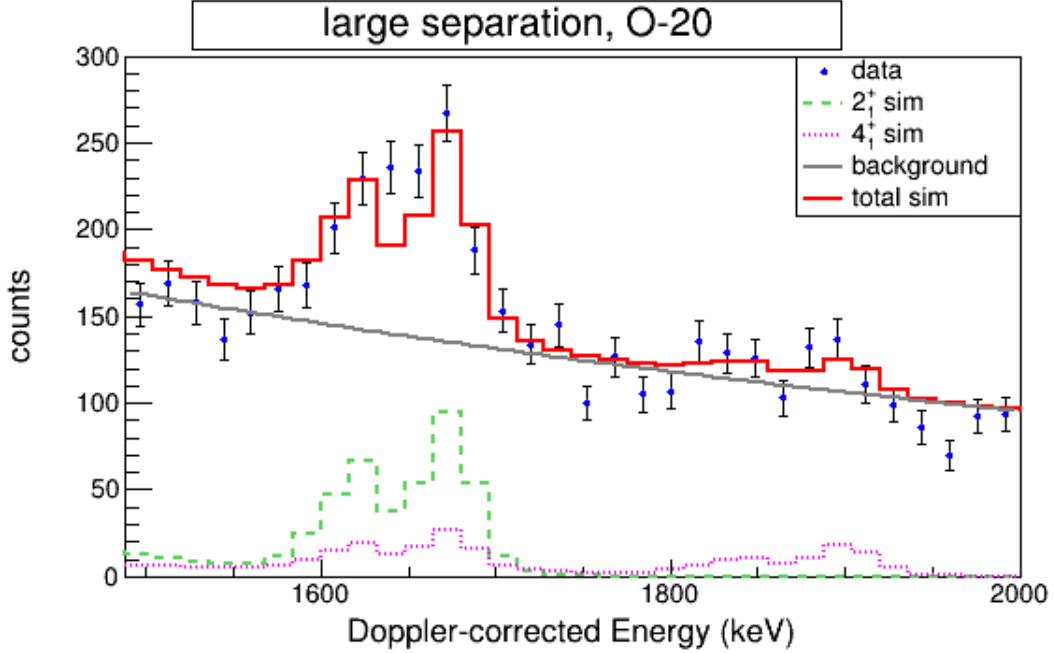
Figure 4.20: Doppler-corrected energy spectra of gamma rays from ^{20}O in the three-foil, large-separation setting. The data shows contributions at 1674-keV from the decay of the 2_1^+ state and at 1898-keV from the 4_1^+ state. The contributions of the populations of the 2_1^+ state and the 4_1^+ state are estimated with the simulated responses depicted with the dashed green and the dotted purple lines respectively. The solid gray line is an exponential background and the solid red line is the sum of the two simulation components and the background.

The ratio of the number of reactions on the target to the first degrader was also obtained from the three-foil large-separation dataset. The best-fit ratio to the large-separation data is $r = 1.0(2)$. The simulated response in Fig. 4.20 assumes a reaction ratio of $r = 1.0$ for both the 2_1^+ and the 4_1^+ states.

The 4_1^+ feeding of the 2_1^+ state plays a significant role in the measurement of the 2_1^+ lifetime. A measurement of the 4_1^+ lifetime has never been reported. A rough estimation of the 4_1^+ lifetime can be obtained from the present experiment. Figure 4.21 shows the Doppler-shift corrected energy spectrum for the 1898-keV transition from the 4_1^+ state for all the short-separation settings summed together. It was necessary to sum all the short-
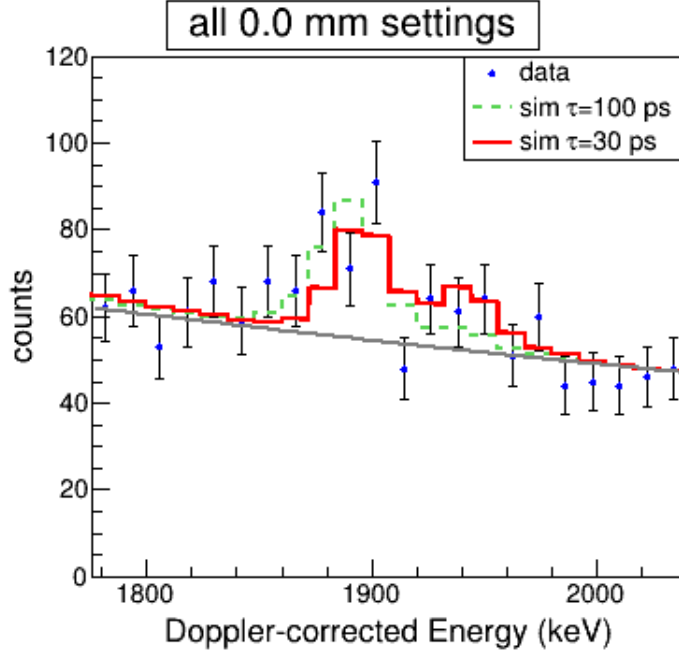
Figure 4.21: Doppler-corrected energy spectra of gamma rays from ^{20}O in the three-foil, short-separation setting. A gate has been placed on the gamma-ray emission angle $\theta < 50°$. The dashed green line and the solid red line are from G4Lifetime simulations assuming a lifetime of 100 and 30 ps respectively for the 4_1^+ state in ^{20}O. The solid gray line is an exponential background.

separation settings to result in sufficient statistics. Through comparison with simulations, the lifetime of the 4_1^+ state is estimated to be $\tau(4_1^+) = 100(70)$ ps where the error is from statistical uncertainty alone.

The Doppler-shift corrected gamma-ray energy spectra for the 2_1^+ state are shown in Fig. 4.22. The best-fit lifetime result for the 2_1^+ state of ^{20}O is $\tau(2_1^+) = 16(2)$ ps from statistical uncertainty alone, when the feeding from the 4_1^+ state is neglected. This result, reflecting the effective lifetime of the 2_1^+ state in this experiment, agrees with the previous result from Ref. [97]. The lifetime of the 2_1^+ was evaluated again with an estimation of the feeding contribution from the 4_1^+ state. The 4_1^+ state was included assuming 20% direct population of the 4_1^+ state and and 80% of the 2_1^+ state and a 4_1^+ lifetime of 100 ps. Under
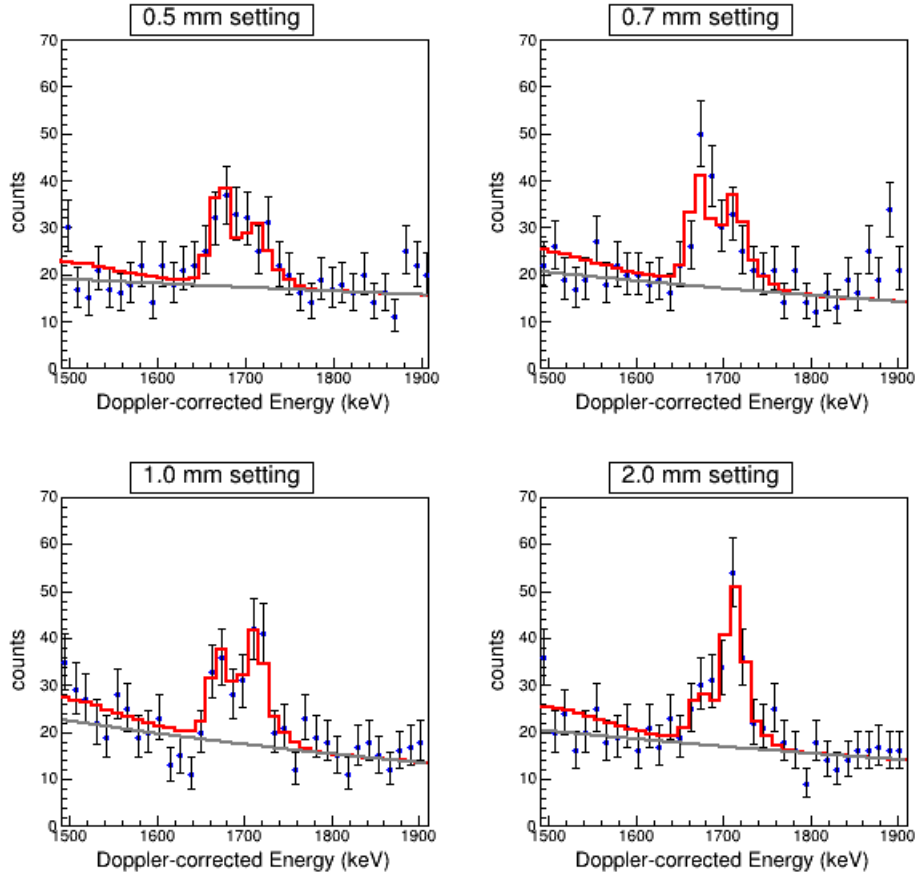
Figure 4.22: Doppler-corrected energy spectra of gamma rays from ^{20}O in each of the the three-foil, short-separation settings. A gate has been placed on the gamma-ray emission angle $\theta < 50°$. The solid red lines are the results of a G4Lifetime simulation assuming a lifetime of $\tau(2_1^+) = 16$ ps and no feeding from the 4_1^+ state. The solid gray lines are exponential backgrounds fit to a large energy region.

these conditions, the lifetime result for the 2_1^+ state became $\tau(2_1^+) = 11.8(13)$ ps where the error corresponds only to the statistical error in this data set. This feeding-corrected value is much closer to the results of Refs. [98] and [96]. The feeding and lifetime of the 4_1^+ is poorly constrained with this dataset but play a major role on the 2_1^+ lifetime, resulting in a significant systematic uncertainty for the 2_1^+ lifetime of 5 ps.

4.4 ^{31}Mg $(7/2^-)$ Isomer

The analysis of long-lived states requires a different approach than the RDM method used to find the results in the previous sections. The CDM method is applicable for the isomers measured in this work which include states in ^{32}Mg and the byproduct ^{31}Mg reaction product. ^{31}Mg will be described first since the lifetime of its isomer is well known and it can be used as a demonstration of the novel CDM measurement. ^{31}Mg has a $(7/2^-)$ isomeric state at 461 keV with a lifetime of $\tau = 15.1(12)$ ns. The measurement of the $(7/2^-)$ lifetime using the CDM will demonstrate the validity of the new method.

The decays we analyzed in ^{31}Mg emit two gamma rays in cascade that both may interact with GRETINA multiple times. As in the analysis of the short-lived states, the interaction point with the largest energy deposit was chosen as the first interaction point of one gamma ray. Then an add-back routine analogous to that used in Ref. [78] was implemented to sum energies within an $r = 80$ mm sphere centered on the first interaction point. Using the remaining interaction points, a second gamma ray was reconstructed with the first interaction point and add-back energy found in the same manner. In general, if interaction points still remain, the same add-back routine can be repeated to define additional gamma rays. However, to improve the signal-to-noise ratio for the CDM measurement, we selected events with exactly two interaction spheres (gamma-ray multiplicity two). GRETINA was most efficient for decays occurring 52 to 92 cm downstream of the target, corresponding to ± 20 cm from the center of GRETINA, so only events within this range were selected to reduce the background contribution. According to the CDM technique, if one gamma ray γ_1 is assigned to the known transition, then the Doppler-corrected energy of the other gamma ray γ_2 is determined event by event based on the common decay position (see Fig. 2.5).

The CDM is applied to the ^{31}Mg products to find the Doppler-shift corrected energy of gamma rays from the isomeric decay and the result is shown in Fig. 4.23(a) together with a partial level scheme. In this case, the 171-keV transition from the 221-keV excited state was used as a reference to determine the decay location of the isomer at 461 keV. The 171-keV transition plays the role of γ_1 in Fig. 2.5, while the 240-keV transition is γ_2. The peak in Fig. 4.23(a) was fit with a Gaussian with a centroid energy of 244(5) keV which is consistent with the literature value of 239.9(5) keV. The low energy of the 240-keV gamma ray suggests that all interactions are likely to occur within a 20-mm sphere. Therefore, to improve the sensitivity to events of interest, an additional gate requiring the 240-keV gamma ray to deposit all energy within $r = 20$ mm of the first interaction point was implemented. This gate results in the lower, filled spectrum of Fig. 4.23(a) which shows a reduced background while retaining 66% of the peak counts. The scaled background spectrum in black in Fig. 4.23 was obtained by analyzing all ^{34}Si reaction products excluding the Mg isotopes, which mostly consists of ^{34}Si and ^{33}Al.

The energy spectrum of ^{31}Mg was studied further with a G4Lifetime simulation that included the isomeric 461-keV state, the lower-lying 221- and 50-keV states, and the gamma-ray transitions at 240, 221, 171, and 50 keV, as shown in the level scheme of Fig. 4.23(a). The simulated spectrum was added to the background and scaled to fit the measured peak at 244 keV. The simulated energy of the transition from the isomer that best reproduced the data was 239(1) keV, as is shown with the red line in Fig. 4.23(a). The difference between the best-fit energy of 239 keV and the peak centroid energy of 244 keV was attributed to the $\tau = 192$ ps lifetime of the 221-keV state, corresponding to an average distance of 2 cm between the emission points of the 171-keV and the 240-keV gamma rays.

The lifetime of the 461-keV state was studied using the distribution of decay points along
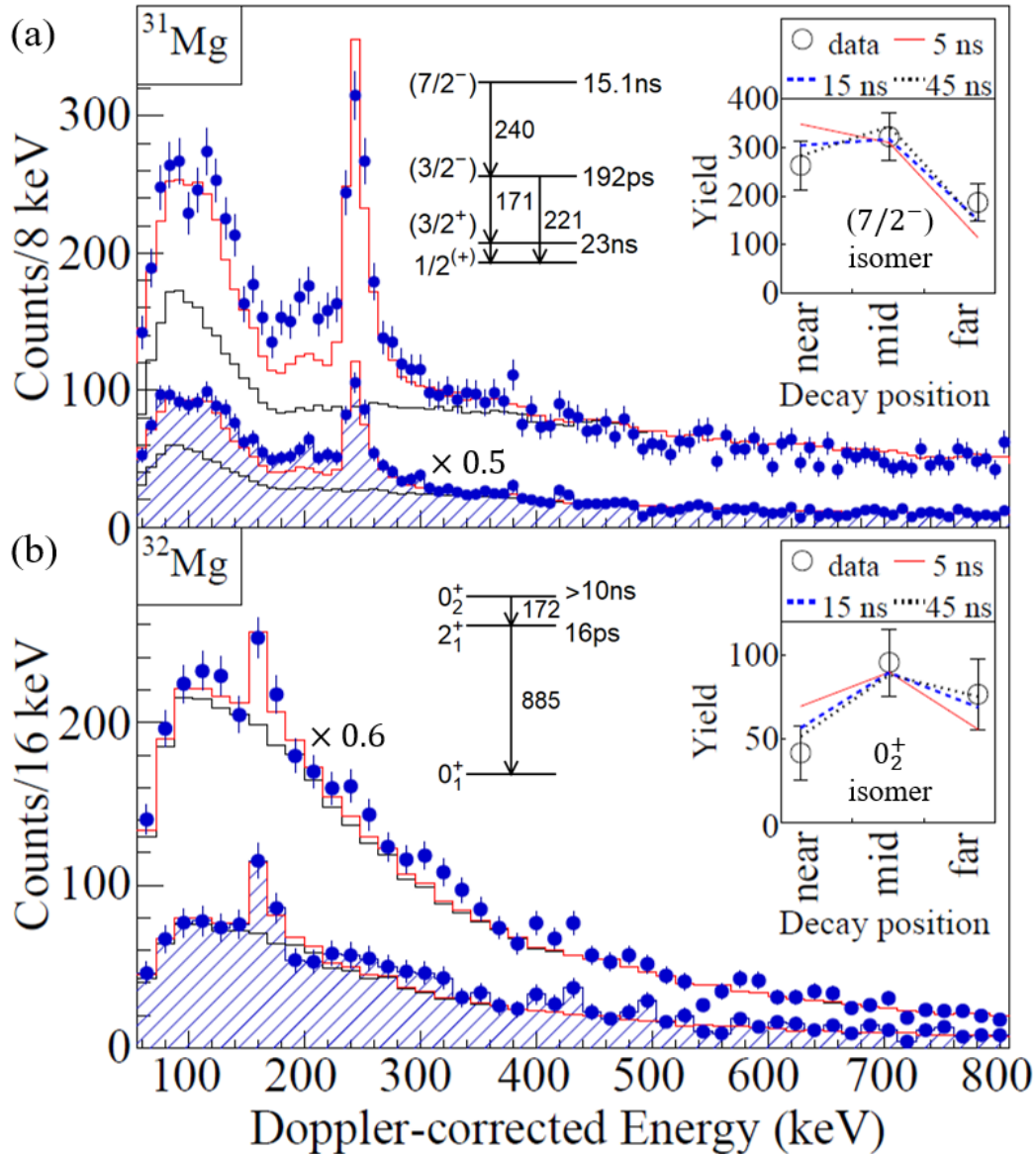
Figure 4.23: Doppler-corrected gamma-ray energy spectra are shown for data (blue circles), background from the scaled response of reaction products excluding the Mg isotopes (black lines), and the sums of the simulated and background responses (red lines). ^{31}Mg is shown (a) in the upper spectra and the constraint that the 244-keV transition only interacts within $r = 20$ mm of its first interaction is included in the lower, filled spectrum (scaled by 0.5). ^{32}Mg is shown (b) with the $r = 20$ mm gate applied to the 170-keV gamma ray in the upper spectrum (scaled by 0.6) and with additional gates requiring proper identification of the interaction points of the 885-keV gamma ray in the lower, filled spectrum. Insets show the number of decays near (250 to 525 mm), at mid-distance (525 to 700 mm) and far from the target (700 to 1000 mm). The data (open circles) is compared to simulations assuming lifetimes of 5 ns (red solid line), 15 ns (blue dashed line), and 45 ns (black dotted line).

118

the beam line shown in the inset of Fig. 4.23(a). Although GRETINA is most efficient for decays from 52 cm to 92 cm downstream of the target, the decay trend was analyzed in a larger region from 25 to 100 cm past the target to improve the sensitivity to the lifetime. The distribution of decay points does not change significantly for lifetimes greater than 10 ns so we cannot place an upper limit on the lifetime of the 461-keV state. However, this data places a 1 σ lower limit of 9 ns which is consistent with the known lifetime of $\tau = 15.1(12)$ ns [40].

4.5 ^{32}Mg 0_2^+ Isomer

The CDM was also used to study the 0_2^+ isomer in ^{32}Mg at $E_x = 1058$ keV [13]. The only previous observation of this state suggested a long lifetime of $\tau > 10$ ps, making the CDM necessary to properly correct the Doppler-shift of in-flight decays.

4.5.1   Energy Measurement and Distribution of Decay Points

The ^{32}Mg result is shown in Fig. 4.23(b) where the CDM approach is used except now the 885-keV transition from the 2_1^+ state of ^{32}Mg is used as a reference to find the decay location. That is to say, for ^{32}Mg the 885-keV transition plays the role of γ_1 in Fig. 2.5, while the 172-keV transition is γ_2. Since the expected energy of the $0_2^+ \rightarrow 2_1^+$ transition (172 keV) is low, similar to the 240-keV transition of ^{31}Mg, the same condition was required that the gamma ray deposits its energy within $r = 20$ mm of the first interaction point. The upper spectrum of Fig. 4.23(b) shows a peak-like structure close to 170 keV corresponding to the $0_2^+ \rightarrow 2_1^+$ transition [13]. The background distribution is reproduced by analyzing the other reaction products of the ^{34}Si beam and scaling the result as shown with a solid black line. To understand the significance of the peak-like structure at 170 keV the measured spectrum was

compared to a simulation including the 0_2^+ isomer at 1058 keV and the cascade of gamma

rays with energies 172 and 885 keV. The 2_1^+ state was also included in the simulation using

the lifetime value $\tau = 16(3)$ ps determined from $B(E2)$ results [12, 35–39, 87]. The simulated

distribution was added to the background distribution and scaled to fit the peak at 170 keV

as shown by the red line.

The 170-keV peak was unambiguously confirmed by applying additional gates to the 885-

keV candidate. The result is shown in Fig. 4.23(b) as the lower, filled spectrum presenting

a clear signal with reduced background. In analogy with the $r = 20$-mm gate applied to the

170-keV transition in ^{32}Mg, a gate was applied for the 885-keV gamma ray that requires all

interaction points to lie within 60 mm of the first interaction point. Additionally, we used

the interaction point information of the detected 885-keV gamma ray to test if it is consistent

with Compton scattering. The energies of the first interaction and remaining interactions

were used in the Compton scattering formula to obtain the scattering angle (see Eq. (21) of

Ref. [99]). If this angle agreed within 0.7 rad with the scattering angle deduced from the decay

position and interaction position information, the event passed the gate. In this work the

$0_2^+ \to 2_1^+$ energy is 165$\pm$4(stat.)$\pm$2(syst.) keV which is included in the simulated response in

Fig. 4.23(b). The 7 keV difference between this measurement and the previous measurement

of 172(2) keV [13] is larger than the systematic uncertainty in this measurement due to both

the lifetime of the 2_1^+ state (3 ps uncertainty, corresponding to 0.6 keV uncertainty in energy)

and the decay location calculation (5 mm uncertainty, corresponding to 2 keV uncertainty

in energy). The apparent discrepancy between the observations may be due to the limited

statistics of the elusive 0_2^+ gamma-ray decay in both studies. For the rest of this work, the

weighted average of 170(2) keV for the energy of the $0_2^+ \to 2_1^+$ transition is adopted.

The distribution of the decays of the 0_2^+ state places an independent 1 σ lower limit on

the lifetime of $\tau > 8$ ns, confirming the isomeric nature of this state [13]. The upper limit could not be constrained, however, as shown in the inset of Fig. 4.23(b).

4.5.2 Constraints on the Cross Section and the 0_2^+ Lifetime

The correlation between the lifetime and partial cross section populating the 0_2^+ state (including feeding from unobserved higher-lying states) can be studied from the yield of the 170-keV peak, shown as a gray band in Fig. 4.24. Since the gamma-ray efficiency in this
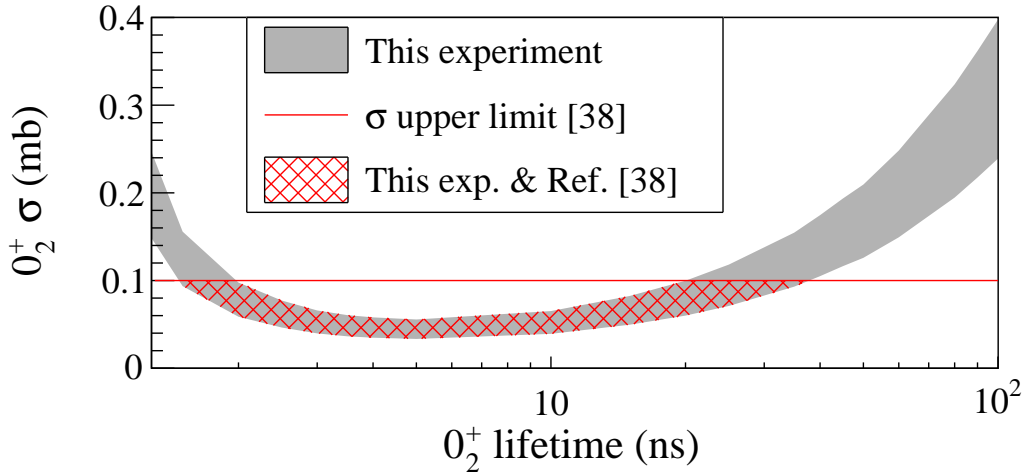
Figure 4.24: Possible values for partial cross section and lifetime of the 0_2^+ state of ^{32}Mg within 1 σ are plotted (gray band). From the work of Ref. [59], the cross section upper limit of 0.10 mb is included (red line), and the overlap of that work and this work is highlighted (red hatched region).

CDM measurement strongly depends on the lifetime, the possible cross section can be constrained for a given lifetime or vice versa. For example, if the assumed lifetime is 5 to 10 ns, the gamma-ray efficiency in this setup is maximized so the assumed cross section must be minimized. The total error in this result includes 20% statistical uncertainty in the yield of the 170-keV peak. Another important source of uncertainty is the efficiency of the gates. In order to keep this systematic uncertainty small, the spectrum including fewer gates (Fig. 4.23(b), upper spectrum) was used in this portion of the analysis and contributes 13%

relative uncertainty, estimated by applying the same gates to calibration data taken with a ^{152}Eu source. The statistical and systematic uncertainties were combined in quadrature to a total relative uncertainty of 25% in the cross section at any given lifetime.

The lifetime can be constrained by including the upper limit on the partial cross section of the 0_2^+ state from a previous two-proton removal reaction experiment [59], shown with a red horizontal line in Fig. 4.24. The previous and present removal reaction experiments populated states in ^{32}Mg using similar mid-target energies of 67 and 75 MeV/nucleon respectively. Eikonal model calculations [56] based on the USDB [100] two-nucleon amplitudes predict 5.11 and 5.23 mb for the inclusive cross section at 67 and 75 MeV/nucleon respectively, suggesting that the results of the previous removal experiment with a slightly different energy can be safely applied here. In the previous measurement, the 0_2^+ state was not observed but the 2_1^+ and 4_1^+ states were observed from their gamma-ray decays. The measured exclusive cross section populating the 2_1^+ and 4_1^+ states accounted for 100(12)% of the ^{32}Mg inclusive cross section, $\sigma_{inc} = 0.76(10)$ mb. This suggests that at most only 12% of the reactions populate the unobserved 0_2^+ state, corresponding to an upper limit of 0.10 mb for the partial cross section of the 0_2^+ state. With this upper limit in conjunction with the present result, the partial 0_2^+ cross section and lifetime are constrained to 0.03 mb $< \sigma <$ 0.10 mb and 1.5 ns $< \tau <$ 38 ns, respectively, as shown by the red hatched region in Fig. 4.24. The lifetime can be further constrained to 10 ns $< \tau <$ 38 ns from Ref. [13].

4.5.3 Independent Cross Section Measurement

The above assumption that the previously measured cross section at a slightly lower beam energy [59] is consistent with the cross section in this experiment is likely robust, however we do not need to rely on it entirely. The inclusive ^{32}Mg cross section and the exclusive

cross section to the short-lived states can be obtained from the data collected during the target-only setting of the TRIPLEX device. Then an upper limit on the exclusive cross section of the 0_2^+ state can again be found. The target-only setting had a mid-target energy of 57 MeV/nucleon, lower than the mid-target energy of 75 MeV/nucleon used for the CDM measurement. Nevertheless, the cross section measured using the TRIPLEX setup provides another result for comparison from a setup that shares many experimental properties.

The inclusive cross section of ^{32}Mg in the two-proton removal reaction from ^{34}Si is

$$\sigma_{inc} = \frac{N_{^{32}\text{Mg}}}{N_{^{34}\text{Si}} N_t} \tag{4.1}$$

where $N_{^{32}\text{Mg}}$ is the number of ^{32}Mg reaction products, $N_{^{34}\text{Si}}$ is the number of ^{34}Si beam ions, and N_t is the areal number density of ^{9}Be nuclei in the target. The exclusive cross to a particular state i of ^{32}Mg is

$$\sigma_{exc,i} = \frac{N_{^{32}\text{Mg},i}}{N_{^{34}\text{Si}} N_t}. \tag{4.2}$$

Also, it must be true that the sum of the exclusive cross section over all states of ^{32}Mg equals the inclusive cross section,

$$\sum_i \sigma_{exc,i} = \sigma_{inc}. \tag{4.3}$$

The inclusive and exclusive cross sections are calculated using the same beam $N_{^{34}\text{Si}}$ and the same target N_t, but the number of products, $N_{^{32}\text{Mg}}$ or $N_{^{32}\text{Mg},i}$, are obtained in different ways. $N_{^{32}\text{Mg}}$ is determined from the number of ^{32}Mg reaction products measured with the S800 focal plane detectors. $N_{^{32}\text{Mg},i}$, on the other hand, is based on the number of gamma rays from the decay of state i that are observed with GRETINA. The experimental setup designed for prompt decays is not sensitive to the exclusive cross section of the 0_1^+ or 0_2^+

states because these states do not promptly decay near GRETINA. However, the difference between the inclusive cross section and the sum of the observed exclusive cross sections to short-lived states, j, sets an upper limit on the exclusive cross section to the 0_2^+ state,

$$\sigma_{exc,0_2^+} < \sigma_{inc} - \sum_j \sigma_{exc,j}. \tag{4.4}$$

The number of incoming ^{34}Si beam nuclei, $N_{34_{Si}}$ can be determined from the total number of signals counted on the S800 OBJ scintillator upstream of the target position. This number reflects the number of secondary beam nuclei of all isotopes that impinge on the scintillator, including contaminants in the secondary beam. To find $N_{34_{Si}}$, we need to correct the number of signals on the object scintillator N_{obj} by the transmission of ^{34}Si ions from the scintillator to the target $t_{obt,t}$, and by the purity of the secondary beam at the object scintillator p_{obj}. Strictly speaking, $t_{obj,t}$ and p_{obj} cannot be measured directly in our setup. To measure $t_{obt,t}$ we would need the number of ^{34}Si at the object but we have the number of secondary beam ions of any species, including the contaminant secondary beams. To measure p_{obj} we need particle identification at the object, but we have this at the S800 focal plane which is not necessarily the same. However, the product $t_{obj,t} \times p_{obj}$ can be found from the unreacted beam setting for ^{34}Si using the number of ^{34}Si ions in the PID at the S800 focal plane divided by N_{obj}. This assumes that the transmission of ^{34}Si from the target to the S800 focal plane is 100%, which is safe to assume since there appears to be no acceptance loss in the ^{34}Si ion profile in Fig. 3.21. Altogether, the proportion of OBJ scintillator signals representing ^{34}Si that impinged on the target was 0.792(9). The observed number of beam nuclei must also be corrected for the efficiency of the object scintillator which was found to be 0.946(10)% for the runs when the S800 spectrograph was tuned to the ^{32}Mg reaction product. Ultimately,

the number of incident beam particles was $N_{34\text{Si}} = 5.91(15) \times 10^9$.

The areal number density of the target is found from the known thickness of the target by

$$N_t = \frac{t N_A}{m_a} \qquad (4.5)$$

where the thickness of the target is $t = 53(2)$ mg/cm^2, N_A is Avogadro's number, and the atomic mass of beryllium is $m_a = 9.012$ g. This results in an areal number density of $N_t = 3.54(13) \times 10^{21}$ cm^{-2} for the beryllium target nuclei. The target foil was manufactured by Goodfellow [101] and is reported to have a purity of greater than 99.8%. The effect of impurities in the target was neglected in this cross section calculation.

The number of ^{32}Mg reaction products is measured with the energy loss versus TOF PID spectrum at the S800 focal plane. Several corrections to the number of ^{32}Mg products must be taken into account as well. Signals from both of the CRDC's is required to obtain precise energy loss and TOF results. The combined efficiencies of the two S800 CRDC's is 0.968(14) for the ^{32}Mg fragment. The S800 data acquisition is triggered by signals from the E1 scintillator which experiences deadtime when the scintillator is not ready to receive the next signal. To estimate the deadtime, a 10 Hz clock is fed through the data acquisition system. The raw signal of the clock is recorded as well as the live signal of the clock that is only seen when the E1 scintillator is live and can receive a new event. The ratio of the live clock to the raw clock represents the proportion of the time that the E1 scintillator was alive, which was 0.93(3) for the setting accepting ^{32}Mg reaction products.

Not all ^{32}Mg reaction products are transmitted from the target to the S800 focal plane. This loss must be accounted for in the cross section measurement. Figure 4.25 shows the angle a_{fp} versus the position x_{fp} for ^{32}Mg ions that reached the S800 focal plane. Figure 4.25
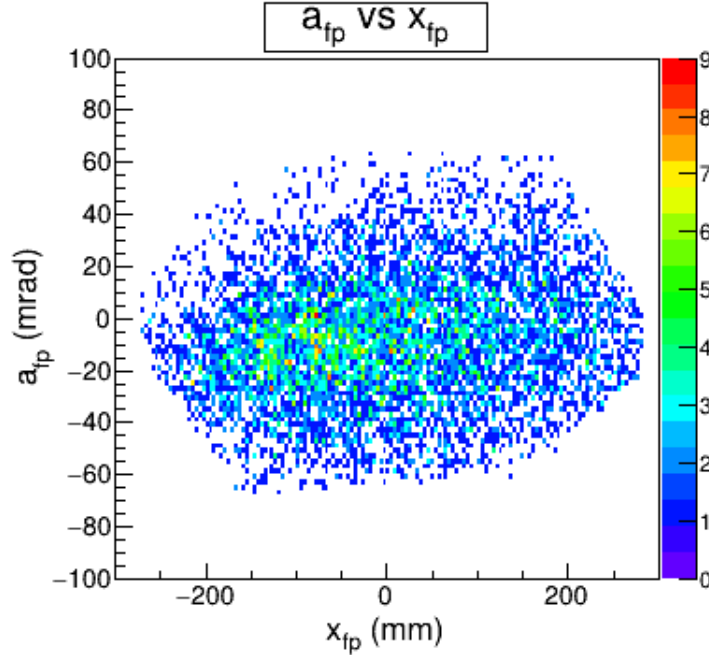
Figure 4.25: Distribution of the angle a_{fp} and the position x_{fp} for ^{32}Mg reaction products in the target-only setting with the TRIPLEX device. A portion of the ^{32}Mg reaction products are lost at the edges of the distribution with extreme values of both a_{fp} and x_{fp}.

shows sharp cutoffs at large a_{fp} and x_{fp} indicating the loss of ^{32}Mg ions that did not reach the focal plane. For ions with x_{fp} near the center of the focal plane, all angles a_{fp} are accepted. A region at the center of x_{fp} was selected and fit with a Gaussian function,

$$\text{counts}(a) = A e^{-(a-\mu)^2/(2\sigma^2)}. \tag{4.6}$$

Using the center μ and width σ of the Gaussian function for the central region as fixed parameters, the height A of the function was fit to regions of x_{fp} away from the center. A distribution of a_{fp} for ^{32}Mg reaction products for different selections of x_{fp} are shown in Fig. 4.26. For the non-central x_{fp} regions, there is a gap between the data and the Gaussian function at the edges of the a_{fp} distributions. The size of these gaps were quantified and associated with loss of angular acceptance of the S800. These steps were repeated with

126
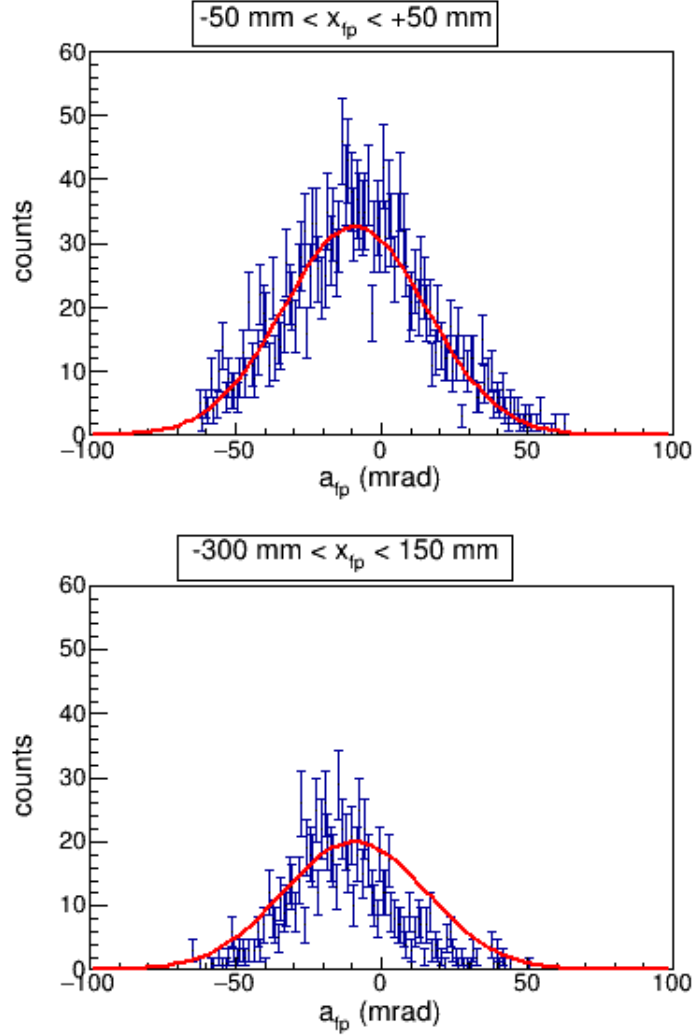
Figure 4.26: Distribution of the angle a_{fp} for ^{32}Mg reaction products in the target-only setting with different x_{fp} ranges. In the top spectrum, central values are chosen (-50 mm $< x_{fp} < 50$ mm) for which all angles a_{fp} are accepted by the S800 spectrograph. A solid red line represents a Gaussian fit to the distribution with the height A, mean μ, and width σ as free parameters. The bottom spectrum shows the a_{fp} distribution for for non-central position (-300 mm $< x_{fp} < -150$ mm). The red solid line in the bottom spectrum represents a Gaussian fit with only the height A as a free parameter and the mean μ and width σ fixed to the values obtained from the fit to the distribution in the top spectrum. The gap between the solid red line and the data in the bottom spectrum represents the reaction products that were lost due to limited a_{fp} acceptance of the S800 for this range of x_{fp} values.

different sizes of the central x_{fp} region that was assumed to accept all a_{fp} angles. Using the

different central regions, consistent results were found and the average value for the S800

angular acceptance was 89(2)%.

Beside the loss due to a_{fp} angular acceptance, there is also loss from the momentum acceptance of the S800 spectrograph. The momentum acceptance is correlated with the angle a_{fp} of the ion, in a similar way to how x_{fp} acceptance is correlated with a_{fp}. Fig 4.27 shows the momenta of ^{32}Mg ions detected by the S800, corrected by the angular acceptance. The
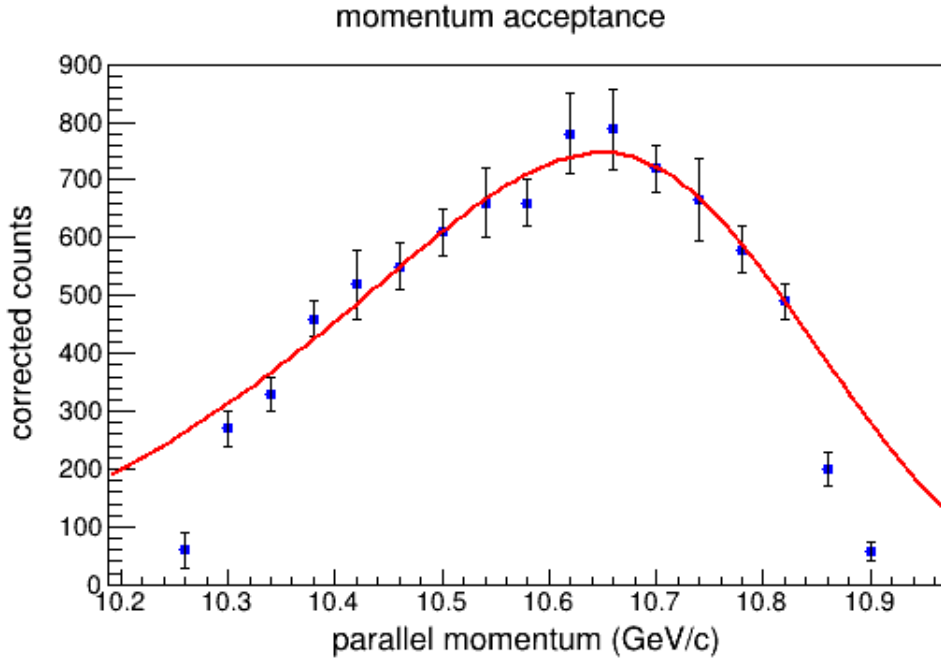
Figure 4.27: The parallel-momentum distribution of ^{32}Mg reaction products in the target-only setting. The counts are corrected for the loss of angular acceptance which occurs mostly at small and large momenta. The solid red line depicts a skew-Gaussian fit [102] to the data from 10.32 to 10.84 GeV/c. The difference between the fit and the data at the edges of the momentum distribution represents the loss of ^{32}Mg reaction products due to the finite momentum acceptance of the S800 spectrograph.

momentum distribution shows a sharp drop at the edges of the acceptance. A skew-Gaussian function [102] was fit to the distribution to estimate the amount of ^{32}Mg that was produced in the reaction but not observed due to limited momentum acceptance. The momentum acceptance for ^{32}Mg ions was determined to be 81(5)%. Considering the momentum acceptance, angular acceptance, the detection efficiency and deadtime, the total number of ^{32}Mg produced in these reactions was $N_{^{32}\mathrm{Mg}} = 1.39(12) \times 10^4$.

The number of reaction products that populate an excited state $N_{^{32}\text{Mg},i}$ is found from the number of observed gamma rays emitted from the decay of state i. To find the exclusive cross section of state i, the gamma rays emitted from the decay of state i must be quantified, and the number of gamma rays feeding state i must be measured as well. Where the feeding of state i is not known, only an upper limit on the exclusive cross section can be obtained.

The inclusive cross section of ^{32}Mg and the exclusive cross sections to the observed excited states are listed in Table 4.2. The cross sections are compared with the values obtained from

state	σ_{exp}	σ_{prev}
^{32}Mg (inc.)	0.65(7)	0.76(10)
2_1^+	0.34(7)	0.52(8)
4_1^+	0.18(3)	0.24(8)
0_2^+	< 0.22	< 0.10

Table 4.2: Two-proton removal cross sections in the $^9\text{Be}(^{34}\text{Si},^{32}\text{Mg})\text{X}$ reaction. The column labeled σ_{prev} shows the results of the work from Ref. [59]. The upper limit for the exclusive cross section of the 0_2^+ state is based on the unobserved gamma-ray intensity as described in the main text.

the past experiment using the same reaction mechanism [59]. The work in Ref. [59] only observed the 2_1^+ and 4_1^+ states in ^{32}Mg and notes that they observe an excess of gamma-ray energies above 1.4 MeV suggesting the existence of undetermined higher-lying states. To make a comparison between the present cross section results and the results from Ref. [59], the exclusive cross sections for the 2_1^+ and 4_1^+ states in this experiment are found from the gamma-ray intensities assuming no higher-lying states were populated. Table 4.2 reports the cross section results with 1σ error bars and in most cases the present results agree with the results from Ref. [59] within the 1σ range. The exclusive cross section of the 2_1^+ is slightly lower in the present measurement than it is in Ref. [59] when including the error. Due to the near agreement between the cross sections measured in the present target-only setting

and the values from Ref. [59], it is likely safe to apply the cross sections from Ref. [59] to the analysis of the data from the upstream experimental setting at 80 MeV/nucleon, as was done in Section 4.5.2.

Chapter 5

Discussion of Results

The new lifetime results for excited states in ^{32}Mg can give us a new understanding of the structure of this isotope. The reduced $E2$ transition rates, $B(E2)$, can be found from these lifetimes. The $B(E2)$ describes the interaction between the two associated states and can be a powerful probe of collective behavior.

5.1 $B(E2)$ Values in ^{32}Mg and Even-even Mg Isotopes

The 2_1^+ state in ^{32}Mg has been studied numerous times. As a result there are many experimental results for the $B(E2; 2_1^+ \rightarrow 0_1^+)$ value as shown in Fig. 5.1. The lifetime measurement from the present experiment is $\tau(2_1^+) = 18.7 \pm 1.2(\text{stat.}) \pm 1.1(\text{syst.})$ ps and results in $B(E2; 2_1^+ \rightarrow 0_1^+) = 80(7)\ e^2\text{fm}^4$, which has the least error of any of the reported $B(E2)$ results. The present $B(E2)$ value from a lifetime measurement accounts for feeding from higher-lying states including the 4_1^+ state at $E_x = 2332$ keV. The $B(E2)$ value from the present experiment is slightly lower but in good agreement with the weighted average of the previous results $B(E2; 2_1^+ \rightarrow 0_1^+) = 90\ e^2\text{fm}^4$ [87].

To interpret the meaning of this $B(E2; 2_1^+ \rightarrow 0_1^+)$ value, it is compared with theoretical predictions for ^{32}Mg and for other even-even Mg isotopes [95, 103–105] in Fig. 5.2. The USDA calculation is a shell model calculation that limits the valence orbits to the sd-shell for both protons and neutrons [106]. The sd-shell orbitals are sufficient for describing many
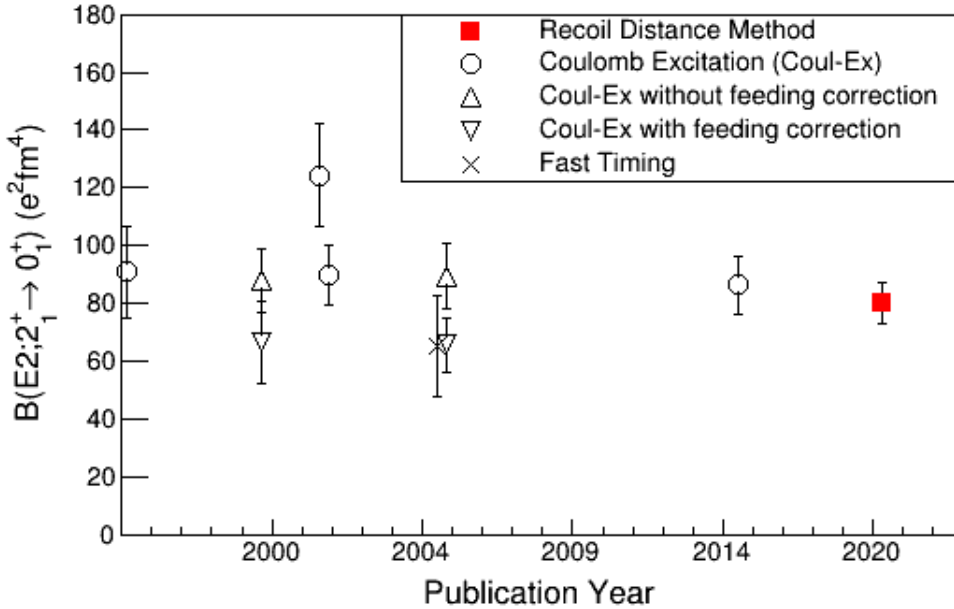
Figure 5.1: The $B(E2; 2_1^+ \rightarrow 0_1^+)$ value in ^{32}Mg reported in experiments over the past 25 years. The present RDM measurement is shown with a red square. The Coulomb-excitation measurements from Refs. [12,36,37,39] are shown with open circles. The open triangles are the results from Refs. [35,38]. The upward-pointing triangles reflect the $B(E2)$ values without feeding corrections while the corresponding downward-pointing triangles take into account feeding corrections. The saltire symbol ($\times$) represents the fast timing measurement of Ref. [40].

nuclei with 8 to 20 of each nucleon since the valence particles will typically occupy the sd-shell. However, for the members of the $N = 20$ island of inversion such as ^{32}Mg, it is understood that intruder configurations of neutrons occupying the $0f_{7/2}$ and $1p_{3/2}$ orbitals dominate the low-energy states [10, 17]. As a result, the USDA calculation underestimates the observed $B(E2)$ strength in ^{32}Mg.

It is important to include the $0f_{7/2}$ and $1p_{3/2}$ orbitals in an effective shell-model description of ^{32}Mg. The SDPF-M [31] and SDPF-U-MIX [20] interactions both include these intruder orbitals. Both the SDPF-M and SDPF-U-MIX implement the USD interaction [106] for the sd-shell and base the pf-shell portion on the KB interaction [107]. They can express
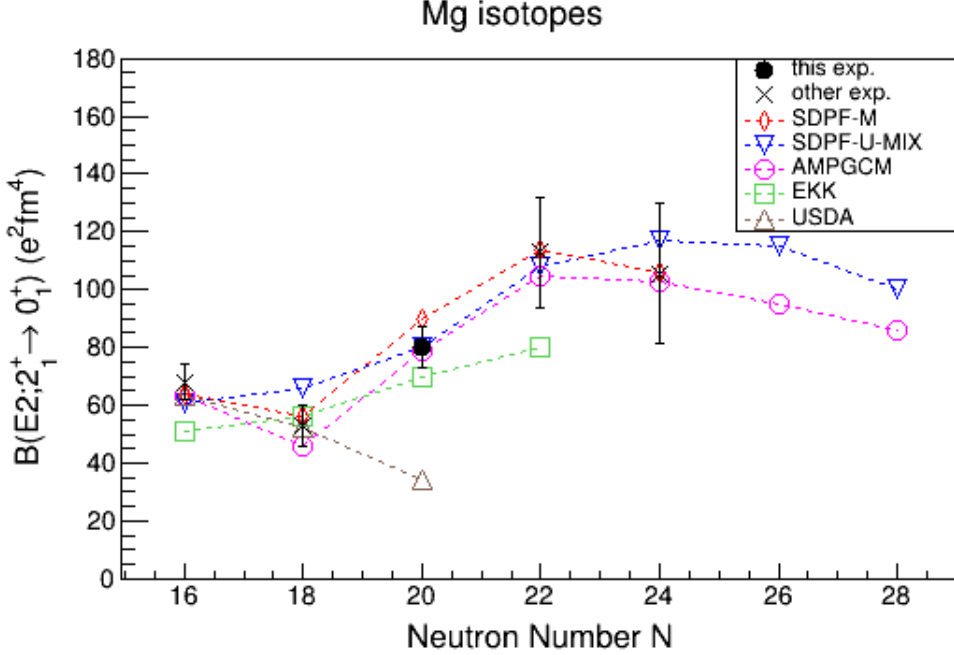
Figure 5.2: The $B(E2; 2_1^+ \rightarrow 0_1^+)$ values in the Mg isotopic chain from ^{28}Mg to ^{40}Mg. The ^{32}Mg result from this experiment is shown with a filled black circle. The experimental values from other results are shown with black saltires ($\times$) and are from Refs. [103,95,104,105]. Theoretical calculations are also shown for SDPF-M [31] (red line and open diamonds), SDPF-U-MIX [20] (blue line and open inverted triangles), AMPGCM [33,34] (purple line and open circles), EKK [21] (green line and open squares), and USDA [106] (brown line and open triangles).

both normal configurations, with neutrons occupying the sd-shell, and intruder configurations with neutrons in the pf-shell, and allow mixing of among these configurations. These calculations are more successful than the USDA calculation at reproducing the increase in $B(E2)$ that occurs from ^{30}Mg to ^{32}Mg.

The angular-momentum-projected generator coordinate method (AMPGCM) [33, 34] result is based on a mean-field calculation using the Gogny interaction [108]. The AMPGCM identifies different deformed minima for the states in ^{32}Mg and mixes these configurations. The mixed configurations were used to obtain the $B(E2)$ results shown in Fig. 5.2. Ref. [34] suggests that the 0_1^+ state in ^{32}Mg contains significant mixing of both oblate and prolate

133

configurations.

The most recent calculation shown in Fig. 5.2 is the extended Kuo-Krenciglowa (EKK) method [21], based on the Kuo-Klenciglowa (KK) method [109–111]. The EKK method uses a shell model interaction that, unlike the previous interactions, does not require empirically fitting the parameters of the interaction to reproduce any observables. This places the EKK results in close connection with microscopic theories such as quantum chromodynamics. While the EKK calculation underpredicts the $B(E2)$ value for ^{32}Mg, it does reproduce the general trend of increasing $B(E2)$ as the isotopic chain becomes more neutron-rich beyond ^{30}Mg.

For ^{32}Mg, the present result for the $B(E2; 2_1^+ \rightarrow 0_1^+)$ value is best reproduced by the SDPF-U-MIX and AMPGCM calculations. All the theories depicted in Fig. 5.2 that include configuration-mixing with pf-shell orbitals reproduce the increase in $B(E2; 2_1^+ \rightarrow 0_1^+)$ which is a signature of this island of inversion. Predictions differ on whether the $B(E2; 2_1^+ \rightarrow 0_1^+)$ value is maximized at ^{34}Mg or ^{36}Mg, and the experimental results for ^{34}Mg and ^{36}Mg are nearly the same. A reduction of the uncertainty for the $B(E2; 2_1^+ \rightarrow 0_1^+)$ value for ^{34}Mg and ^{36}Mg would shed light on the evolution of collectivity through the Mg isotopes. The investigation of $B(E2)$ values in Mg ultimately leads to the intriguing case of ^{40}Mg at $N = 28$ where the collapse of yet another magic number may play a significant role [112]. These $B(E2)$ values can inform the idea that the $N = 20$ and $N = 28$ islands of inversion merge into a continuous region of inversion along the Mg isotopes according to the SDPF-U-MIX calculation [20].

5.2 The ^{32}Mg 4_1^+ State

This dissertation reported the first lifetime measurement of the 4_1^+ state of ^{32}Mg as $\tau(4_1^+) = 0.9\pm0.2(\text{stat.})\pm0.1(\text{syst.})$ ps. The corresponding large value of $B(E2; 4_1^+ \to 2_1^+) = 150(30)$ e^{2}fm^4 is a signature of the collectivity of this transition. This underscores the breaking of the $N = 20$ magic number to allow the coherent mixing of many configurations into a collective state. The spin-parity assignment of the 4_1^+ state was previously established through a proton-scattering experiment [43]. The $B(E2; 4_1^+ \to 2_1^+)$ result from the present work is consistent with the 4^+ assignment and the interpretation of this band as rotational collectivity.

The ratio of $B(E2)$ values for the $4_1^+ \to 2_1^+$ and $2_1^+ \to 0_1^+$ transitions can now be reported for the first time with the present lifetime measurement of the 4_1^+ state. The $B(E2)$ ratio is a tool often used to characterize many different band structures. It is complementary to the ratio of the excited energies of the 4_1^+ and 2_1^+ states. The energy and $B(E2)$ ratios for ^{32}Mg are shown in Table 5.1 along with the predicted values for different archetypes of collective behavior. Both the energy and the $B(E2)$ ratio indicate that the ground-state band exhibits

ratio	data	vibrator	symmetric rotor	EKK [21]
$E(4_1^+)/E(2_1^+)$	2.62	2	3.33	2.55
$\dfrac{B(E2;4_1^+\to2_1^+)}{B(E2;2_1^+\to0_1^+)}$	1.9(4)	2	1.43	1.37

Table 5.1: Energy ratio and $B(E2)$ ratio observed for ^{32}Mg and from several predictions. The EKK predictions are from Ref. [21].

collective behavior. The $B(E2)$ ratio has large uncertainty which comes mostly from the 4_1^+ lifetime measurement so it is not useful here to characterize the nature of the ground-state band further. The short lifetime of the 4_1^+ state is near the limit of sensitivity for the

present experimental setup. A dedicated DSAM measurement at a lower beam energy would likely be able to measure the 4_1^+ lifetime with less uncertainty. As shown in Fig. 2.2 DSAM experiments are often able to measure lifetimes as short as 10 fs.

5.3 The ^{32}Mg 0_2^+ State

Using the 0_2^+ lifetime result of 10 ns $< \tau <$ 38 ns and the weighted average energy of the $0_2^+ \rightarrow 2_1^+$ transition of 170(2) keV, the reduced $E2$ transition probability is 28 e^{2}fm^4 $<$ $B(E2; 2_1^+ \rightarrow 0_2^+) <$ 122 e^{2}fm^4. For physically reasonable values of $\rho^2(E0)$ the $E0$ branch is expected to be less than 1% [13, 113] therefore the $0_2^+ \rightarrow 0_1^+$ transition is assumed to be negligible. Table 5.2 summarizes the reduced $E2$ transition rates to 0^+ states in ^{32}Mg and neighboring even-even nuclei which can characterize the quadrupole collectivity in these transitions. For ^{30}Mg, a strong $B(E2)$ is observed for the $2_1^+ \rightarrow 0_1^+$ transition [31, 115],

$B(E2)$ (e^{2}fm^4)	^{30}Mg	^{34}Si	^{32}Mg [1]
$2_1^+ \rightarrow 0_1^+$	53(7) [95]	17(7) [114]	80(7)
$2_1^+ \rightarrow 0_2^+$	10.9(12) [95]	61(40) [60]	48^{+74}_{-20}

Table 5.2: $B(E2)$ values in ^{32}Mg and neighboring even-even isotopes.

whereas in ^{34}Si a strong $B(E2)$ appears for the $2_1^+ \rightarrow 0_2^+$ transition since both the 0_2^+ and 2_1^+ states are considered to be dominated by the collective 2p2h configurations [60]. The present data for ^{32}Mg indicate that the 0_2^+ state is as collective as the 0_1^+ state in contrast with the sizeable difference in transition probabilities between 0^+ states in both ^{30}Mg and ^{34}Si. Notably, the $B(E2; 2_1^+ \rightarrow 0_2^+)$ value in ^{32}Mg is comparable to the strong transitions in ^{30}Mg and ^{34}Si. Indeed, the present result shows $E2$ strength that far exceeds the value

---

[1]central value of $B(E2; 2_1^+ \rightarrow 0_2^+) = 48$ e^{2}fm^4 corresponds to the central lifetime value of 24 ns

calculated by the SDPF-U-MIX model [60] which predicts $B(E2; 2_1^+ \rightarrow 0_2^+) = 15 \ e^2 \text{fm}^4$. The large collectivity in the 0_2^+ state of ^{32}Mg indicates prominent intruder contributions to the state. However, given the large experimental uncertainties, the current $B(E2; 2_1^+ \rightarrow 0_2^+)$ result does not allow for a stringent conclusion.

5.4 Cross Section to ^{32}Mg 0^+ States

Additional direct information about the intruder contributions can be obtained from the partial cross section to populate the 0_2^+ state in comparison with theoretical calculations assuming a pure 0p0h configuration. The ^{34}Si 0_1^+ state is predominantly of 0p0h configuration [20, 31] and the two-proton removal reaction cross section is sensitive to the wavefunction overlap between the incoming projectile and outgoing residual nucleus final state, allowing the 0p0h occupancy in the 0_2^+ state of ^{32}Mg to be quantified. Reaction calculations were performed following the method of Ref. [56] which applies the two-neutron amplitudes (TNA) from shell-model calculations combined with eikonal, direct reaction theory. The suppression factor R_{2n}, the ratio of experimental to calculated inclusive two-nucleon removal cross sections, is not well-known for the $(^{34}\text{Si},^{32}\text{Mg})$ reaction. We use the value $R_{2n} = 0.5$ seen for a number of less-exotic sd-shell nuclei [56]. Assuming the essentially pure 0p0h ^{32}Mg ground state calculated with the USDB interaction [100] is the ^{32}Mg 0_2^+ state, the 0_2^+ cross section is $\sigma_{2n} = 0.42$ mb. This value is significantly larger than the experimental upper limit of 0.10 mb indicating the physical 0_2^+ state has a reduced 0p0h occupancy. The 3-level mixing model of Ref. [45] predicts a smaller 0p0h occupancy with a probability $\alpha^2 = 0.15$ for the 0_2^+ state due to the sizeable 2p2h and 4p4h contributions to this state which reduces the overlap with the ^{34}Si 0_1^+ state. By scaling the cross section obtained from the USDB

pure 0p0h calculation with the 0p0h probability α^2 of the 0_2^+ state, the 3-level mixing model results in a cross section of 0.06 mb. This result is consistent with the measured partial cross section, strongly suggesting that the 0_2^+ state contains strong admixtures of the 2p2h and 4p4h intruder configurations.

The present result raises the question, "Where does the 0p0h-dominant 0^+ state exist in ^{32}Mg, if anywhere?" The 3-level mixing model [45] predicts the 0_3^+ state at 2.22 MeV with the 0p0h probability $\alpha^2 = 0.81$. This gives the partial cross section $\sigma_{2n} = 0.34$ mb for the 0_3^+ state, although associated events have not been experimentally observed. Using the USDB calculations the partial cross sections for the individual states are $\sigma(0^+) = 0.42$ mb, $\sigma(2^+) = 0.94$ mb and $\sigma(4^+) = 1.26$ mb for $R_{2n} = 0.50$. The resulting inclusive cross section of 2.62 mb is much larger than the experimental value of 0.76(10) mb [59] as is the case for more exotic nuclei in this mass region [116, 117]. This discrepancy indicates either that the R_{2n} is strongly quenched in the $(^{34}$Si,^{32}Mg) reaction where the structure is thought to change drastically between the two nuclei or that the 0p0h components in ^{32}Mg are widely spread or even fragmented above the neutron separation energy ($S_n = 5.778$ MeV), calling for future investigation.

138

Chapter 6

Concluding Remarks

The nature of ^{32}Mg is an intriguing topic due to the significant admixture of the normal 0p0h configuration and the intruder 2p2h and 4p4g configurations [45]. For instance, within a single band of ^{32}Mg complex changes in the admixture of the intruder configurations may take place as the nucleus increases in spin [44]. The complications in ^{32}Mg may signal similar effects in other island of inversion nuclei or neutron-rich regions.

This work has shown through the precise $B(E2; 2_1^+ \rightarrow 0_1^+)$ result that the collectivity in the ground-state band is slightly lower than previously thought. In the light of this evidence for strong collectivity in the 0_2^+ state, a new picture of ^{32}Mg begins to emerge. Apparently, this collectivity once thought to dominate only the ground-state band is actually well-mixed with the band beginning with the 0_2^+ state, which is more collective than once believed.

The available data suggests significant collectivity in both the 0_1^+ and 0_2^+ states of ^{32}Mg. The normal configuration is associated with spherical shapes in the $N = 20$ isotones and hence hinders collectivity. It seems likely that the 2p2h and 4p4h configurations are both significant components of the 0_1^+ and 0_2^+ states of ^{32}Mg given the low cross section observed for these states in the ^{9}Be(^{34}Si,^{32}Mg)X reaction. The SDPF-U-MIX calculation shown in Ref. [44] indicates that the band built upon the 0_1^+ state becomes more dominated by 4p4h than 2p2h configurations as spin increases. The 0_2^+ state could be the beginning of a band that begins with nearly equal components of 2p2h and 4p4h configurations but then evolves

with increasing spin to have more 2p2h component. Of course, it is possible for band above the 0_2^+ state to become dominated by 0p0h configurations at higher spin. This is reminiscent of the original observation of the 0_2^+ state which suggested the 0_2^+ state is based on an almost pure sd configuration [13]. Experimental data on the hypothetical 2^+ and 4^+ members of the band built upon the 0_2^+ may provide crucial data on the configuration-mixing therein. For now however one must rely on shell-model calculations or other theoretical approaches.

As mentioned earlier, the branching ratio of the $0_2^+ \rightarrow 0_1^+$ $E0$ transition in ^{32}Mg is expected to be less than 1% [13, 113]. The observation of this $E0$ transition rate would be valuable to help understand the similarities or differences in the wave functions of the 0_1^+ and 0_2^+ states (see, for instance, Ref. [118]).

In conclusion, the lifetimes of excited states in ^{32}Mg have been studied with established experimental techniques as well as the novel Cascade Doppler-shift Method for the study of in-flight-decaying isomers. The 2_1^+ state lifetime $\tau(2_1^+) = 18.7(12stat.)(13syst.)$ ps indicates the collectivity of the ground-state band and provides a resolution to the discrepancy between previous experimental observations. The lifetime of the 4_1^+ state $\tau(4_1^+) = 0.9(2)$ ps is the first measurement for this state and confirms the spin-parity assignment of 4^+ and reinforces the interpretation of the ground-state band as a collective structure along the traditional $N = 20$ magic number. The new CDM method to study isomeric states decaying in-flight was used to observe the $0_2^+ \rightarrow 2_1^+$ transition at 170(2) keV in ^{32}Mg and constrain the lifetime of the 0_2^+ state. The $B(E2; 2_1^+ \rightarrow 0_{1,2}^+)$ values of ^{32}Mg reveal that the 0_2^+ state is as collective as the 0_1^+ state which is an unexpected feature not yet observed in neighboring isotopes or in available theoretical calculations. From the constrained reaction cross section it is implied that the 0p0h amplitude in the 0_2^+ state is much reduced by the presence of intruder configurations. The novel technique introduced here proved indispensable to observe the 0_2^+ state and, as

rare-isotope beams with high velocities continue to be powerful tools, this method will prove

vital to extend the sensitive lifetime range of in-beam experiments.

BIBLIOGRAPHY

[1] National Nuclear Data Center `www.nndc.bnl.gov`.

[2] B. A. Brown, Lecture Notes on Nuclear Structure (2017).

[3] R. F. Casten, *Nuclear Structure from a Simple Perspective*, 2nd ed. (Oxford University Press, 2000).

[4] R. D. Woods and D. S. Saxon, Phys. Rev. **95**, 577 (1954).

[5] M. G. Mayer, Phys. Rev. **75**, 1969 (1949).

[6] O. Haxel, J. H. D. Jensen, and H. E. Suess, Phys. Rev **75**, 1766 (1949).

[7] V. F. Weisskopf, Phys. Rev. **83**, 1073 (1951).

[8] B. Pritychenko, M. Mirch, B. Singh, and M. Horoi, Atomic Data and Nuclear Data Tables **107** (2016).

[9] M. G. Mayer, Phys. Rev **74**, 235 (1948).

[10] O. Sorlin and M.-G. Porquet, Prog. Part. Nucl. Phys. **61**, 602 (2008).

[11] A. Navin, D. W. Anthony, T. Aumann, T. Baumann, D. Bazin, Y. Blumenfeld, B. A. Brown, T. Glasmacher, P. G. Hansen, R. W. Ibbotson, P. A. Lofy, V. Maddalena, K. Miller, T. Nakamura, B. V. Pritychenko, B. M. Sherrill, E. Spears, M. Steiner, J. A. Tostevin, J. Yurkon, and A. Wagner, Phys. Rev. Lett. **86**, 266 (2000).

[12] T. Motobayashi, Y. Ikeda, Y. Ando, K. Ieki, M. Inoue, N. Iwasa, T. Kikuchi, M. Kurokawa, S. Moriya, S. Ogawa, H. Murakami, S. Shimoura, Y. Tanagisawa, T. Nakamura, Y. Watanabe, M. Ishihara, T. Teranishi, H. Okuno, and R. F. Casten, Phys. Lett. B **346**, 9 (1995).

[13] K. Wimmer, T. Kröll, R. Krücken, V. Bildstein, R. Gernhäuser, B. Bastin, N. Bree, J. Diriken, P. V. Duppen, M. Huuyse, N. Patronis, P. Vermaelen, D. Voulot, J. V. de Walle, F. Wenander, L. M. Fraile, R. Chapman, B. Hadinia, R. Orlandi, J. F. Smith, R. Lutter, P. G. Thirolf, M. Labiche, A. Blazhev, M. Kalkúhler, P. Reiter, M. Seidlitz, N. Warr, A. O. Macchiavelli, H. B. Jeppesen, E. Fiori, G. Gerigiev, G. Schirieder, S. D. Gupta, G. L. Bianco, S. Nardelli, J. Butterworth, J. Johansen, and K. Riisager, Phys. Rev. Lett. **105** (2010).

[14] C. Détraz, D. Guillemaud, G. Huber, R. Klapisch, M. Langevin, F. Naulin, C. Thibault, and L. Carraz, Phys. Rev. C **19** (1979).

[15] B. Bastin, S. Grévy, D. Sohler, O. Sorlin, Z. Dombrádi, N. L. Achouri, J. C. Angélique, F. Azaiez, D. Baiborodin, R. Borcea, C. Bourgeois, A. Buta, A. Bürger, R. Chapman, J. C. Dalouzy, Z. Dlouhy, A. Drouard, Z. Elekes, S. Franchoo, S. Iacob, B. Laurent, M. Lazar, X. Liang, E. Liénard, J. Mrazek, L. Nalpas, F. Negoita, N. A. Orr, Y. Penionzhkevich, Z. Podolyák, F. Pougheon, P. Roussel-Chomaz, M. G. Saint-Laurent, M. Stanoiu, I. Stefan, F. Nowacki, and A. Poves, Phys. Rev. Lett. **99** (2007).

[16] A. Gade, R. V. F. Janssens, T. Baugher, D. Bazin, B. A. Brown, M. P. Carpenter, C. J. Chiara, A. N. Deacon, S. J. Freeman, G. F. Grinyer, C. R. Hoffman, B. P. Kay, F. G. Kondev, T. Lauritsen, S. McDaniel, K. Meierbachtol, A. Ratkiewicz, S. R. Stroberg, K. A. Walsh, D. Weisshaar, R. Winkler, and S. Zhu, Phys. Rev. C **81**, 051304(R) (2010).

[17] B. A. Brown, Physics **3** (2010).

[18] S. M. Lenzi, F. Nowacki, A. Poves, and K. Sieja, Phys. Rev. C **82** (2010).

[19] F. Nowacki, A. Poves, E. Caurier, and B. Bounthong, Phys. Rev. Lett. **117** (2016).

[20] E. Caurier, F. Nowacki, and A. Poves, Phys. Rev. C **90** (2014).

[21] N. Tsunoda, T. Otsuka, N. Shimizu, M. Hjorth-Jensen, K. Takayanagi, and T. Suzuki, Phys. Rev. C **95** (2017).

[22] T. Otsuka, T. Suzuki, J. D. Holt, A. Schwenk, and Y. Akaishi, Phys. Rev. Lett. **105** (2010).

[23] C. Thibault, R. Klapisch, C. Rigaud, A. M. Poskanzer, R. Prieels, L. Lessard, and W. Reisdorf, Phys. Rev. C **12** (1975).

[24] E. K. Warburton, J. A. Becker, and B. A. Brown, Phys. Rev. C **41**, 1147 (1990).

[25] B. H. Wildenthal and W. Chung, Phys. Rev. C **22**, 2260 (1980).

[26] C. Détraz, M. Langevin, M. C. Goffri-Kouassi, D. Guillemaud, M. Epherre, G. Audi, C. Thibault, and F. Touchard, Nucl. Phys. A **394**, 378 (1983).

[27] X. Campi, H. Flocard, A. Kerman, and S.Koonin, Nucl. Phys. A **251**, 193 (1975).

[28] A. Poves and J. Retamosa, Phys. Lett. B **184**, 311 (1987).

[29] A. Poves and J. Retamosa, Nucl. Phys. B **571**, 221 (1994).

[30] N. Fukunishi, T. Otsuka, and T. Sebe, Phys. Lett. B **296**, 279 (1992).

[31] Y. Utsuno, T. Otsuka, T. Mizusaki, and M. Honma, Phys. Rev. C **60** (1999).

[32] A. Poves, E. Caurier, F. Nowacki, and K. Sieja, Phys. Scr. **T150** (2012).

[33] A. Rodríguez-Guzmán, J. L. Egido, and L. M. Robledo, Phys. Rev. C **62** (2000).

[34] A. Rodríguez-Guzmán, J. L. Egido, and L. M. Robledo, Nucl. Phys. A **709**, 201 (2002).

[35] B. V. Pritychenko, T. Glasmacher, P. D. Cottle, M. Fauerback, R. W. Ibbotson, K. W. Kemper, V. Maddalena, A. Navin, R. Ronningen, A. Sakharuk, H. Scheit, and V. G. Zelevinsky, Phys. Lett. B **461**, 322 (1999).

[36] V. Chisté, A. Gillibert, A. Leépine-Szily, N. Alamanos, F. Auger, J. Barrette, F. Braga, M. D. Cortina-Gil, Z. Dlouhy, V. Lapoux, M. Lewitowicz, R. Lichtenthäler, R. L. Neto, S. M. Lukyanov, M. MacCormick, F. Marie, W. Mittig, F. de Oliveira Santos, N. A. Orr, A. N. Ostrowski, S. Ottini, A. Pakou, Y. E. Penionzhkevich, P. Roussel-Chomaz, and J. L. Sida, Phys. Lett. B **514**, 233 (2001).

[37] H. Iwasaki, T. Motobayashi, H. Sakurai, K. Yoneda, T. Gomi, N. Aoi, N. Fukuda, Z. Fülöp, U. Futakami, Z. Gacsi, Y. Higurashi, N. Imai, N. Iwasa, T. Kubo, M. Kunibu, M. Kurokawa, Z. Liu, T. Minemura, A. Saito, M. Serata, S. Shimoura, S. Takeuchi, Y. X. Watanabe, K. Yamada, Y. Yanagisawa, and M. Ishihara, Phys. Lett. B **522**, 227 (2001).

[38] J. A. Church, C. M. Campbell, D.-C. Dinca, J. Enders, A. Gade, T. Glasmacher, Z. Hu, R. V. F. Janssens, W. F. Mueller, H. Olliver, B. C. Perry, L. A. Riley, and K. L. Yurkewicz, Phys. Rev. C **72** (2005).

[39] K. Li, Y. Ye, T. Motobayashi, H. Scheit, P. Doornenbal, S. Takeuchi, N. Aoi, M. Matsushita, E. Takeshita, D. Pang, and H. Sakurai, Phys. Rev. C **92** (2015).

[40] H. Mach, L. M. Fraile, O. Tengblad, R. Boutami, C. Jollet, W. A. Plóciennik, D. T. Yordanov, M. Stanoiu, M. J. G. Borge, P. A. Butler, J. Cedarkäll, P. Fogelberg, H. Fynbo, P. Hoff, A. Jokinen, A. Korgul, U. Köster, W. Kurcewicz, F. Marechal, T. Motobayashi, J. Mrazek, G. Neyens, T. Nilsson, S. Pedersen, A. Poves, B. Rubio, E. Ruchowska, and the ISOLDE Collaboration, Eur. Phys. J. A **s01**, 105 (2005).

[41] D. Guillemaud-Mueller, C. Détraz, M. Langevin, F. Naulin, M. de Saint-Simon, C. Thibault, and F. Touchard, Nucl. Phys. A **426**, 37 (1984).

[42] G. Klotz, P. Baumann, M. Bounajma, A. Huck, A. Knipper, G. Walter, G. Marguier, C. Richard-serre, A. Poves, and J. Retamosa, Phys. Rev. C **47**, 2502 (1993).

[43] S. Takeuchi, N. Aoi, T. Motobayashi, S. Ota, E. Takeshita, H. Suzuki, H. Baba, T. Fukui, Y. Hashimoto, K. Ieki, N. Imai, H. Iwasaki, S. Kanno, Y. Kondo, T. Kubo, K. Kurita, T. Minemura, T. Nakabayashi, T. Nakamura, T. Okumura, T. K. Onishi, H. Sakurai, S. Shimoura, R. Sugou, D. Suzuki, M. K. Suzuki, M. Takashina, M. Tamaki, K. Tanaka, Y. Togano, and K. Yamada, Phys. Rev. C **79** (2009).

[44] K. L. Wimmer, P. Fallon, A. O. Macchiavelli, A. Poves, V. M. Bader, D. Bazin, M. Bowry, C. M. Campbell, M. P. Carpenter, R. M. Clark, M. Cromaz, A. Gade, E. Ideguchi, H. Iwasaki, C. Langer, I. Y. Lee, C. Loelius, E. Lunderberg, C. Morse,

A. L. Richard, J. Rissanen, D. Smalley, S. R. Stroberg, D. Weisshaar, K. Whitmore, A. Wiens, S. J. Williams, K. Wimmer, and T. Yamamato, Phys. Rev. C **93** (2016).

[45] A. O. Macchiavelli, H. L. Crawford, C. M. Campbell, R. M. Clark, M. Cromaz, P. Fallon, M. D. Jones, I. Y. Lee, M. Salathe, B. A. Brown, and A. Poves, Phys. Rev. C **94** (2016).

[46] A. O. Macchiavelli and H. L. Crawford, Phys. Scr. **92** (2017).

[47] R. D. Evans, *The Atomic Nucleus*, 1st ed. (Tata McGraw-Hill Publishing Company Ltd., 1995).

[48] G. F. Knoll, *Radiation Detection and Measurement*, 4th ed. (Wiley, 2010).

[49] D. Weisshaar, D. Bazin, P. C. Bender, C. M. Campbell, F. Recchia, V. Bader, T. Baugher, J. Belarge, M. P. Carpenter, H. L. Crawford, M. Cromaz, B. Elman, P. Fallon, A. Forney, A. Gade, J. Harker, N. Kobayashi, C. Langer, T. Lauritsen, I. Y. Lee, A. Lemasson, B. Longfellow, E. Lunderberg, A. O. Macchiavelli, K. Miki, S. Momiyama, S. Noji, D. C. Radofrd, M. Scott, J. Sethi, S. R. Stroberg, Z. Sullivan, R. Titus, A. Wiens, S. Williams, K. Wimmer, and S. Zhu, Nucl. Instrum Methods Phys. Res., Sect. A **847**, 187 (2017).

[50] A. Lemasson, H. Iwasaki, C. Morse, D. Bazin, T. Baugher, J. S. Berryman, A. Dewald, C. Fransen, A. Gade, C. McDaniel, A. Nichols, A. Ratkiewicz, S. Stroberg, P. Voss, R. Wadsworth, D. Weisshaar, K. Wimmer, and R. Winkler, Phys. Rev. C **85** (2012).

[51] P. J. Nolan and J. F. Sharpey-Schafer, Rep. Prog Phys. **42**, 1 (1979).

[52] A. Dewald, O. Möller, and P. Petkov, Prog. Part. Nucl. Phys. **67**, 786 (2012).

[53] S. Shimoura, A. Saito, T. Minemura, Y. U. Matsuyama, H. Baba, H. Akiyoshi, N. Aoi, T. Gomi, Y. Higurashi, K. Ieki, N. Imai, N. Iwasa, H. Iwasaki, S. Kanno, S. Kubono, M. Kunibu, S. Michimasa, T. Motobayashi, T. Nakamura, H. Sakurai, M. Serata, E. Takeshita, S. Takeuchi, T. Teranishi, K. Ue, K. Yamada, Y. Yanagisawa, M. Ishihara, and N. Itagaki, Phys. Lett. B **560**, 31 (2003).

[54] R. Elder, H. Iwasaki, J. Ash, D. Bazin, P. C. Bender, T. Braunroth, B. A. Brown, C. M. Campbell, H. L. Crawford, B. Elman, A. Gade, M. Grinder, N. Kobayashi, B. Longfellow, A. O. Macchiavelli, T. Mijatović, J. Pereira, A. Revel, D. Rhodes, J. A. Tostevin, and D. Weisshaar, Phys. Rev. C **100** (2019).

[55] P. G. Hansen and J. A. Tostevin, Annu. Rev. Nucl. Part. Sci. **53**, 219 (2003).

[56] J. A. Tostevin and B. A. Brown, Phys. Rev. C **74** (2006).

[57] P. G. Hansen and B. M. Sherrill, Nucl. Phys. A **693**, 133 (2001).

[58] A. Mutschler, A. Lemasson, O. Sorlin, D. Bazin, C. Borcea, R. Borcea, Z. Dombrádi, J.-P. Ebran, A. Gade, H. Iwasaki, E. Khan, A. Lepailleur, F. Recchia, T. Roger, F. Rotaru, D. Sohler, M. Stanoiu, S. R. Stroberg, J. A. Tostevin, M. Vandebrouck, D. Weisshaar, and K. Wimmer, Nature **13**, 152 (2016).

[59] D. Bazin, B. A. Brown, C. M. Campbell, J. A. Church, D. C. Dinca, J. Enders, A. Gade, T. Glasmacher, P. G. Hansen, W. F. Mueller, H. Olliver, B. C. Perry, B. M. Sherrill, J. R. Terry, and J. A. Tostevin, Phys. Rev. Lett. **91** (2003).

[60] F. Rotaru, F. Negoita, S. Grévy, J. Mrazek, S. Lukyanov, F. Nowacki, A. Poves, O. Sorlin, C. Borcea, R. Borcea, A. Buta, L. Cáceres, S. Calinescu, R. Chevrier, Z. Dombrádi, J. M. Daugas, D. Lebhertz, Y. Penionzhevich, C. Petrone, D. Sohler, M. Stanoiu, and J. C. Thomas, Phys. Rev. Lett. **109** (2012).

[61] P. A. Zavodszky, B. Arend, D. Cole, J. DeKamp, G. Machinoane, F. Marti, P. Miller, J. Moskalik, J. Ottarson, J. Vincent, and A. Zeller, Nucl. Instrum and Methods B **241**, 959 (2005).

[62] D. J. Morrissey, Nucl. Phys. A **616**, 45c (1997).

[63] B.-M. Sherrill, Progress of Theoretical Physics Supplement **146**, 60 (2002).

[64] D. J. Morrissey, B. M. Sherrill, M. Steiner, A. Stolz, and I. Wiedenhoever, Nucl. Instrum. Methods Phys. Res., Sect. B **204**, 90 (2003).

[65] D. Bazin, J. A. Caggiano, B. M. Sherrill, J. Yurkon, and A. Zeller, Nucl. Instrum. Methods Phys. Res., Sect. B **204**, 629 (2003).

[66] S. Paschalis, I.Y.Lee, A. Macchiavelli, C. M. Campbell, M. Cromaz, S. Gros, J. Pavan, J. Qian, R. M. Clark, H. L. Crawford, D. Doering, P. Fallon, C. Lionberger, T. Loew, M. Petri, T. Stezelberger, S. Zimmermann, D. C. Radford, K. Lagergren, D. Weisshaar, R. Winkler, T. Glasmacher, J. T. Anderson, and C. W. Beausang, Nucl. Instrum. Methods **709**, 44 (2013).

[67] I. Brown, *The Physics and Technology of Ion Sources*, 2nd ed. (Wiley-VCH, 2004).

[68] E. O. Lawrence and M. S. Livingston, Phys. Rev. **40**, 19 (1932).

[69] J. P. Dufour, R. D. Moral, H. Emmermann, F. Hubert, D. Jean, C. Poinot, M. S. Pravikoff, and A. Fleury, Nucl. Instrum. and Methods Sect. A **248**, 267 (1986).

[70] **S800 Spectrograph wiki**, `https://wikihost.nscl.msu.edu/S800Doc/` (2020), accessed: 2020-05-09.

[71] J. Yurkon, D. Bazin, W. Benenson, D. J. Morrissey, B. M. Sherrill, D. Swan, and R. Swanson, Nucl. Instrum. Methods, Sect. B **422**, 291 (1999).

[72] K. Meierbachtol, D. Bazin, and D. J. Morrissey, Nucl. Instrum. Methods, Sect. A **652**, 668 (2011).

[73] K. Wimmer, D. Barofsky, D. Bazin, L. M. Fraile, J. Lloyd, J. R. Tompkins, and S. J. Williams, Nucl. Instrum. and Methods Sect. A **769**, 65 (2015).

[74] M. Berz, K. Joh, J. A. Nolen, B. M. Sherrill, and A. F. Zeller, Phys. Rev. C **47** (1993).

[75] M. Robinson, P. Halse, W. Trinder, R. Anne, C. Borcea, M. Lewitowicz, S. Lukyanov, M. Mirea, Y. Oganessian, N. A. Orr, Y. Peniozhkevich, M. G. Saint-Laurent, and O. Tarasov, Phys. Rev. C **53** (1996).

[76] M. Cromaz, V. J. Riot, P. Fallon, S. Gros, B. Holmes, I. Y. Lee, A. O. Macchiavelli, C. Vu, H. Yaver, and S. Zimmermann, Nucl. Instrum. Methods A **597**, 233 (2008).

[77] J. Anderson, R. Brito, D. Doering, T. Hayden, B. Holmes, J. Joseph, H. Yaver, and S. Zimmermann, IEEE Trans. Nucl. Sci. **NS-56**, 258 (2009).

[78] C. Loelius, H. Iwasaki, B. A. Brown, M. Honma, V. M. Bader, T. Baugher, D. Bazin, J. S. Berryman, T. Braunroth, C. M. Campbell, A. Dewald, A. Gade, N. Kobayashi, C. Langer, I. Y. Lee, A. Lemasson, E. Lunderberg, C. Morse, F. Recchia, D. Smalley, S. R. Stroberg, R. Wadsworth, C. Walz, D. Weisshaar, A. Westerberg, K. Whitmore, and K. Wimmer, Phys. Rev. C **94** (2016).

[79] **National Institute of Standards and Technology**, x-ray Mass Attenuation Coefficients, `https://physics.nist.gov/PhysRefData/XrayMassCoef/tab3.html` (2004), accessed: 2004-03-29.

[80] H. Iwasaki, A. Dewald, T. Braunroth, C. Fransen, D. Smalley, A. Lemasson, C. Morse, K. Whitmore, and C. Loelius, Nucl. Instrum. Methods Phys. Res., Sect. A **806**, 123 (2016).

[81] T. K. Alexander and K. W. Allen, Can. J. Phys. **43** (1965).

[82] A. B. T. K. Alexander, Nuclear Instruments and Methods **81**, 22 (1970).

[83] A. Dewald, S. Harissopulos, and P. von Brentano, Zeitschrift für Physik **334**, 163 (1989).

[84] P. Bednarczyk, J. Grębosz, M. Kmiecik, A. Maj, W. Męczyński, S. Myalski, J. Styczeń, C. Domingo-Pardo, P. Doornenbal, J. Gerl, M. Górska, H. J. Wollersheim, J. Jolie, P. Reiter, A. Bracco, and F. Camera, Acta Physica Polonica B **41**, 505 (2010).

[85] Physik Instrumente, N-381 NEXACT Linear Actuator, `https://www.physikinstrumente.com/en/products/linear-actuators/`, accessed: 2020-02-13.

[86] TESA, Wireless probe, `https://tesatechnology.com/en-us/products/measuring-probes-and-display-units/usb-or-wireless-measuring-probes/wireless-probe_p40763.htm`, accessed: 2020-02-13.

[87] C. Ouellet and B. Singh, Nucl. Data Sheets **112**, 2199 (Data extracted from the ENSDF online database June, 2019) (2011).

[88] H. Nishibata, T. Shimoda, A. Odahara, S. Morimoto, S. Kanaya, A. Yagi, H. Kanaoka, M. R. Pearson, C. D. P. Levy, and M. Kimura, Phys. Lett. B **767**, 81 (2017).

[89] R. Fox, **SpecTcl Home page**, `http://docs.nscl.msu.edu/daq/spectcl/` (2003), accessed: 2020-04-04.

[90] K. Wimmer and E. Lunderberg, Nuclear Structure and Reactions Software, `http://nucl.phys.s.u-tokyo.ac.jp/wimmer/software.php` (2016), accessed: 2020-04-04.

[91] S. Agostinelli, J. Allison, K. Amako, J. Apostolakis, H. Araujo, P. Arce, M. Asai, D. Axen, S. Banerjee, G. Barrand, F. Behner, L. Bellagamba, J. Boudreau, L. Broglia, A. Brunengo, H. Burkhardt, S. Chauvie, J. Chuma, R. .Chytracek, G. Cooperman, G. Cosmo, P. Degtyarenko, A. Dell'Acqua, G. Depaola, D. Dietrich, R. Enami, A. Feliciello, C. Ferguson, H. Fesefeldt, G. Folger, F. Foppiano, A. Forti, S. Garelli, S. Giani, R. Giannitrapani, D. Gibin, J. J. G. Cadenas, I. González, G. G. Abril, G. Greeniaus, W. Greiner, V. Grichine, A. Grossheim, S. Guatelli, P. Gumplinger, R. Hamatsu, K. Hashimoto, H. Hasui, A. Heikkinen, A. Howard, V. Ivanchenko, A. Johnson, F. W. Jones, J. Kallenbach, N. Kanaya, M. Kawabata, Y. Kawabata, M. Kawaguti, S. Kelner, P. Kent, A. Kimura, T. Kodama, R. Kokoulin, M. Kossov, H. Kurashige, E. Lamanna, T. Lampén, V. Lara, V. Lefebure, F. Lei, M. Liendl, W. Lockman, F. Longo, S. Magni, M. Maire, E. Medernach, K. Minamimoto, P. M. de Freitas, Y. Morita, K. Murakami, M. Nagamatu, R. Nartallo, P. Nieminen, T. Nishimura, K. Ohtsubo, M. Okamura, S. O'Neale, Y. Oohata, K. Paech, J. Perl, A. Pfeiffer, M. G. Pia, F. Ranjard, A. Rybin, S. Sadilov, E. D. Salvo, G. Santin, T. Sasaki, N. Savvas, Y. Sawada, S. Scherer, S. Sei, V. Sirotenko, D. Smith, N. Starkov, H. Stoecker, J. Sulkimo, M. Takahata, S. Tanaka, E. Tcherniaev, E. S. Tehrani, M. Tropeano, P. Truscott, H. Uno, L. Urban, P. Urban, M. Verderi, A. Walkden, W. Wander, H. Weber, J. P. Wellisch, T. Wenaus, D. C. Williams, D. Wright, T. Yamada, H. Yoshida, and D. Zschiesche, Nucl. Instrum. Methods Phys. Res., Sect. A **506**, 250 (2003).

[92] NSCL lifetime group webpage, `https://wikihost.nscl.msu.edu/lifetime/`, accessed: 2020-04-04.

[93] S. Baker and R. D. Cousins, Nucl. Instrum. Methods **221**, 437 (1984).

[94] K. Wimmer, Normal and intruder configurations in the island of inversion (2016) 2016.

[95] M. S. Basunia, Nucl. Data Sheets **111**, 2331 (Data extracted from the ENSDF online database July, 2019 (2010).

[96] A. J. Rutten, A. Holthuizen, J. A. G. D. Raedt, W. A. Sterrenburg, and G. V. Middelkoop, Nucl. Phys. A **344**, 294 (1980).

[97] Z. Berant, C. Broude, G. Engler, M. Hass, R. Levy, and B. Richter, Nucl. Phys. A **243**, 519 (1975).

[98] J. A. J. Hermans, G. A. P. Engelbertink, L. P. Ekström, H. H. Eggenhuisen, and M. A. V. Driel, Nucl. Phys. A **284**, 307 (1977).

[99] T. Lauritsen, A. Korichi, S. Zhu, A. N. Wilson, D. Weisshaar, J. Dudouet, A. D. Ayangeakaa, M. P. Carpenter, C. M. Campbell, E. Clément, H. L. Crawford, M. Cromaz, P. Fallon, J. P. Greene, R. V. F. Janssens, T. L. Khoo, N. Lalović, I. Y. Lee, A. O. Macchiavelli, R. M. Perez-Vidal, S. Pietri, D. C. Radford, D. Ralet, L. A. Riley, D. Seweryniak, and O. Stezowski, Nucl. Instrum. Methods Phys. Res., Sect. A **836**, 46 (2016).

[100] B. A. Brown and W. A. Richter, Phys. Rev. C **74** (2006).

[101] Goodfellow, `http://www.goodfellow.com/` (2020), accessed: 2020-03-09.

[102] S. K. Ashour and M. A. Abdel-hameed, Journal of Advanced Research **1** (2010).

[103] M. S. Basunia, Nucl. Data Sheets **114**, 1189 (Data extracted from the ENSDF online database June, 2019) (2013).

[104] N. Nica and B. Singh, Nucl. Data Sheets **113**, 1563 (Data extracted from the ENSDF online database June, 2019) (2012).

[105] P. Doornenbal, H. Scheit, S. Takeuchi, N. Aoi, K. Li, M. Matsushita, D. Steppenbeck, H. Wang, H. Baba, E. Ideguchi, N. Kobayashi, Y. Konda, J. Lee, S. Michimasa, T. Motobayashi, A. Poves, H. Sakurai, M. Takechi, Y. Togano, and K. Yoneda, Phys. Rev. C **93** (2016).

[106] B. A. Brown and B. H. Wildenthal, Ann. Rev. Nucl. Part. Sci. **38**, 29 (1988).

[107] T. T. S. Kuo and G. E. Brown, Nucl. Phys. A **114**, 241 (1968).

[108] J. Dechargé and D. Gogny, Phys. Rev. C **21**, 1568 (1980).

[109] T. T. S. Kuo, S. Y. Lee, and K. F. Ratcliff, Nucl. Phys. A **176**, 65 (1971).

[110] E. M. Krenciglowa and T. T. S. Kuo, Nucl. Phys. A **235**, 171 (1974).

[111] E. M. Krenciglowa, T. T. S. Kuo, E. Osnes, and P. J. Ellis, Nucl. Phys. A **289**, 381 (1977).

[112] H. L. Crawford, P. Fallon, A. O. Macchiavelli, P. Doornenbal, N. Aoi, F. Browne, C. M. Campbell, S. Chen, R. M. Clark, M. L. Cortés, M. Cromaz, E. Ideguchi, M. D. Jones, R. Kanungo, M. MacCormick, S. Momiyama, I. Murray, M. Niikura, S. Paschalis, M. Petri, H. Sakurai, M. Salathe, P. Schrock, D. Steppenbeck, S. Takeuchi, Y. K. Tanaka, R. Taniuchi, H. Wang, and K. Wimmer, Phys. Rev. Lett. **122**, 052501 (2019).

[113] T. Kibédi, T. W. Burrows, M. B. Trzhaskovskaya, P. M. Davidson, and C. W. N. Jr., Nucl. Instrum. Methods Phys. Res., Sect. A **589**, 202 (2008).

[114] R. W. Ibbotson, T. Glasmacher, B. A. Brown, L. Chen, M. J. Chromik, P. D. Cottle, M. Fauerbach, K. W. Kemper, D. J. Morrissey, H. Scheit, and M. Thoennessen, Phys. Rev. Lett. **80** (1998).

[115] O. Neidermaier, H. Scheit, V. Bildstein, H. Boie, J. Figging, R. von Hahn, F. Köck, M. Lauer, U. K. Pal, H. Podlech, R. Repnow, D. Schwalm., C. Alvarez, F. Ames, G. Bollen, S. Emhofer, D. Habs, O. Kester, R. Lutter, K. Rudolph, M. Pasini, P. G. Thirolf, B. H. Wolf, J. Eberth, G. Gersch, H. Hess, P. Reiter, O. Thelen, N. Warr, D. Weisshaar, F. Aksouh, P. V. den Bergh, P. V. Duppen, M. Huyse, O. Ivanov, P. Mayet, J. V. de Walle, J. Äystö, P. A. Butler, J. Cederkäll, P. Delahaye, H. O. U. Fynbo, L. M. Fraile, O. Forstner, S. Franchoo, U. Köster, T. Nilsson, M. Oinonen, T. Sieber, F. Wenander, M. Pantea, A. Richter, G. Schreider, H. Simon, T. Behrens, R. Gernhäuser, T. Kröll, Krücken, M. Münch, T. Davison, J. Gerl, G. Huber, A. Hurst, J. Iwanicki, B. Jonson, P. Lieb, L. Liljeby, A. S. nad A. Scherillo, P. Schmidt, and G. Walter, Phys. Rev. Lett. **94** (2005).

[116] P. Fallon, E. Rodriguez-Vieitez, A. O. Macchiavelli, A. Gade, J. A. Tostevin, P. Adrich, D. Bazin, M. Bowen, C. M. Campbell, R. M. Clark, J. M. Cook, M. Cromaz, D. C. Dinca, T. Glasmacher, I. Y. Lee, S. McDaniel, W. F. Mueller, S. G. Prussin, A. Ratkiewicz, K. Siwek, J. R. Terry, D. Weisshaar, M. Wiedeking, K. Yoneda, B. A. Brown, T. Otsuka, and Y. Utsuno, Phys. Rev. C **81** (2010).

[117] I. Murray, M. MacCormick, D. Bazin, P. Doornenbal, N. Aoi, H. Baba, H. Crawford, P. Fallon, K. Li, J. Lee, M. Matsushita, T. Motobayashi, T. Otsuka, H. Sakurai, H. Scheit, D. Steppenbeck, S. Takeuchi, J. A. Tostevin, N. Tsunoda, Y. Utsuno, H. Wang, and K. Yoneda, Phys. Rev. C **99** (2019).

[118] B. P. Crider, C. J. Prokop, S. N. Liddick, M. Al-Shudifat, A. D. Ayangeakaa, M. P. Carpenter, J. J. Carroll, J. Chen, C. J. Chiara, H. M. David, A. C. Dombos, S. Go, R. Grzywacz, J. Harker, R. V. F. Janssens, N. Larson, T. Lauritsen, R. Lew, S. J. Quinn, F. Recchia, A. Spyrou, W. B. Walters, and S. Zhu, Phys. Lett. B **763**, 108 (2016).